

REPORT DOCUMENT

AD-A238 098

Form Approved
OMB No. 0704-0188

Public reporting burden for this collection of information is estimated to average 1 hour per response, including the time for reviewing instructions, searching existing data sources, gathering and maintaining the data needed, and completing and reviewing this collection of information. Send comments regarding this burden estimate or any other aspect of this collection of information, including suggestions for reducing this burden, to Washington Headquarters Services, Directorate for Information Operations and Reports, 1215 Jefferson Davis Highway, Suite 1204, Arlington, VA 22202-4302.



reviewing instructions, searching existing data sources, gathering this burden estimate or any other aspect of this or information Operations and Reports, 1215 Jefferson Davis Highway, Suite 1204, Arlington, VA 22202-4302.

1. AGENCY USE ONLY (Leave blank)		2. REPORT DATE April 1991		3. REPORT TYPE AND DATES COVERED Final 15 Dec 85 - 31 Jan 90	
4. TITLE AND SUBTITLE Three-Dimensional Mapping of Atmospheric Boundary Layer Structure and Winds with a High Performance Lidar				5. FUNDING NUMBERS DAAL03-86-K-0024	
6. AUTHOR(S) Edwin W. Eloranta					
7. PERFORMING ORGANIZATION NAME(S) AND ADDRESS(ES) University of Wisconsin-Madison Madison, Wisconsin 53706				8. PERFORMING ORGANIZATION REPORT NUMBER	
9. SPONSORING / MONITORING AGENCY NAME(S) AND ADDRESS(ES) U. S. Army Research Office P. O. Box 12211 Research Triangle Park, NC 27709-2211				10. SPONSORING / MONITORING AGENCY REPORT NUMBER ARO 23217.4-GS	
11. SUPPLEMENTARY NOTES The view, opinions and/or findings contained in this report are those of the author(s) and should not be construed as an official Department of the Army position, policy, or decision, unless so designated by other documentation.					
12a. DISTRIBUTION / AVAILABILITY STATEMENT Approved for public release; distribution unlimited.				12b. DISTRIBUTION CODE	
13. ABSTRACT (Maximum 200 words) Initial work under this grant concentrated on construction of the Volume Imaging Lidar (VIL). Work on this system had begun under the support of ARO Grant DAAG29-84-G-0028; the system was completed with support from this grant and Office of Naval Research Grant N0014-87-0436. While the major mechanical structures were completed on the previous contract most of the system integration and testing remained when this grant began. The result of this work is an instrument with unmatched capabilities; no existing lidar system approaches its ability to map the three-dimensional structure of the atmosphere. A brief description of the VIL is supplied as appendix A.					
14. SUBJECT TERMS High Performance Lidar, Lidar Systems, Atmospheric Boundary Layer, Volume Imaging Lidar				15. NUMBER OF PAGES 90	
				16. PRICE CODE	
17. SECURITY CLASSIFICATION OF REPORT UNCLASSIFIED	18. SECURITY CLASSIFICATION OF THIS PAGE UNCLASSIFIED	19. SECURITY CLASSIFICATION OF ABSTRACT UNCLASSIFIED	20. LIMITATION OF ABSTRACT UL		

Three-Dimensional Mapping of Atmospheric Boundary Layer Structure and
Winds with a High Performance Lidar

FINAL REPORT

Edwin W. Eloranta

1991

U.S. ARMY RESEARCH OFFICE

DAAL03-86-K-0024

UNIVERSITY OF WISCONSIN

91-05348



APPROVED FOR PUBLIC RELEASE;

DISTRIBUTION UNLIMITED

THE VIEW, OPINIONS, AND/OR FINDINGS CONTAINED IN THIS REPORT ARE THOSE OF THE
AUTHOR(S) AND SHOULD NOT BE CONSTRUED AS AN OFFICIAL DEPARTMENT OF THE ARMY
POSITION, POLICY, OR DECISION, UNLESS SO DESIGNATED BY OTHER DOCUMENTATION.

91 7 17 097

Accession For	
DTIC TAB	<input checked="" type="checkbox"/>
Unannounced	<input type="checkbox"/>
Justification	<input type="checkbox"/>
Distribution/	
Availability Codes	
Dist	Avail and/or Special
A-1	

Final report on US Army Research Office Grant DAAL03-86-K-0024 (Univ. of Wisconsin 144-X500) 12/15/85 to 1/31/90.

Completion of the VIL hardware

Initial work under this grant concentrated on construction of the Volume Imaging Lidar (VIL). Work on this system had begun under the support of ARO Grant DAAG29-84-G-0028; the system was completed with support from this grant and Office of Naval Research Grant N0014-87-0436. While the major mechanical structures were completed on the previous contract most of the system integration and testing remained when this grant began. The result of this work is an instrument with unmatched capabilities; no existing lidar system approaches its ability to map the three-dimensional structure of the atmosphere. A brief description of the VIL is supplied as appendix A.

Generation of data acquisition software

The VIL has demanding data acquisition and control requirements. We are not aware of any lidar system capable of data acquisition at a higher sustained rate. The VIL digitizers acquire more than 0.7 gigabyte of data per hour of operation. Realtime processing is required to compress the volume of recorded data and in order to provide data displays for operator control of data acquisition. To perform these functions the VIL data system includes the following computers:

DEC VAX 751	System Control and data archiving
CSPI MiniMap Array Processor	Realtime data processing
DEC LSI 11/73	Front end data formatting and transfer
Intel 8085	Scan control
Stardent GS-1000	Data display

Each of these computers has required development of special purpose software: much of this programming has been supported by this grant.

Development of lidar image display software

A single VIL volume scan consists of 5 to 10 million data points. Software has been written to display these data in a variety of image formats. Programs provide Range-Height-Indicator (RHI), Plan-Position-Indicator (PPI), and Constant-Altitude-Plan-Position-Indicator (CAPPI) for realtime display of images during data acquisition. Other programs have been developed to superimpose aircraft measured data on the lidar images and to correct images for distortion produced by wind motions during the time required to complete a laser scan. Programs which contour the VIL backscatter signal and display the contour surface as three dimensional objects have also been prepared. Additional routines use ray tracing solutions to display clouds and boundary layer aerosol backscatter in a visually realistic reproduction. These programs provide two dimensional images of the three dimensional objects; they also allow viewing images in 3-D stereo with red-green glasses. A few examples of VIL images are provided in appendix A. Animation routines have been developed which allow time-lapse 'movie' display of all images types. This software provides the VIL with most powerful lidar image display capability in existence.

Improvements to the Volume Imaging lidar system:

In our progress report of 11/30/88 we reported a series of lidar system problems uncovered during the 1987 FIFE experiment. Mechanical modifications to the beam steering unit including the a strengthening of major components and installation of new angle readout transducers have eliminated serious problems with the pointing angle readouts and greatly improved on alignment errors previously encountered. Tests of the beam steering unit now shows a repeatability of the pointing angle to a fixed ground based target at the 0.01 degree level. All sticking of the scanning unit and erroneous angle reports appear to have been eliminated. We still encounter slight shifts in transmitter receiver alignment with scan direction. Modifications to the photo detector preamplifier have nearly eliminated gain and offset fluctuations which depended on the previous lidar return, but work to solve the remaining low level effects continue. The overall effect of system improvements has been to nearly double the useful range of the lidar. Under favorable conditions, usable boundary layer data has been acquired at ranges up to 30km; even with relatively poor conditions good data is now acquired at ranges up to 15km. Cirrus cloud observations have been demonstrated at ranges exceeding 100km.

Wind measurement algorithms

Algorithms were developed to measure the area-averaged vertical profile of the horizontal wind by observing the drift of naturally occurring inhomogeneities in the aerosol backscatter. Area-averaging allows wind profiles with a few cm/sec accuracy to be derived in the presence of convective boundary layer turbulence. These results profiles are achieved with averaging times as short as 3 minutes. These were reported at the 15th International Lidar Conference, Tomsk, USSR, August, 1989 and also in a paper submitted to the Journal of Geophysical Research (copy enclosed as appendix E).

Analysis of BLX-83 data

Data analysis begun in a masters thesis supported under a previous ARO grant (DAA-G29-80-K-0079) was extended and prepared for publication under this grant. Richard Ferrare's masters thesis "Lidar observations of organized convection within the atmospheric mixed layer" formed the basis for this paper. The extended results have been accepted for publication in the Journal of Applied Meteorology (copy enclosed as appendix B). Additional analysis of BLX-83 resulted in a paper "a prognostic relationship for entrainment zone thickness" by Nelson, Stull and Eloranta (copy enclosed as appendix D).

Operation of the system in field experiments

The VIL has been operated in a series of field experiments which were partially supported by this grant.

FIFE-87

The first operation of the VIL took place as part of the NASA First ISLSCP Field Experiment(FIFE 87). The VIL was operated just South of Manhattan Kansas from June 30 to July 8, 1987. Direct costs of the field campaign were funded by

NASA. This experiment provided a test of the VIL and provided a valuable data set. The first three-dimensional lidar pictures of clear air convection were produced from this data (first reported at the AMS conference on Turbulence and Diffusion, San Diego, 1989). The data was also used to develop algorithms for measuring area-averaged vertical profiles of the horizontal wind. These were described in a paper presented at the 15th International Laser Radar Conference, Tomsk, USSR, August 1990 and a paper describing the technique is attached as appendix E.

Four-dimensional correlation functions describing the spatial structure and temporal evolution of inhomogeneities in the aerosol backscatter were computed from this data (see enclosed MS thesis by Chen-Hui Sun).

This initial experiment also served to identify weaknesses in the VIL system. These included mechanical problems which degraded the pointing accuracy of the scanning mirror assembly, a baseline offset problem in the photodetector preamplifier, and the need for a more capable realtime image display.

Gibbs Lake-87

The Gibbs Lake experiment (9/23/87 to 11/6/87) was a pilot experiment designed to detect an isolated convective plume produced at night over the warm water of a small lake. It was anticipated that an isolated convective plume would be detectable on cool calm nights with high relative humidity. However, weather conditions favorable for formation and detection of the plume did not occur during this observation period. Despite our failure to achieve our first objective this experiment produced significant results. Daytime measurements provided observations of a subvisual smoke plume as it was transported by and incorporated into a weakly convective mixed layer. These observations were reported at the AMS Seventh Symposium on Air Pollution (New Orleans, Jan., 1991). The first three-dimensional lidar images of cirrus clouds were generated from an exploratory set of cirrus cloud observations made during this experiment. These results were reported at the AGAR Conference on Atmospheric Propagation in the UV, Visible, IR and MM-Wave Region and Related Systems Aspects, Copenhagen, Denmark, October 1989.

FIFE 89

Between July 26 and August 8, 1989 the VIL was deployed a second time at the site of FIFE-87. This experiment followed the design of the previous FIFE observations as described by Sellers and Forrest (Bulletin American Meteorological Society, 1-Jan-1989). The VIL recorded more than 11 million lidar profiles during 16 consecutive days of operation. Typical daily operations included 4 to 6 hours of nearly continuous operation. This experiment produced an extensive data set depicting the convective boundary layer over an extended site instrumented to measure meteorological surface fluxes as well as surface biology. A series of coordinated observations with a turbulent flux measuring aircraft and the lidar were also obtained. These measurements have been used

to show that the aircraft observations can be superimposed on lidar images of the three dimensional structure of the convective elements. It is possible not only to identify the location of the aircraft data with respect to the convective structure, but to also place the observation with respect to the temporal evolution of the structure. An initial discussion of these observations is reported in a paper submitted to The Journal of Geophysical Research (copy enclosed as appendix C). The FIFE 89 data set contains much data which has not been analyzed and this work will be the subject of future research proposals.

CREPE-89

Between November 7 and December 6, 1989 the Volume Imaging Lidar was operated near Madison, Wisconsin as part of the Cirrus Remote Sensing Pilot Experiment (CREPE). This was a coordinated experiment to observe the spatial structure and optical properties of cirrus clouds. The following instruments were deployed:

Instrument	Instrument provider
Volume Imaging Lidar	U Dept of Meteorology
High Spectral Resolution Lidar	U Dept of Meteorology
HIS, Infrared Fairer Transform Spectrometer	U Space Science center
The Scripts All Sky Camera	Scripts Visibility Lab.
The NCAR CLASS radiosonde	National Center for Atmospheric Research
The VAS instrument on GOES	U Space Science Center

During this experiment the VIL demonstrated the capability of mapping cirrus cloud structure at ranges up to 60 km. Scanning from a small elevation angle on one side the lidar overhead to a small elevation angle on the other side in approximately 25 seconds the VIL produced an image depicting structure in a 120 km slice of the atmosphere. Sequences of these images have been used to produce high spatial resolution 3-dimensional images of cirrus cloud structure. These results were reported at the 15th International Laser Radar Conference in August, 1990. A scientific paper based on this data is also presently in preparation. The direct costs of this experiment were funded under Office of Naval Research, Department of Energy and National Aeronautics and Space Administration grants, however the experiment would not have been possible without the equipment support offered under this grant.

Publications

Scientific papers describing results of work supported under this grant are enclosed. Titles, Authors and abstracts of these papers are reproduced below and copies of the papers are included as appendices to this report.

The following paper appeared in the Journal of Applied Meteorology, Vol. 28 No 9, Sept. 1989.

"A prognostic relationship for entrainment zone thickness"

E. Nelson, R. Stull, and E. W. Eloranta

Abstract

The thickness of the entrainment zone at the top of the atmospheric mixed layer is analyzed using measurements made with a ground-based lidar during the BLX-83 and CIRCE field programs. When the entrainment-zone depth normalized by mixed-layer depth is plotted as a function of the entrainment rate normalized by the convective velocity scale, with time as a parameter, a hysteresis curve results. Although portions of the curve can be approximated by diagnostic relationships, the complete hysteresis behavior is better described with a prognostic relationship. A simple thermodynamic model that maps the surface-layer frequency distribution of temperature into a corresponding entrainment zone distribution is shown to approximate the hysteresis evolution to first order.

The following paper has been accepted for publication by the Journal of Applied Meteorology.

"Lidar observations of linear convection during BLX-83"

R.A.Ferrare, J.L.Schols and E.W.Eloranta

Abstract

Lidar observations of clear air convection during the 1983 Boundary Layer Experiment (BLX83) reveal the presence of linearly organized regions of updrafts marked by enhanced aerosol backscattering. These linear aerosol structures were observed over a two hour period during a cloud-free morning. During this period, the depth of the Convective Boundary Layer (CBL) increased from 100m to 1300m. Wind speeds averaged over the depth of the CBL varied between 0 and 2 m/s, while the wind direction varied from 310 degrees to 110 degrees. The CBL instability parameter, $-Z_i/L$, increased from approximately 25 (weakly unstable) to 250 (strongly unstable). The spacings of the linearly organized plumes, which were visible across the area of the lidar inclined Plan Position Indicator (PPI) scans, scaled with the CBL height. These findings suggest that secondary circulations in the form of horizontal roll vortices were present under conditions not normal associated with roll vortices. The orientation of the lines of aerosol structures remained parallel (within 15 degrees) to the direction of the vertical shear of the horizontal wind across the depth of the CBL.

The following paper has been submitted to the Journal of Geophysical Research special issue on the results of the NASA FIFE experiment.

"The calculation of area-averaged vertical profiles of the horizontal wind velocity using the University of Wisconsin Volume Imaging lidar"

J.L.Schols and E.W.Eloranta

Abstract

Area-averaged horizontal wind measurements are derived from the motion of spatial inhomogeneities in aerosol backscattering observed with a volume imaging lidar. Spatial averaging provides high precision, reducing sample variation of wind measurements well below the level of turbulent fluctuations even under conditions of very light mean winds and strong convection, or under the difficult conditions represented by roll convection.

Wind velocities are measured, using the two-dimensional spatial cross correlation computed between successive horizontal plane maps of aerosol backscattering, assembled from three-dimensional lidar scans. Prior to the calculation the correlation function, three crucial steps are used: The scans are corrected for image distortion by the wind during a finite scan time, a temporal high pass median filter is applied to eliminate structure that does not move with the wind, and a histogram equalization is employed to reduce biases to the brightest features.

The following paper has been submitted to the Journal of Geophysical Research special issue on the results of the NASA FIFE experiment.

"Volume Imaging Lidar observations of the convective structure surrounding the flight path of a flux measuring aircraft"

E. W. Eloranta and D. K. Forrest.

Abstract

The University of Wisconsin Volume Imaging Lidar has been used to image the three-dimensional structure of clear air convective plumes in the volume surrounding the flight path of the instrumented Twin Otter aircraft operated by the National Aeronautical Establishment (NEA) of Canada. These observations allow location of insitu measurements with respect to the lidar observed structure of individual convective cells. Plots of $q'w'$ superimposed on lidar images clearly demonstrate the well known sampling difficulties encountered when attempting to measure fluxes near the top of the convective boundary layer. A comparison of flight leg-averaged winds measured by lidar agree to within 0.2 m/s in speed and 2.3 degrees in direction when loran navigation is used to determine average aircraft velocity.

The following University of Wisconsin Masters thesis was supported by this grant.

"3-D Spatial and Temporal Correlation Functions of Aerosol Structures in the Convective PBL"

Chen-Hui Sun

A copy of this document is enclosed. A particularly interesting feature of this work is the observations of superimposed correlation patterns with different lifetimes. A radially symmetric pattern associated with individual convective plumes is imposed on an underlying elliptical pattern generated by longitudinal rolls. This work has important implications in the modeling of turbulent diffusion. It also shows why aerosol pattern correlation techniques for wind measurement are sensitive to the time separation between measurement; if the time separation is too large the correlation peak becomes small and difficult to detect. In addition the wind velocities measured may become measurements of the drift of the longitudinal roll patterns which are less likely to reflect true wind velocities than the shorter lived thermals.

Conference presentations

American Meteorological Society Conference on Application of Air Pollution Meteorology, New Orleans, LA, January, 1990

"Three Dimensional Mapping of Aerosol Pollution Plumes in Convective Boundary Layers", E. W. Eloranta

15th International Laser Radar Conference, Tomsk, USSR, July 23-27, 1990.

"Lidar and Radiometric Observation of Local and Mesoscale Cirrus Cloud Properties with High Spectral and Spatial Resolution",
C. J. Grund, E. W. Eloranta, D. P. Wylie and H. E. Revercomb

"The Display of Volume Imaging Lidar Data", E. W. Eloranta,
D. K. Forrest and S. Kohn

IEEE Lasers and Electro-optics Society 1990 Annual Meeting, Boston, MA, November, 4-9, 1990.

"Three Dimensional Lidar Measurements of Boundary Layer Dynamics",
E. W. Eloranta

Seventh American Meteorological Conference on Atmospheric Radiation, San Francisco, July 23-27, 1990.

"Cirrus Cloud Characteristics Derived from Volume Imaging Lidar. High Spectral Resolution Lidar, His Radiometer and Satellite",
C. J. Grund, S. A. Ackerman, E. W. Eloranta, R. O. Knutesen,
H. E. Revercomb, W. L. Smith and D. P. Wylie

American Meteorological Symposium on FIFE, Anaheim, CA, February 7-9, 1990.

"Lidar Measurements of Winds and Boundary Layer Structure During FIFE",
E. W. Eloranta and J. L. Schols

15th International Laser Radar Conference, TOMSK, USSR, July 23-27, 1990
"Measurements of Spatially Averaged Wind Profiles with a Volume Imaging Lidar", E. W. Eloranta and J. Schols

"NATO AGARD Symposium on Atmospheric Propagation in the UV, Visible, IR and MM-wave Region and Related Systems Aspects", Copenhagen, Denmark, October 9-13, 1989.

"Cirrus Cloud Optical Properties Measured with the University of Wisconsin High Spectral Resolution and Volume Imaging Lidars"
E. W. Eloranta and C. J. Grund.

The 1989 International Symposium on JAPACS, Tuskuba, Japan, October 19-20, 1989.

"Boundary Layer Dynamics"

"American Meteorological Society Annual Meeting Special Session" Laser Atmospheric Studies of Clouds, Chemistry, Climate and Pollution", Anaheim, CA., January 1989.

"Observations of Atmospheric Structures in Four Dimensions with a High Performance Lidar"

ACU Spring Meeting, Baltimore, MD, May 8-12, 1989

"Four-Dimensional Observations of the Convective Boundary Layer Structures with the University of Wisconsin Lidar", E. W. Eloranta

"A Lidar System Designed for Time Resolved Three-Dimensional Mapping of Atmospheric Boundary Layer Structures", E. W. Eloranta

AMS, NCAR, NOAA Symposium on Lower Tropospheric Profiling: Needs and Technologies, Boulder, CO, May 1988.

"Lidar Observations of Atmospheric Structure", E. W. Eloranta

14th International Laser Radar Conference, San Candido, Italy, June 1988.

"Spatial Variations in Mixed Layer Growth Observed with Lidar",
G. D. Vassiliou and E. W. Eloranta

"A Lidar Designed for Three-Dimensional Time Resolved Mapping of Atmospheric Structure", E. W. Eloranta

Thirteenth International Laser Radar Conference, August 1986, Toronto, Canada

"Generation of Attenuation Corrected Images from Lidar Data",
E. W. Eloranta and D. K. Forest

"American Meteorological Society Annual Meeting Special Session" Laser Atmospheric Studies of Clouds, Chemistry, Climate and Pollution", Anaheim, CA, January 1989.

"Observations of Atmospheric Structures in Four Dimensions with a High Performance Lidar"

NSF Workshop on Airborne Instrumentation, Boulder, CO, October, 1988.

"Airborne Remote Sensors: A Means to Achieve Statistically, Reliable Sampling of Atmospheric Variables"

Optical Society of America, Topical Meeting on Laser and Optical Remote Sensing: Instrumentation and Technique. North Falmouth, MA, September 1987.

"Lidar Measurements of Boundary Layer Parameters"

American Meteorological Society Symposium on Meteorological Observations and Instruments, New Orleans, LA, January 1987.

"Lidar Observations of the Atmospheric Boundary Layer"

Workshop on Ground Based Remote Sensing Techniques for the Troposphere, Hamburg, Germany, August, 1986.

"Applications of Incoherent Lidar to Atmospheric Boundary Layer Research"

Appendix A

The University of Wisconsin Volume Imaging Lidar (VIL)

The Volume Imaging Lidar(VIL) is an elastic backscatter lidar designed to image the 4-dimensional structure of the atmosphere. This system couples an energetic high pulse repetition rate laser with a sensitive receiver, and a fast computer controlled angular scanning system. High bandwidth data acquisition is sustained during extended experiments by using a 2.6 gigabyte write once optical disk for data storage. A Stellar GS-1000 graphics computer provides 1280x1024 pixel resolution lidar images with 24 bit true color rendition. Data analysis and real time control of data acquisition are facilitated by the display of 2-dimensional and 3-dimensional displays of lidar data. System specifications and a block diagram are provided in figure 1.

High sensitivity allows observation of inhomogeneities in natural aerosol content which reveal clear air convective structure. For boundary layer observations the lidar is typically programed to repeatedly scan an atmospheric volume consisting of the elevation angles between the horizon and 20° inside an azimuthal sector of 30° to 60° . Scans are repeated at intervals between 2.5 and 5 minutes. Each volume scan consists of 4500-9000 lidar profiles; producing 5-10 million independent measurements of lidar backscattering in the scanned volume. Clear air aerosol structure is typically recorded with 7.5 to 15 meter resolution at ranges between the lidar and 15 km. Figure 2 presents an example of clear air boundary layer structure obtained from a single VIL volume scan. This display combines a Range-Height-Indicator (RHI) scan obtained at one azimuth with Constant-Altitude-Plan-Position-Indicator (CAPPI) scans at several altitudes. Images of this type are continuously displayed during lidar operation to allow real-time control of data taking operations. Three-dimensional images of boundary layer structure are easily derived from VIL data. In one form of display a contour level enclosing all regions greater than a selected threshold is displayed as a solid body in 3-dimensional perspective. Figure 3 provides an example of this type of image. A family of such images can be prepared using different thresholds or observer view points. Sequences of images can be animated to allow vivid portrayal of motion and temporal evolution. Red-green image pairs can be created to allow true stereo vision of 3-dimensional images with the aid of special glasses. Three-dimensional images are also constructed from ray tracing codes to provide images which mimic the actual visual appearance of boundary layer aerosol and cloud fields.

Cirrus clouds are easily detected at ranges of 100 km. Detailed cirrus images showing a 120 km horizontal extent with 60 meter resolution are routinely obtained. Figure 4 presents a pair of cirrus images obtained with the VIL; two perpendicular scan planes are shown: a north-zenith-south plane and an east-zenith-west plane. Images pairs are typically recorded at approximately one minute intervals. Continuous observations are possible over many-hour periods. Individual scan planes typically consist of 900 lidar profiles containing 1024 data points each.

Cirrus structure typically moves at 20-40 m/sec; clouds move before we can completely scan the cloud volume. In order to generate 3-dimensional images of fast moving cirrus, the lidar repeatedly scans a plane perpendicular to the mean wind in the cloud. Three-dimensional scenes are displayed by computing the third spatial dimension from the time between images multiplied by the wind speed. Two types of images have been produced in this fashion. In the first, the cloud is modeled as a partially transparent object with the image intensity proportional to the integrated backscatter observed along each line of sight through the cloud. In the second image type (see figure 5), the cloud is modeled as a solid object as described for boundary layer images.

U.W. ND-YAG LIDAR

Transmitter:

Ave. Power

25 W

Repetition Rate

30 Hz

Wavelength

1064 nm

Receiver:

Diameter

0.5 m

Angular Scanning Rate

25 deg/s

APD Quantum Efficiency

35 %

Range Resolution

7.5 m

Optical Bandwidth

1 nm

Average Data Rate ~ 1/2 Gbyte/hr

Data Processing/Storage:

Vax 11/750 Computer

LSI 11/73 Computer

CSPI Array Processor

2.6 Gbyte Write Once Optical Disk

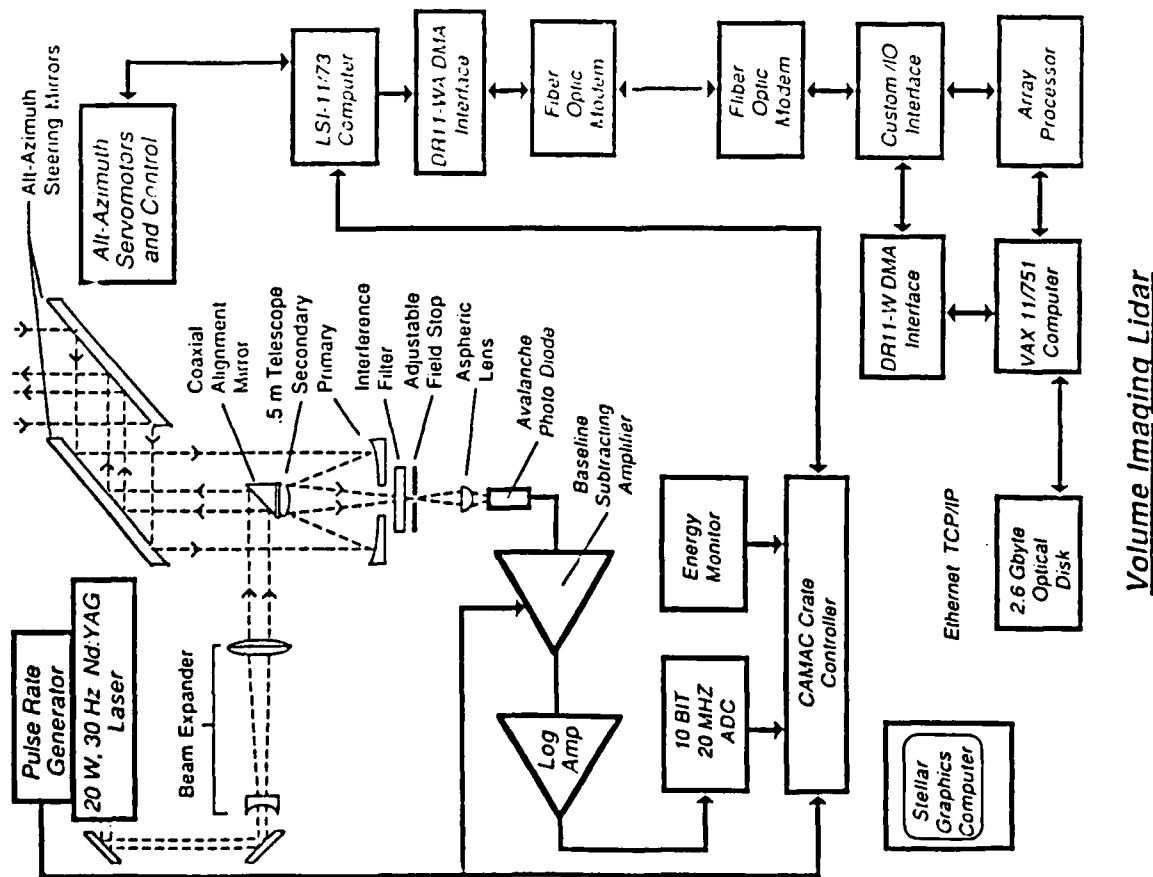
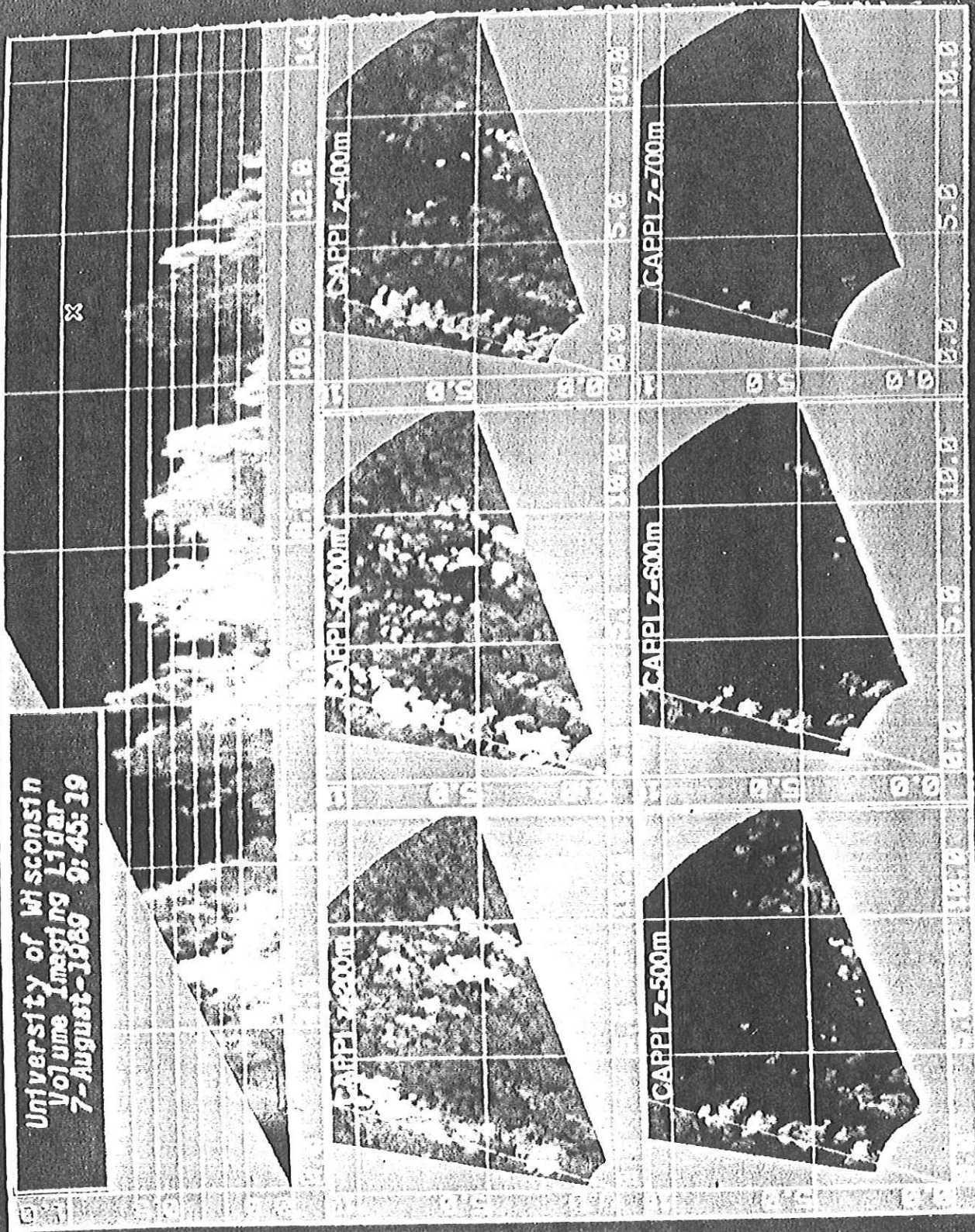
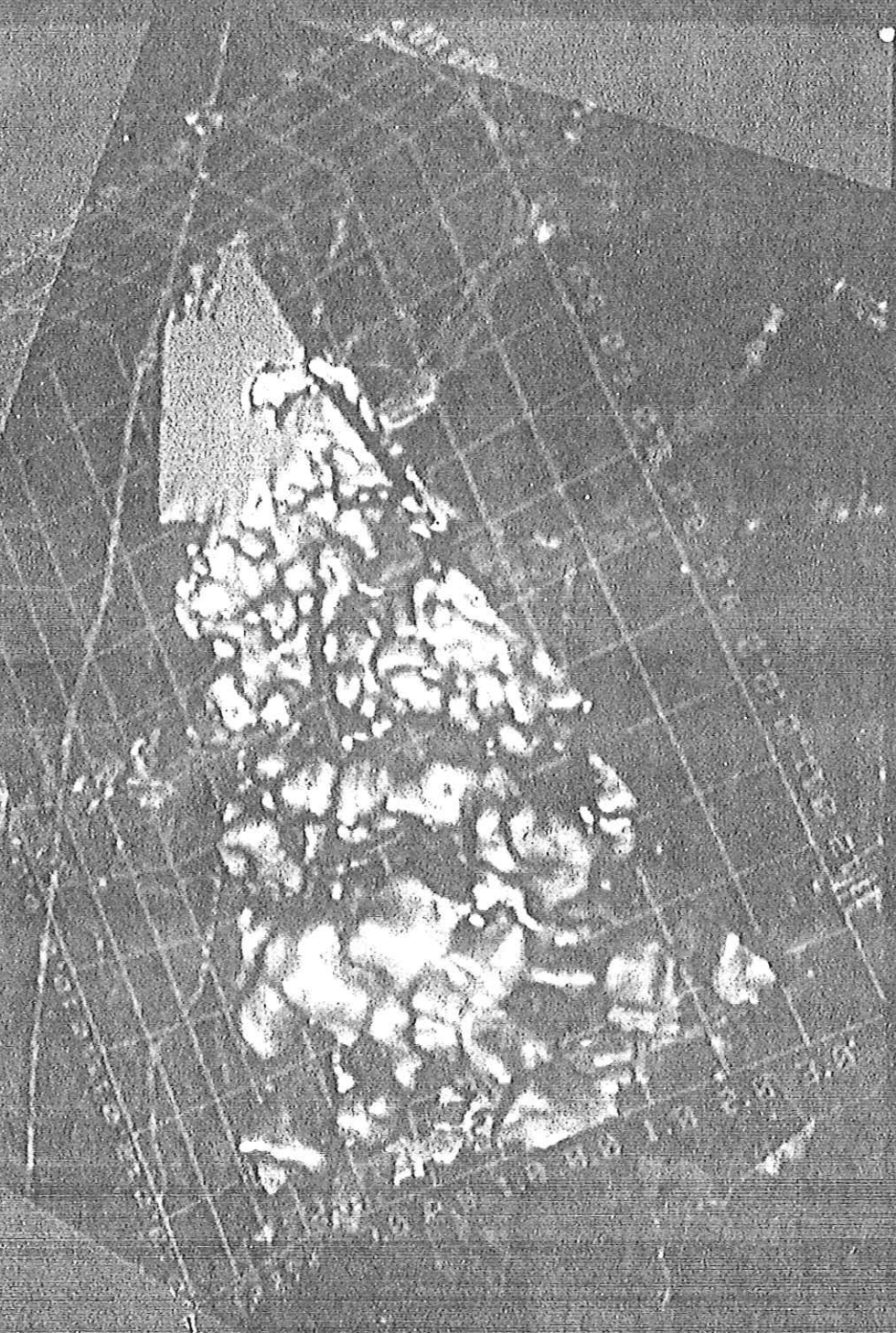


Figure 1.

University of Wisconsin
Volume Imaging Lidar
7-August-1989 9:45:19

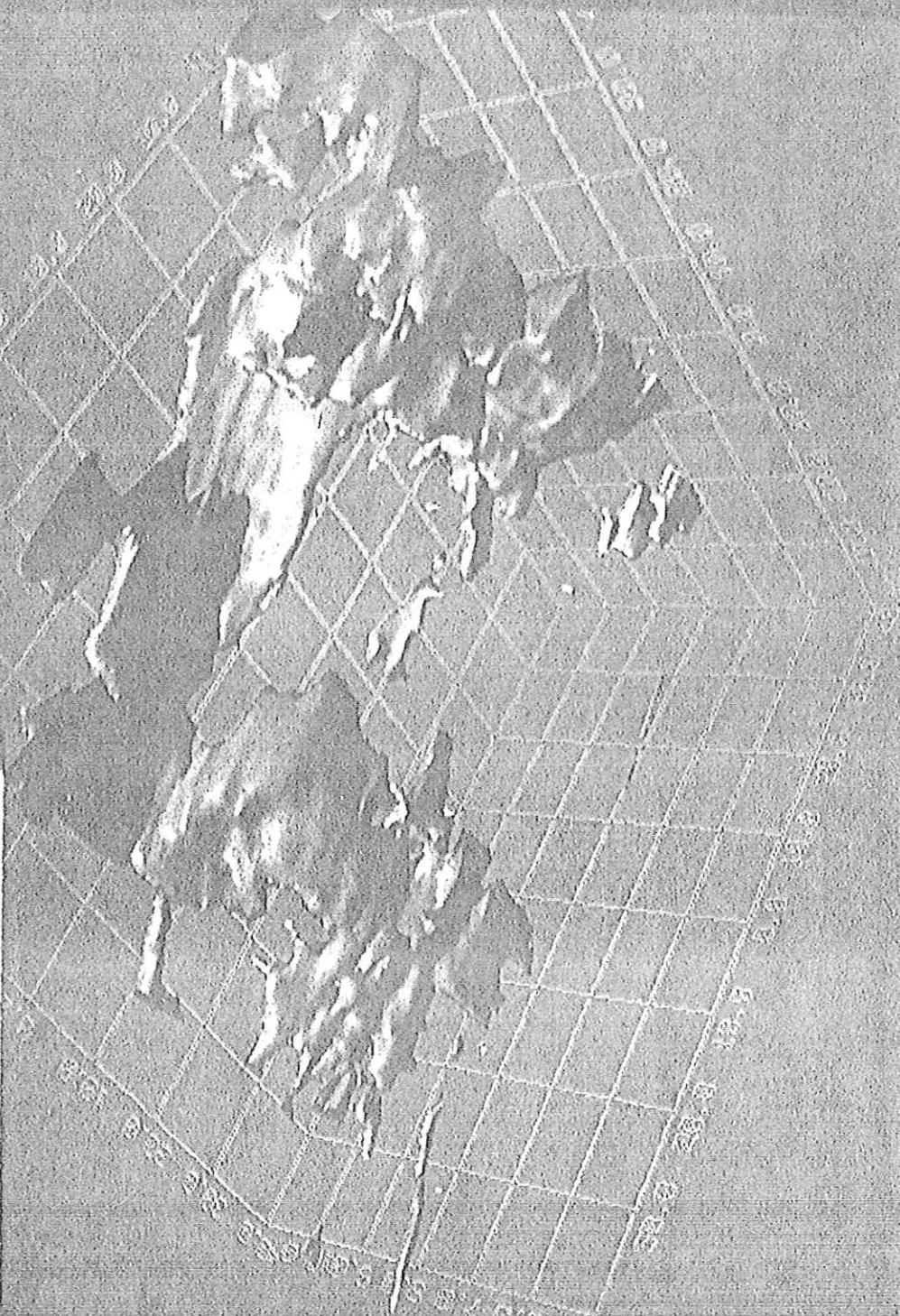


University of Wisconsin
Volume Imaging Lidar
1-Jul y-1987 11:23:03



University of Wisconsin
Volume Imaging Eider
70-November-1989 13:56:46

University of Wisconsin
Volume Imaging Lidar
1-December-1989 13:00:00



Lidar observations of banded convection during BLX83

Appendix B

R. A. Ferrare¹, J. L. Schols², E. W. Eloranta

Department of Meteorology, University of Wisconsin, Madison, WI 53706

R. Coulter

Environmental Research Division, Argonne National Laboratory, Argonne, IL 60439

Abstract

Lidar observations of clear air convection during the 1983 Boundary Layer Experiment (BLX83) reveal the presence of elongated, parallel regions of updrafts marked by enhanced aerosol backscattering. These linear (banded) aerosol structures were observed over a two hour period during a cloud-free morning. During this period, the depth of the Convective Boundary Layer (CBL) increased from 100 m to 1300 m. Wind speeds averaged over the depth of the CBL varied between 0 and 2 m/s, while the wind direction varied over a range of 160 degrees. The CBL instability parameter, $-Z_i/L$, increased from approximately 25 (weakly unstable) to 250 (strongly unstable). The spacings of the elongated, parallel plumes scaled with the CBL height. These findings suggest that secondary circulations in the form of horizontal roll vortices were present under conditions not normally associated with roll vortices. The lines of aerosol structures aligned much more closely (within 15 degrees) with the direction of the vertical shear of the horizontal wind through the depth of the CBL than with either the surface wind, mean CBL wind, or the wind at an altitude of $1.1 Z_i$.

¹Present affiliation: Universities Space Research Association and Laboratory for Atmospheres, Code 917, NASA/GSFC, Greenbelt, MD 20771

²Present affiliation: General Sciences Corporation, Laurel, MD 20707

1. Introduction

During recent years, observations of structures within the convective boundary layer have been made by various remote sensing techniques. Acoustic sounders (sodars) have observed the development and dissipation of convective thermals within the daytime mixed layer by measuring the small-scale temperature variations produced by thermals (Shaw, 1974; Nater and Richter, 1977). While producing excellent temporal records of convective plumes, sodars are unable to produce good spatial records of the development of convective structures.

Radars can discern structures within the boundary layer by measuring the reflectivity fields produced by small scale changes in the refractive index of air caused by temperature and moisture gradients (Konrad, 1970). In addition, single and dual-Doppler radars have observed the structure and dynamics of convective elements organized by horizontal roll circulations (Berger and Doviak, 1978; Hildebrand, 1980; Kelly, 1984). However, Doppler radars have significant problems sampling the lowest part of the Convective Boundary Layer (CBL) because of interference from ground clutter (Kelly, 1984). This problem may prohibit the observations of convective structures during the early morning, when the height of such structures may be only a few hundred meters.

The structures within the shallow CBL, which can not be measured by radar, can be measured by lidar (Kunkel et al., 1977). Lidar observes convective structures by measuring the light scattered by inhomogeneities in the aerosol concentration. These naturally occurring aerosol particles are carried into the boundary layer by convective plumes which originate from the surface through solar heating. Unlike tower, sodar, and airplane measurements, lidar can provide essentially instantaneous two-dimensional pictures of the CBL.

Because of this capability, lidar is a powerful tool which can be used to study organized convection in the CBL. Linear convection, which is referred to here in the geometric sense of being arranged in lines, has been often observed with horizontal roll vortices and banded structures (Woodcock, 1942; Plank, 1966; Kuettner, 1959, 1971; LeMone, 1973; Berger and Doviak, 1979; Kelly, 1984; Melfi et al., 1985) and predicted by various models (Kuo, 1963; Asai, 1970, 1972; Brown, 1972; LeMone, 1973; Sun, 1978; Shirer, 1980). This paper presents an analysis of elongated, parallel bands of enhanced aerosol backscattering observed by the University of Wisconsin ruby lidar system during

the 1983 Boundary Layer Experiment (BLX83). The observations of banded convection presented in this paper are unusual in that the convection occurred during light winds within a shallow boundary layer. Two-dimensional spectral and correlation analyses are used to objectively determine the geometrical properties of the observed aerosol structures and their relationship to the wind field in which they were embedded.

In this paper, the lidar instrumentation and data acquisition during the BLX83 field experiment are briefly described. The correlation and spectral analysis procedures used to determine the shape, wavelength, and orientation of the convective structures are then discussed. Next, the lidar measurements of wind speed and direction are briefly described. Finally, the lidar measurements are discussed in the context of the atmospheric conditions.

2. Experiment

The lidar data discussed in this paper were obtained on June 7, 1983 during BLX83, which took place from May 25 through June 18. A detailed review of this field experiment is given by Stull and Eloranta (1984). The primary field site was a flat wheat-alfalfa pasture located about five kilometers southeast of Chickasha, Oklahoma. The Argonne National Laboratory (ANL) facilities were at the center of the site with the University of Wisconsin lidar located on a small ridge 3.3 km south-southwest of the ANL site positioned to scan directly over the ANL instruments.

Personnel from ANL operated a kytoon based measurement system that provided vertical profiles of mean horizontal wind, temperature, and humidity in the lowest 800 m of the boundary layer at the primary field site. A three-component Doppler sodar system located at the ANL site measured the three wind velocity components as well as the thermal structure of the lowest 1.5 km of the boundary layer. Vertical fluxes of momentum, temperature, and moisture were measured from a 10 meter tower. The National Center for Atmospheric Research (NCAR) provided a network of 13 portable automated mesonet (PAM-II) stations; one of the PAM-II stations was located with the ANL instruments at the primary field site. This PAM-II station provided five minute averaged values of temperature, humidity, and wind velocity at a height of 10 meters.

3. Lidar Instrumentation and Data Acquisition

The University of Wisconsin lidar system which operated during BLX83 employed a pulsed ruby laser which emitted approximately 1 Joule pulses at a repetition rate of 0.9 Hz. The laser light backscattered by air molecules and aerosols was received using a 31 cm

diameter Newtonian telescope with a field of view adjusted to fully overlap the laser beam at a range of about 1 kilometer. An avalanche photodiode detected the collected light and provided an output signal which was logarithmically amplified and digitized. A 10 bit, 20 MHz analog-to-digital converter provided a range resolution of 7.5 meters with a maximum range of 7.68 kilometers in normal operation. A PDP-11/40 minicomputer controlled the laser scanning and normalized the signal for range square attenuation and for shot-to-shot energy variations. The resulting signal was stored on magnetic tape and displayed in real-time by a video display system. A more complete description of the lidar system is given by Sroga et al. (1980) and Wilde et al. (1985).

The lidar data described here were collected between 0850 and 1115 CDT (CDT = GMT - 5 hours) on June 7 1983 using two scan modes: the Range-Height Indicator (RHI) scan, and the Plan Position Indicator (PPI) scan. In the RHI scanning mode the lidar remained pointed at an azimuth angle of 23.5 degrees (directly over the ANL facilities), while the elevation angles were scanned from 0.5 to 20.0 degrees by half degree steps. In the PPI mode the elevation angle was fixed at 1.5, 3.0, or 12.0 degrees, depending on the boundary layer height, while the azimuth angle was scanned between 3.5 and 43.5 degrees again using half degree steps. A PPI scan took about 90 seconds to complete. Scanning modes were alternated by acquiring three RHI scans followed by three PPI scans. This scanning sequence permitted a quasi-three dimensional view of the CBL.

4. Lidar Data Analysis

The data from the RHI scans were used to determine the heights of the bottom and top of the entrainment zone and the height of the CBL. These heights were determined visually from the lidar RHI pictures using the method described by Boers et al. (1984). The horizontal structure of the aerosol features was obtained from the PPI scan data. The description of the analyses procedures applied to the PPI data follows.

a. Image Enhancement

When entrained clear air from above the boundary layer mixes with the aerosol-laden air in the boundary layer, the large contrast in aerosol content that is present at the top of the boundary layer decreases. Thus, the variation in the returned signal decreases with altitude within the boundary layer so that it is difficult to display features both at the top and at the bottom of the CBL equally well using the raw data. Therefore, the PPI scan data were enhanced in order to obtain a uniform contrast over the entire area so that aerosol features

both within and at the top of the boundary layer could be distinguished. This enhancement procedure also removes any shot-to-shot variations which may be the result of small errors in the laser energy monitor.

The first step in the procedure consists of determining the average return signal over a range interval located well within the boundary layer (usually less than half the boundary layer height) for each of the shots in a PPI scan using

$$S_i = \frac{1}{l_2 - l_1} \sum_{l=l_1}^{l_2} S_{il} \quad (1)$$

where S_{il} is the natural logarithm of the normalized lidar return signal, i is the index for the i^{th} lidar shot (between 1 and 80), l is the index for the l^{th} range element (between 1 and 1024), and $(l_1 \text{ to } l_2)$ is the range segment located well within the boundary layer. Within this range interval, the aerosol contribution to the lidar return signal is approximately uniform over all shots in a PPI scan. After the average return signal over this range interval is computed for the entire PPI scan, the deviation from this mean is computed for each shot

$$S'_i = S_i - \frac{1}{N} \sum_{i=1}^N S_i \quad (2)$$

where $N = 80$ is the total number of shots in a PPI scan. Next, this deviation is used to compute the variation of return signal versus range for each shot

$$S''_{il} = S_{il} - S'_i \quad (3)$$

The enhancement is accomplished by using the minimum and average return signals over all shots for each range element computed from

$$S''_{l,\min} = \text{Min} (S''_{1l}, S''_{2l}, S''_{3l}, \dots, S''_{Nl}) \quad (4)$$

$$S''_{l,\text{ave}} = \frac{1}{N} \sum_{i=1}^N S''_{il} \quad (5)$$

The contrast normalization is then given by

$$S_{il}^* = \frac{S_{il}'' - \overline{S_{l,ave}''}}{\overline{S_{l,ave}''} - \overline{S_{l,min}''}} \quad (6)$$

An overbar indicates smoothing of these quantities over range using a 200 m running mean average. This length scale is chosen to be large enough to remove any anomalous lidar returns yet small enough to preserve small scale features.

Examples of enhanced PPI scans at 0846, 0947, and 1052 CDT are shown in figures 1a, 1b, and 1c respectively. These times represent three convective regimes observed by the lidar during the morning of June 7 and will be discussed in detail in section 5b. In these figures, the bright areas in the PPI scans represent regions of enhanced aerosol backscattering, while the darker regions correspond to clear air between the convective structures. The center azimuth angle of these scans is 23.5° (measured from magnetic north) while the elevation angles are 1.5° , 3.0° , and 12.0° respectively. The dark sector near the center of the PPI scan in figure 1a is due to the laser beam striking a nearby utility pole; the laser scanned above the pole when the PPI scans used the larger elevation angles at the later times.

The enhanced PPI scans were then transformed from polar to cartesian coordinates using a weighted bilinear interpolation. For this transformation, the x axis was chosen along the center azimuth direction (23.5°) in a PPI scan. The resolution of the cartesian grid was chosen appropriately to match the spatially-averaged resolution of the polar coordinate system as determined by the range resolution and the azimuthal angle increment between adjacent lidar shots.

b. Power Spectra

Power spectra and autocorrelation analyses were performed on these transformed PPI scan data to measure the geometrical properties of the aerosol structures, i.e. their organization and average size and shape. Spectral analysis was used to find the spacing between the aerosol structures in the lidar data. The procedure is similar to that employed by Leese and Epstein (1963) to quantify the patterns present in cloud fields observed by satellite. Briefly, the power spectral density (PSD) of a PPI scan is computed using the computationally efficient Fast Fourier Transform (FFT) technique (Otnes and Enochson, 1972). Before the FFT technique is applied, an image is linearly detrended to reduce undesired power near the central, zero-wavenumber pair and to minimize leakage from low

wavenumber components into the higher wavenumber region. This detrending has a "pre-whitening" effect on the spectrum. The discrete form of the FFT of an image on an two-dimensional grid with dimensions L_x and L_y is given by

$$F(k) = \sum_{m=1}^M \sum_{n=1}^N f(x) e^{-2\pi j k x} \quad (7)$$

where

- k = wave vector (k_x, k_y)
- k_x = wave number in x direction = $(i_x M_x) / (M L_x)$
- i_x = lag index in x direction ($-M/2 \leq i_x \leq M/2$)
- M_x = number of data points in x direction
- M = number of data points in x direction
- k_y = wave number in y direction = $(i_y N_y) / (N L_y)$
- i_y = lag index in y direction ($-N/2 \leq i_y \leq N/2$)
- N_y = number of data points in y direction
- N = number of data points in y direction
- j = imaginary unit, ($j = \sqrt{-1}$)
- x = data point coordinate on two dimensional grid with lidar at the origin
= $(x,y) = (m L_x / M_x, n L_y / N_y)$
- L_x/M_x = grid resolution in x direction
- L_y/N_y = grid resolution in y direction
- f = aerosol backscattered radiation intensity in an enhanced PPI scan

The number of points in the x and y directions were increased by adding zeroes to the data to equal a power of 2 in order to implement the two-dimensional FFT computer routine.

The FFT of the image is then used to compute the PSD

$$G(k) = 4 \frac{L_x}{M_x^2} \frac{L_y}{N_y^2} F^*(k) F(k) \quad (8)$$

where the asterisk denotes a complex conjugate. The PSD is multiplied by the wavenumbers k_x and k_y to obtain the spectral power (SP) at each wavenumber

$$P(k) = G(k) k_x k_y \quad (9)$$

The SP's for each of the three consecutive PPI scans were averaged together to increase the statistical significance of the spectral estimates. Figures 2a, 2b, 2c show three-dimensional views of the averaged SP's corresponding to the enhanced PPI images of figure 1. The SP's are symmetric about both axes. In these figures, the viewing position is located 220 degrees counterclockwise from the x axis, at 50 degrees elevation angle above the x-y plane, and at a distance of three times the diameter of the picture.

The aerosol patterns shown in wavenumber space in figures 2a, 2b, and 2c are shown as a function of horizontal distance in figures 3a, 3b, and 3c. The wave pattern and the orientation of the aerosol structures shown in figures 1 and 2 are easily seen in the autocorrelation function (ACF) shown in figure 3. The computation of the ACF and its relationship to the SP will be discussed in section 4c.

The spectral power is a measure of the contribution to the total variance of the aerosol backscattered radiation at wavenumber k , and can be interpreted as the square of the amplitude of a wave whose wavelength is

$$\lambda = \frac{1}{|k|} = \frac{1}{\sqrt{k_x^2 + k_y^2}} \quad (10)$$

These characteristics are shown in figure 4a. The direction of the crest of this wave measured counterclockwise from the x axis is

$$\phi = \tan^{-1} \left(\frac{k_x}{k_y} \right) \quad (11)$$

Since the x axis was oriented 23.5 degrees east of magnetic north, the map orientation of the crest of the wave is

$$\theta = 23.5 - \phi \quad (12)$$

The wavelength and orientation of the dominant aerosol patterns were obtained from the locations of the maxima within the spectral power distributions. A spectral peak was compared to a noise level to determine whether it was statistically significant; a detailed discussion is given in the Appendix. Whenever the spectral power contained a single maximum larger than the noise level, the PPI scan data show linearly organized bands. The average spacing between these bands is given by λ_{\max} . The determination of λ_{\max} is complicated by the fact that the two-dimensional spectral power distribution is only available at discrete points. Therefore, λ_{\max} is close, but not exactly equal to the wavelength at which the maximum value in the spectral power appears. The grid point with the largest spectral value and its eight neighboring spectral values are used to obtain a better estimate of the actual location of the maximum using a center of mass technique

$$\lambda_{\max} = \frac{1}{\sqrt{k_{x,\max}^2 + k_{y,\max}^2}} \quad (13)$$

where

$$k_{x,\max} = \frac{1}{D} \sum_{m=-1}^1 \sum_{n=-1}^1 P(i_x+m, i_y+n) \frac{(i_x+m) M_x}{M L_x} \quad (14)$$

$$k_{y,\max} = \frac{1}{D} \sum_{m=-1}^1 \sum_{n=-1}^1 P(i_x+m, i_y+n) \frac{(i_y+n) N_y}{N L_y} \quad (15)$$

$$D = \sum_{m=-1}^1 \sum_{n=-1}^1 P(i_x+m, i_y+n) \quad (16)$$

and $P(i_x+m, i_y+n)$ is the value of the spectral power at the grid point (i_x+m, i_y+n) . The orientation of the bands is given by the direction θ of the crest of the wave corresponding to the wavelength λ_{\max} . If more than one maximum appears in the spectral power distribution, the aerosol structure pattern in the PPI scan looks more complex.

The errors and limitations associated with these spectral computations are discussed in the Appendix. The maximum relative error in λ_{\max} is 10% with a maximum error of 10 degrees in the orientation of the wave associated with λ_{\max} . The minimum resolvable wavelength averaged over the entire area of the PPI scan is approximately 80 m.

c. Autocorrelations

The shapes of the aerosol structures were estimated using autocorrelation functions computed from the PPI scan data. The autocorrelation function (ACF) is calculated from the inverse FFT of the PSD, which results in the autocovariance function

$$\text{ACV}(\Delta\mathbf{x}) = \frac{M_x N_y}{4 M N} \sum_{i=1}^M \sum_{l=1}^N G(\mathbf{k}) e^{2\pi j \mathbf{k} \Delta\mathbf{x}} \quad (17)$$

where $\Delta\mathbf{x} = (\Delta x, \Delta y)$ is a lag vector. The ACF is computed from the ACV using

$$\text{ACF}(\Delta\mathbf{x}) = \frac{\text{ACV}(\Delta\mathbf{x})}{\sigma^2} \quad (18)$$

where the variance σ^2 of the image is given by

$$\sigma^2 = \frac{1}{(M_x N_y - 1)} \sum_{m=1}^{M_x} \sum_{n=1}^{N_y} [f(x) - f_{\text{ave}}(x)]^2 \quad (19)$$

where

$$f_{\text{ave}}(x) = \frac{1}{M_x N_y} \sum_{m=1}^{M_x} \sum_{n=1}^{N_y} f(x) \quad (20)$$

As in the case of the spectral power distributions, the ACF's from three consecutive PPI scans are averaged together to reduce the statistical error. The ACF corresponding to the enhanced PPI scans at 0846, 0947, and 1052 CDT are shown in figure 3.

A typical ACF in this data set has an elliptically shaped peak with a maximum value of unity centered around lag distances of zero as shown in figure 4b. The ellipse represents a particular contour level in the ACF. In the present study, various contour values were chosen. For contour values less than 0.5, the orientations and shapes of the ellipses did not significantly change. The ratio of the semi-major axis b to the semi-minor axis a is used to determine the elongation of the observed aerosol patterns. The angle of the semi-major axis also indicates the orientation of the aerosol structures on the PPI scan. The error in the estimate of the average shape of the aerosol structures is basically determined by the variability of the position of the specified contour line in the ACF. For the present data, the

relative error in the measured elongation of the aerosol structures was estimated to be between 25 to 30%. A more complete description is given in the Appendix.

In order to study the mechanisms responsible for the observed aerosol structures, horizontal wind vectors were estimated by measuring the cross correlation between aerosol patterns on two PPI scans separated in time (Schols and Eloranta, 1990). The distance the aerosol structures drifted between the two scans and the direction of movement were found from the positions of the maxima of the cross-correlation functions (CCF) computed between the two scans. Values of the mean horizontal wind velocity at different heights in the CBL were obtained using subdomains located at various positions within the PPI scans and by assuming horizontal uniformity. The accuracy of the present lidar wind velocity measurements depends on the errors in determining both the maximum correlation lag distance in the CCF's and the local time separation between the two PPI scans. Wind speed errors less than 0.1 m/s and wind directional errors less than 10 degrees have been demonstrated with this technique (Schols and Eloranta, 1990). The lidar-derived winds are compared to the winds measured by the kytoon and sodar in the next section.

5. Results

a. Velocity Measurements

A comparison of the wind speeds derived from the lidar data during the morning of June 7 with those measured by sodar and kytoon is shown in figure 5a; a similar comparison for wind directions is shown in figure 5b. The comparisons between the lidar, sodar, and kytoon winds above the ANL site shown in figure 5 were made at heights and times that matched as closely as possible. The sodar continuously acquired five minute averaged values of the vertical profile of the horizontal wind velocity until 09:45 CDT. The first kytoon wind velocity profile began at 08:30 CDT when the kytoon began its ascent. The kytoon ascended to a maximum altitude of 375 m at 09:00 CDT and then descended, reaching the surface about 40 minutes later. A second cycle was then repeated, with the kytoon reaching 360 m at 10:06 CDT and returning to the surface at 10:25 CDT.

The differences between the lidar-derived wind speeds and directions with those measured by the sodar and kytoon are primarily due to different methods of sampling by the various instruments. The lidar winds were averaged in space by the area covered by a subdomain with a PPI scan (on the order of a few square kilometers) and in time by the duration of a PPI scan (about 90 seconds). In contrast, the kytoon wind measurements

were averages over a few minutes of the wind velocity in the immediate vicinity of the kytoon. The sodar wind velocity measurements were vertical Eulerian soundings inside the CBL.

b. Evolution of Banded Structures

On the morning of June 7 a region of high pressure with strong subsidence was centered over Oklahoma. During the lidar observational period discussed here, which ran from 08:50 CDT to 11:15 CDT, the sky was cloud-free. The winds throughout the CBL during this morning were less than 3 m/s. Figure 6 shows the lidar-derived wind speed and direction averaged over the depth of the CBL. Boundary layer stability was computed for this period using the parameter $-Z_i/L$ where Z_i is the height of the CBL and L is the Obukhov length. The CBL height Z_i was derived from the lidar RHI scan data, virtual potential temperatures were obtained from the kytoon profiles, and wind speeds were obtained from the lidar data and the PAM-II surface data. Since surface fluxes and friction velocities could not be measured when wind speeds were less than 1 m/s, these parameters were estimated during most of the morning of June 7 so that the resulting L values are rough estimates. The friction velocities were obtained from surface winds and the roughness length measurements made by the ANL facilities. The surface buoyancy fluxes were estimated from the sensible and latent heat fluxes measured at the ANL flux tower later on June 7 and during other days during BLX83 when conditions were similar. Further details of these computations are given by Ferrare (1984). The CBL height Z_i and the instability parameter $-Z_i/L$ are shown in figure 7.

During the lidar observational period, three convective regimes were observed. The first and last regimes were separated by a period during which the CBL grew rapidly, the winds became calm, and the instability of the CBL increased dramatically. For each regime, the spectra and autocorrelation functions derived from the lidar data were used to find the dominant wavelength, orientation, and average size and shape of the observed aerosol structures. The orientation of these aerosol structures did not change over the depth of the CBL. This was confirmed by performing the autocorrelation and spectral analyses on subdomains within the PPI scans; the locations of these subdomains corresponded to various heights in the CBL. The results of the analyses on these subdomains were similar to the results of the analyses performed over the entire PPI scans.

The evolution of the shape and orientation of the aerosol structures is presented in figure 8 by a series of ellipses whose shape and orientation change throughout the

morning. While these ellipses correspond to a contour level of $ACF = 0.05$, the shape and orientation of the ellipses shown in figure 6 do not change appreciably for ACF values less than about 0.5. The horizontal wind vector averaged over the depth of the CBL, and the vertical shear vector of the horizontal wind over the CBL are also shown. The vertical shear of the horizontal wind across the depth of the CBL was estimated by taking the difference between the lidar measured wind at the top of the CBL and the surface wind measured by the PAM-II station. Between 09:47 CDT and 10:20 CDT no shear vectors are displayed because the nearly calm winds produced unreliable estimates of the vertical shear, and because the lidar elevation angle permitted observation of winds over only 60 to 90% of the rapidly growing CBL. A measure of the elongation of the structures is shown in figure 9, where the elongation is defined by the ratio of the semi-major axis to the semi-minor axis. The orientation of the aerosol structures and the direction of the vertical shear of the horizontal wind are also shown in figure 10 along with the surface wind direction obtained from the PAM-II data, the wind direction averaged over the CBL measured by the lidar, and the wind direction just above the CBL at an altitude of $1.1 Z_i$ also measured by the lidar.

During the first convective period, which occurred from 0830 CDT to 0936 CDT, the convective plumes were small and were organized into bands. During this period, the average wind direction over the depth of the CBL was from the northwest, while the average wind speed was about 1 m/s as shown in figure 6. Figure 7 indicates that the CBL appeared only weakly convective as the instability parameter $-Z_i/L$ increased from 20 to 60. The CBL was shallow, slowly increasing in height from 100 meters to 180 meters. At the start of this first period, the convective bands were aligned with both the CBL average wind direction, and the direction of the vertical shear of the horizontal wind across the boundary layer. While the direction of the average wind remained approximately constant throughout the first convective period, both the wind shear across the CBL and the orientation of the aerosol bands veered with respect to the average wind. At 0913 CDT, the surface wind began backing, causing a gradual veering of the vertical shear with respect to the orientation of the bands.

During the second convective period, which occurred from 0947 CDT to approximately 1026 CDT, the size of the individual aerosol plumes quickly increased, and the elongation of the plumes decreased. As shown in figure 7, the height of the CBL also increased rapidly from 200 m to 600 m as well as $-Z_i/L$ which increased from 60 to 250.

The CBL winds were nearly calm, and the orientation of the aerosol structures remained essentially constant.

During the third convective period, which occurred after 1026 CDT, the lidar PPI scans revealed elongated individual convective plumes rather than the earlier banded structure. While the plumes are believed to have been organized into bands, the size of the plumes had become so large that the number of plumes within a PPI scan was too small to support this assumption. The decrease in the PPI scan size relative to the CBL height throughout this part of the morning of June 7 can be seen in figure 11. The stability of the CBL did not change significantly. During this third period, the CBL continued to grow rapidly, rising from 625 m to 1300 m at 1112 CDT. The CBL average wind direction became easterly and the wind speed increased to about 2 m/s. The plume elongation, shown in figure 9, increased in response to this increase in wind speed. The aerosol convective structures were again aligned parallel to the vertical shear vector of the horizontal wind across the CBL. The average CBL wind direction was aligned approximately 45° clockwise to the orientation of the aerosol structures.

The changes in the wind direction and speed observed during these periods suggest that the transition from downslope drainage flow to thermally-driven upslope flow occurred during this morning. The light winds measured near 10:00 CDT would correspond to this flow reversal. These directions appear consistent with the local topography. Since high pressure was centered over central Oklahoma during this time, the weak synoptic forcing would have permitted such a thermally driven flow to dominate near the surface.

Throughout this two hour period, the direction of the vertical shear of the horizontal wind across the CBL depth correlated well with the orientation of the banded aerosol structures. It should be emphasized that, while the average wind direction within the CBL changed from 310° to 110°, the linear aerosol structures remained aligned to the shear and not the mean horizontal wind. The aerosol bands remained parallel (within 15°) to the direction of this vertical shear. The spacing, λ_{\max} , between the aerosol bands measured during the first convective period scaled with the height of the CBL. Figure 11 shows the ratio λ_{\max}/Z_i measured by the lidar throughout the morning; this ratio varied between 2.0 to 2.5 between 0846 and 1020 CDT. The decrease in the PPI scan sector relative to the height of the CBL, thereby decreasing the number of patterns which could be observed within in scan, contributed to this effect.

6. Discussion

In an attempt to explain the reason for the linear convection pattern observed by the lidar, topographical maps and aerial photographs of the area surrounding the lidar PPI scan sector were examined. These maps and photos revealed no apparent land use patterns or surface features which could generate the orientations recorded in the lidar measurements. The lidar measurements of the orientations of the aerosol structures and wind directions indicate that during the first convective period the orientation of the aerosol structures changed by as much as 40° while the average wind direction within the CBL showed no significant variations. Therefore, it would appear unlikely for the linear aerosol pattern to have been produced by a particular surface feature outside of the immediate area and then to have advected into the lidar PPI scan sector.

The linear organization of the aerosol structures was visible throughout the depth of the CBL, while the spacing of the aerosol structures scaled with the depth of the CBL. These observations suggest that secondary circulations in the form of horizontal roll vortices were present. The present observations of roll circulations can be compared to the summary given by Kelly (1984) for models, laboratory experiments, and field experiments of roll circulations. When using the period before 0945 CDT when the lidar PPI sector scan was large enough to permit adequate sampling, the roll wavelengths found from the spectral analysis of the lidar data range from 200 m to about 500 m. These values are at the low end of the range reported by Kelly (1984). However, defining the roll aspect ratio as λ_{\max}/Z_i , the aspect ratios shown in figure 9 lie in the range predicted by models (1.5-4.0) and within the range (1-10) observed in field experiments. It is not surprising that the roll wavelengths found in the current study lie on the low end of the range of previously observed range since the CBL depths over which the lidar observations were made are considerably smaller than those in previous observations.

In previous roll observations, the roll orientation has been measured with respect to either the mean CBL wind or to the geostrophic wind at the top of the CBL. Previous observations of roll vortices have observed the roll orientation angle to vary from -30° to 20° with respect to the mean boundary layer wind and the geostrophic wind at the top of the CBL (Kelly, 1984). In the present case, the orientations of the aerosol structures were measured with respect to the vertical shear of the horizontal wind, the mean CBL wind, the surface wind, and the wind at a height of $1.1 Z_i$. These orientation angles are shown in figure 12. The orientation angles are positive for wind vectors which lie to the right

(clockwise) of the axes of the aerosol structures. If comparisons are made for the first and third periods discussed above, then the alignment of the aerosol structures varied between 40 degrees to the right or 120 degrees to the left of the mean CBL wind. Even larger variations are present when the orientations are measured with respect to the surface wind. The variation in orientation angle is less when the orientation is measured with respect to the wind at a height of $1.1Z_i$. In this case the angles vary from about -15° to 50° . More importantly, however, the orientation of the aerosol structures does not vary more than 15 degrees with respect to the vertical shear of the horizontal wind. This suggests that the vertical shear is more appropriate for measuring the orientation rather than the mean CBL wind.

Previous observations have shown that roll circulations occur predominantly with winds speeds greater than 5 to 8 m/s (LeMone, 1973; Kuettner, 1959, 1971; Berger and Doviak, 1979; Kelly, 1984). The present lidar study indicates that the bands can also form at lower wind speeds. While the winds speeds are less in the current study, the CBL depth is also considerably less than in previous observations, suggesting that the vertical shear of the horizontal wind over the CBL may be comparable to the shear in prior observations. It is also interesting to note that during most of the period when the bands were observed, the boundary layer was very unstable, as shown in figure 7. Many previous observations have shown rolls to occur in neutral to slightly unstable boundary layers ($-Z_i/L < 25$). However, observations by Kelly (1984) and the present lidar observations indicate that roll circulations may occur in very unstable boundary layers.

The lidar measurements of elongated convective plumes, which were observed later in the observational period, are similar to previous observations of plumes which have occurred on a variety of scales. As shown in figure 9, the lidar measurements have shown the convective plumes to be elongated with the ratio of longitudinal to transverse diameters to range vary between 2 to 5. Lenschow (1970) measured velocity and temperature fields associated with thermals in the CBL and also found the thermals to be elongated in the direction of the mean wind.

Wilczak and Tillman (1980) measured the structure of large scale convective plumes in the surface layer using an array of temperature sensors and the 300 m Boulder Atmospheric Observatory tower. They noted that as the static stability decreased, the ratio of downwind to crosswind dimension of the plumes also decreased. Davison (1975) measured the horizontal cross sectional shape of convective plumes at a height of 3.5 m in the surface layer using temperature measurements. The investigation, which was

performed under moderately strong wind conditions (about 10 m/s), found that the thermals were elongated in the direction of the mean wind. The elongation is larger in moderate to strong winds than in light wind conditions. In the present lidar study, both the increase in the CBL instability and the decrease in the CBL average wind speed during the second convective period clearly contributed to the decrease in the elongation of the convective structures (see figure 9). The plume elongation increased again as the wind speed increased during the third convective period.

7. Conclusion

Lidar data collected on the morning of June 7, 1983 during the BLX83 experiment reveal linearly organized regions of updrafts marked by enhanced aerosol scattering. These linear aerosol structures were observed during cloud-free conditions. The dimensions, wavelengths, and orientations of these structures are computed from the lidar PPI scan data using power spectra and autocorrelation analyses. Wind velocities within the Convective Boundary Layer (CBL) are estimated by measuring the cross correlation between aerosol patterns inside successive PPI scans. These lidar-derived wind velocities show excellent agreement with those measured by kytoon and Doppler sodar.

The linear organization of the aerosol structures was observed throughout the depth of the CBL as the CBL height increased from 100 to 1300 m during the observational period. The spacing of the aerosol structures varied between $2.0Z_i$ to $2.5Z_i$ while the banded aerosol structures were observed. While the orientation of the linear aerosol structures did not correlate well with the mean CBL wind, the structures are found to remain aligned (within 15 degrees) with the shear vector across the CBL. The lidar observations of the linear aerosol structures across the depth of the CBL combined with observation that the spacing between the linear patterns scaled to the CBL depth suggest that secondary circulations in the form horizontal roll vortices were present. The lidar observations indicated that these roll circulations disappeared during the middle part of the observational period when boundary layer winds became calm.

Lidar measurements during the latter part of the observation period, when the convective plume size became comparable to the PPI scan area, show the convective plumes were elongated with the ratio of longitudinal to transverse diameters varying between 2 and 5. This elongation increased as the wind speed increased. These elongated plumes are found to remain aligned with the shear of wind across the CBL.

8. Appendix

Error Analyses

a. Spectra

The statistical error present in the spectral calculations is used to determine whether a maximum is significant and actually presents a pattern on a PPI scan or whether the maximum has arisen by chance. We assume $P(k)/E[P(k)]$ is distributed as χ^2/f (Blackman and Tukey, 1958), where $P(k)$ is the estimate of the spectral power, $E[P(k)]$ is the expected value of $P(k)$, χ^2 is a chi-square variable, and f the number of degrees of freedom. For a relatively flat spectrum f is at least equal to 11, when the number of lags in each dimension is taken equal to half the size of the data points (Leese and Epstein, 1963). Assuming random noise $P_n(k)$, the expected value of the spectral noise $E[P_n(k)]$ is given by the average of the spectral power over the wavenumber domain. To determine the significance of a maximum of $P(k)$ at a confidence level of $1 - \alpha$, the upper α per cent limit of χ^2/f is considered. Then if the signal-to-noise ratio $SNR = P(k)/E[P_n(k)]$ is larger than χ^2/f , the peak is considered to be real. For the present data, a 99% confidence level with 11 degrees of freedom requires a SNR greater than 2.3 for a maximum in the power spectrum to be considered significant. By averaging successive spectra this minimum requirement is reduced since the reliability of the spectral estimate improves due to the increase in the number of degrees of freedom.

The inverse of the SNR of the spectral maximum is used to calculate the error in the exact location of the spectral peak. For example, if the SNR is low, indicating a relatively broad spectral peak, the resulting uncertainty in the location of the spectral peak is large. The uncertainty in the grid point location can be found by assuming that the spectral peak has the shape of a normal curve. The standard deviation of that curve in units of lag index is equal to $1/(SNR (2\pi)^{1/2})$ and forms a measure of the error in the grid point location of the spectral peak. Peaks observed at small wavenumbers have the largest relative error in their measured position. For the present data this uncertainty is smaller than 0.17, indicating that the error in its position is at most 10%. This results in a maximum relative error of 10% in λ_{max} and a maximum error of 10 degrees in the orientation of the wave corresponding to λ_{max} .

The minimum resolvable wavelength is limited primarily by the azimuthal angle increment between adjacent shots. Using the present angular separation of 0.5 degree, the

angular resolution ranges from 20 m at a range of 2300 m to 60 m at a range of 6900 m. This translates to minimum resolvable wavelengths of 40 m and 120 m respectively, with an average over an entire PPI scan of approximately 80 m. The maximum detectable wavelength is limited by the dimensions of the data domains on the PPI scans. These dimensions are in turn limited by the laser repetition rate and the emitted energy of the laser. The estimate of λ_{\max} becomes unreliable when its value exceeds half the domain size. The spectral resolution can be improved by either choosing larger numbers of lags, or by increasing the grid spacing. Both methods reduce the number of degrees of freedom and the reliability of the spectral estimates. In the present case the grid spacing was increased in the third convective period.

b. Autocorrelations

The error in the estimate of the average shape of the aerosol structures is basically determined by the variability of the position of the specified elliptic contour line in the ACF. The uncertainty in the location of a point on the contour line depends on the error in the estimate of the ACF and the grid resolution. If we assume that the ACF damps out exponentially, its variance can be written in the one-dimensional case as (Box and Jenkins, 1976)

$$\sigma_{\text{ACF}}^2(i) = \frac{1}{N} \left[\frac{(1 + \alpha^2)(1 - \alpha^{2i})}{1 - \alpha^2} - 2i\alpha^{2i} \right] \quad (21)$$

where i is the lag index, N is the number of data points, and α is the base of the exponential, (i.e. $A(i) = \alpha^{|i|}$, $-1 < \alpha < 1$). If α is not close to unity, for large lag numbers this becomes

$$\lim_{i \rightarrow \infty} \sigma_{\text{ACF}}^2(i) = \frac{1}{N} \left[\frac{1 + \alpha^2}{1 - \alpha^2} \right] \quad (22)$$

Averaging three successive ACF's together reduces the variance by a factor of three. The errors in the lengths of the axes of the ellipse in the ACF were evaluated by changing the ACF contour level over an amount that is equal to σ_{ACF} , measured along the directions of the ellipse axes. For the present data, the relative error of the average of three successive ACF's was between 2% and 5%, thereby producing relative errors between 10% and 20% in the axes of the ellipse. The accompanying relative error in the measured elongation of the aerosol structures was between 25% and 30%.

Acknowledgements

The material used in this article was based on the University of Wisconsin Department of Meteorology M.Sc. thesis by Richard Ferrare. Dan Forrest's vast computer experience was tapped to write the much of the code that was necessary to carry out the calculations and display the pictures. Thanks go to our colleagues Drs. Louis Garand and Tim Crum for their helpful discussions. We acknowledge the field collection and analysis of the kytoon and sodar data made by Mr. Tim Martin and Dr. Marvin Wesely of Argonne National Laboratory, and the PAM-II surface measurements done by personnel from NCAR. The comments of an anonymous reviewer are also appreciated. This research was sponsored by grants of NSF ATM-8211842 and ARO DAAG29-80-K-0079, DAAL03-86-K-0024 and by the U.S. Department of Energy; Assistant Secretary for Energy Research, Office of Health and Environmental Research, under contract W-31-109-Eng-38. This paper was completed during Richard Ferrare's work with Universities Space Research Association at NASA/Goddard Space Flight Center.

References

- Asai, T., 1970 : Three dimensional features of thermal convection in a plane Couette flow. *J. Meteor. Soc. Japan*, 48, 18-29.
- Asai, T., 1972 : Thermal instability of a shear flow turning the direction with height. *J. Meteor. Soc. Japan*, 50, 525-532.
- Berger M. I. and R. J. Doviak, 1979 : An analysis of the clear air planetary boundary layer wind synthesized from NSSL's dual Doppler-radar data. NOAA-ERL-NSSL-87, National Severe Storms Laboratory, Norman ,OK, 55pp.
- Blackman, R. B. and J. W. Tukey, 1958 : The measurement of power spectra, New York, Dover Publications, Inc., 180 pp.
- Boers, R., E.W. Eloranta, and R.L. Coulter, 1984: Lidar observations of mixed layer dynamics: Tests of parameterized entrainment models of mixed layer growth rate. *J. Clim. Appl. Meteor.*, 23, 247-266.
- Box, G.E.P., and G.M. Jenkins, 1976: Time Series Analysis, Holden-Day, San Francisco, 575 pp.
- Brown, R. A., 1972 : On the inflection point instability of a stratified Ekman boundary layer. *J. Atmos. Sci.*, 29, 850-859.

- Davison, D. G., 1975 : The horizontal cross-sectional shape of convective plume. *Quart. J. Roy. Meteor. Soc.*, **101**, 463-473.
- Ferrare, R. A., 1984 : Lidar observations of organized convection within the atmospheric mixed layer. M. Sc. thesis, Department of Meteorology, University of Wisconsin Madison, 204 pp.
- Hildebrand, P.H., 1980: Multiple Doppler radar observations of PBL structure. Preprints 19th Conference on Radar Meteorology, Miami Beach, Amer. Meteor. Soc., 656-661.
- Kelly, R. D., 1984 : Horizontal roll and boundary-layer interrelationships observed over lake Michigan. *J. Atmos. Sci.*, **41**, 1816-1826.
- Khalsa, S. J. S., 1980 : Surface-layer intermittency investigated with conditional sampling. *Boundary-Layer Meteor.*, **19**, 135-153.
- Konrad, T.G., 1970: The dynamics of the convective processes in the clear air as seen by radar. *J. Atmos. Sci.*, **27**, 1138-1147.
- Kuettner, J. P., 1959 : The band structure of the atmosphere. *Tellus*, **2**, 267-294.
- Kuettner, J. P., 1971 : Cloud Bands in the Earth's Atmosphere. Observations and Theory. *Tellus*, **23**, 404-426. .
- Kunkel, K. E., E. W. Eloranta and S. T. Shipley, 1977 : Lidar observations of the convective boundary layer. *J. Appl. Meteor.*, **16**, 1306-1311.
- Kuo, H. L., 1963 : Perturbations of plane Couette flow in stratified fluid and origin of cloud streets. *Physics Fluids*, **6**, 195-211.
- Leese, J. A. and E. S. Epstein, 1963 : Application of two-dimensional spectral analysis to the quantification of satellite cloud photographs. *J. Appl. Meteor.*, **2**, 629-644.
- LeMone, M. A., 1973 : The structure and dynamics of horizontal roll vortices in the planetary boundary layer. *J. Atmos. Sci.*, **30**, 1077-1091.
- Lenschow, D. H., 1970 : Airplane measurements of planetary boundary layer structure. *J. Appl. Meteor.*, **9**, 874-884.
- Melfi, S. H., J. D. Spinhirne, S-H. Chou and S. Palm, 1985 : Lidar observations of vertically organized convection in the planetary boundary layer over the ocean. *J. Climate Appl. Meteor.*, **24**, 806-821.

- Otnes, R. K. and L. Enochson, 1972 : Digital time series analysis. John Wiley & Sons, Inc. N.Y., 384 pp.
- Nater, W. and H. Richter, 1977: Thermal plumes detected by an acoustic echo sounder. *J. Appl. Meteor.*, **16**, 986-989.
- Plank, V. G., 1966 : Wind conditions in situations of pattern form and nonpattern form cumulus convection. *Tellus*, **18**, 1-12.
- Schols, J. L. and E. W. Eloranta, 1990 : The calculation of area-averaged vertical profiles of the horizontal wind velocity using the University of Wisconsin three-dimensional volume imaging lidar data. submitted to *J. Appl. Meteor.*
- Shaw, N.A., 1974: Observations of atmospheric structure using an acoustic sounder. Argonne National Lab Report, ANL/RER/75-2, (November, 1974).
- Shirer, H. N., 1980 : Bifurcation and stability in a model of moist convection in a shearing environment. *J. Atmos. Sci.*, **37**, 1586-1602.
- Sroga, J. T., E. W. Eloranta and T. Barber, 1980 : Lidar measurement of wind velocity profiles in the boundary layer. *J. Appl. Meteor.*, **19**, 598-605.
- Stull, R. B. and E. W. Eloranta, 1984 : Boundary Layer Experiment 1983. *Bull. Amer. Meteor. Soc.*, **65**, 450-456.
- Sun, W. Y., 1978. Stability analysis of deep cloud streets. *J. Atmos. Sci.*, **35**, 466-483.
- Wilczak, J. M. and J. E. Tillman, 1980 : The three-dimensional structure of convection in the atmospheric surface layer. *J. Atmos. Sci.*, **37**, 2424-2443.
- Wilde, N. P., R. B. Stull and E. W. Eloranta, 1985 : The LCL zone and cumulus onset. *J. Appl. Meteor.*, **24**, 640-657.
- Woodcock, A., 1942 : Soaring over the open sea. *Sci. Mon.*, **55**, 226-232.

Figures

Figure 1. (a) Enhanced lidar PPI scan at 08:46 CDT on June 7. The bright areas represent enhanced aerosol scattering while the darker regions correspond to clear air between the structures. The x axis represents horizontal distance away from the lidar while the y axis represents the distance away from the center shot. The dark sector near the center of the scan is due to missing data caused by the laser beam hitting a nearby utility pole. The elevation angle of this scan was 1.5 degrees.

Figure 1. (b) same as (a) except for 09:47 CDT. The elevation angle was 3.0 degrees.

Figure 1. (c) same as (a) except for 10:52 CDT. The elevation angle was 12.0 degrees.

Figure 2. (a) Average spectral power: (SP) at 08:46 CDT. The SP is symmetric about the x and y axes. The viewing position is located at 220 degrees counterclockwise from the x axis, at 50 degrees above the horizontal plane, and at a distance of three times the picture diameter. The wavenumbers along the x and y axes are shown as km^{-1} .

Figure 2. (b) same as (a) except for 09:47 CDT.

Figure 2. (c) same as (a) except for 10:52 CDT.

Figure 3. (a) Average autocorrelation function (ACF) at 08:46 CDT. The ACF is symmetric about the origin. The lag distances along the x and y axes are shown as km.

Figure 3. (b) same as (a) except for 09:47 CDT.

Figure 3. (c) same as (a) except for 10:52 CDT.

Figure 4. (a) Wave in an image as characterized by its wavelength, λ , and its crest orientation, θ measured clockwise from magnetic north. The angle between the crest of the wave and the x axis (the center azimuth direction in a PPI scan) is ϕ . The orientation of the x axis is 23.5 degrees east of magnetic north ($\theta = 23.5 - \phi$). (b) Ellipse representing the average shape and orientation of the aerosol structures as estimated from the ACF. The ratio of the semi-major to semi-minor axes b/a measures the elongation of the aerosol structures.

Figure 5. (a) Comparison of the wind speeds derived from the lidar data with those measured by kytoon and Doppler sodar. The comparisons were made for heights and times that matched as closely as possible with the kytoon and sodar measurements. (b) Same as (a) except for wind directions. The lidar-derived wind speeds show excellent agreement with those measured by kytoon and Doppler sodar; differences in wind speed are less than 0.2 m/s and differences in wind direction are less than 20 degrees.

Figure 6. Lidar derived wind speed and direction averaged over the depth of the CBL during the morning of June 7, 1983. The first of the three convective regimes observed by the lidar occurred from 0830 CDT to 0936 CDT when the convective plumes were small and organized into bands. The second regime occurred between 0947 CDT to 1026 CDT, when the winds became calm, and the plumes rapidly grew in size. The third convective period occurred after 1026 CDT when the PPI scans showed elongated individual large plumes.

Figure 7. CBL height and instability parameter $-Z_i/L$ during the morning of June 7. Z_i was obtained from the lidar RHI data while L was determined from the ANL surface flux and kytoon data.

Figure 8. Shape and orientation of the aerosol structures represented by ellipses obtained from autocorrelation function (ACF) analyses of the lidar PPI scan data. These ellipses represent a specified contour level in the ACF. The mean CBL wind (dotted line) and the vertical shear of the wind over the depth of the CBL (solid line) determined from the lidar data are also shown.

Figure 9. Elongation of the aerosol structures during the morning of June 7. The elongation is defined as the ratio of the semi-major axis to the semi-minor axis of the specified contour line in the ACF.

Figure 10. The directions of the vertical shear of the wind over the CBL, mean CBL wind, surface wind, and the wind at a height of $1.1 Z_i$. The orientation of the aerosol structures is also shown.

Figure 11. The aspect ratio of the aerosol structures, defined as the ratio of the dominant spectral wavelength λ_{\max} to the CBL height Z_i , for the morning of June 7. The width of the PPI scan area ΔY normalized to the CBL height Z_i is also shown. After 1020 CDT the λ_{\max}/Z_i values became unreliable because of the limitations imposed by the horizontal dimensions of the lidar PPI scan area.

Figure 12. Orientation of the aerosol structures with respect to: the direction of the vertical shear of the wind over the CBL, the mean CBL wind, the surface wind, and the wind at an altitude of $1.1 Z_i$. Orientation angles are positive for wind vectors which lie to the right (clockwise) of the axes of the aerosol structures.

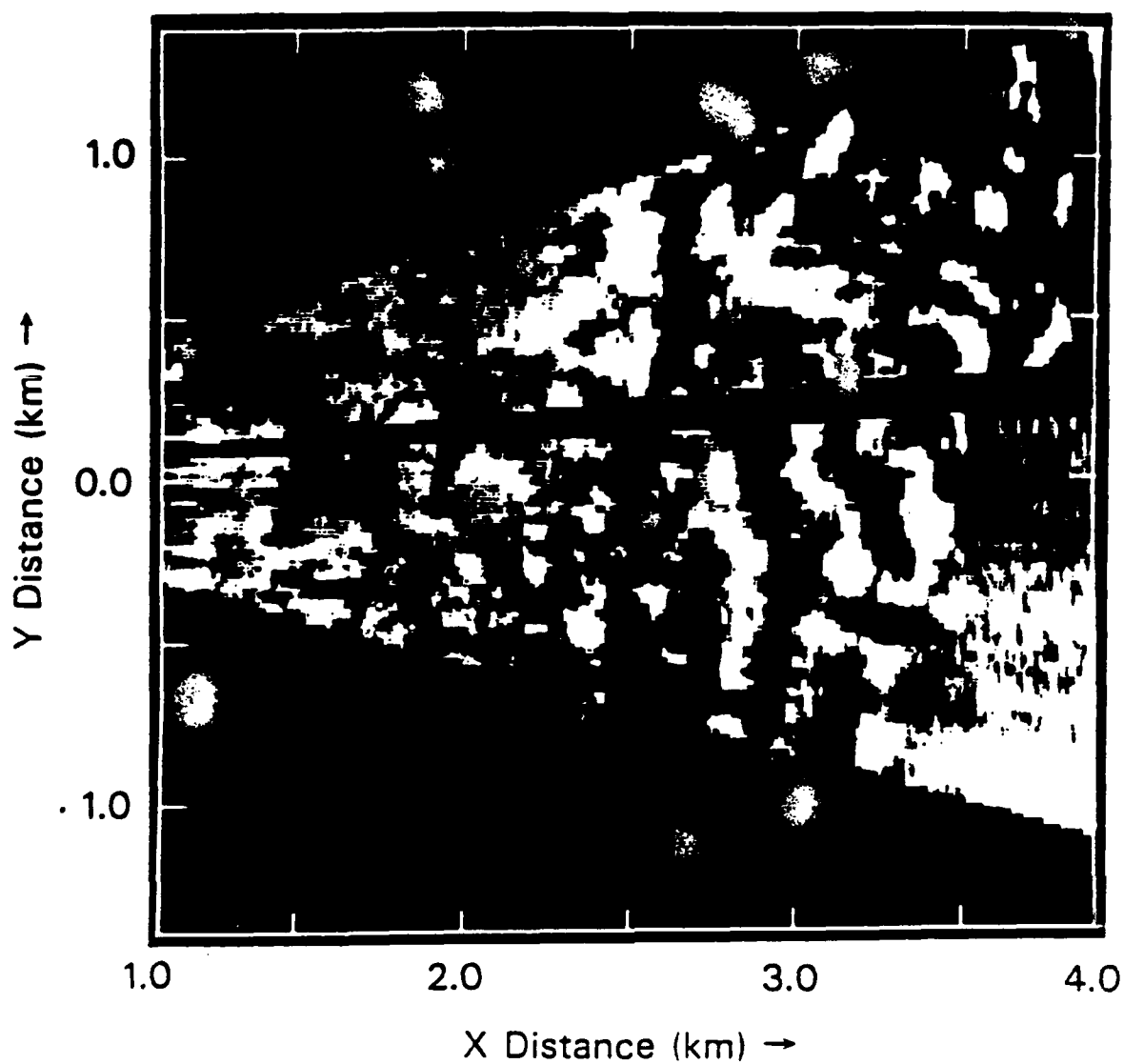


Figure 1. (a) Enhanced lidar PPI scan at 08:46 CDT on June 7. The bright areas represent enhanced aerosol scattering while the darker regions correspond to clear air between the structures. The x axis represents horizontal distance away from the lidar while the y axis represents the distance away from the center shot. The dark sector near the center of the scan is due to missing data caused by the laser beam hitting a nearby utility pole. The elevation angle of this scan was 1.5 degrees.

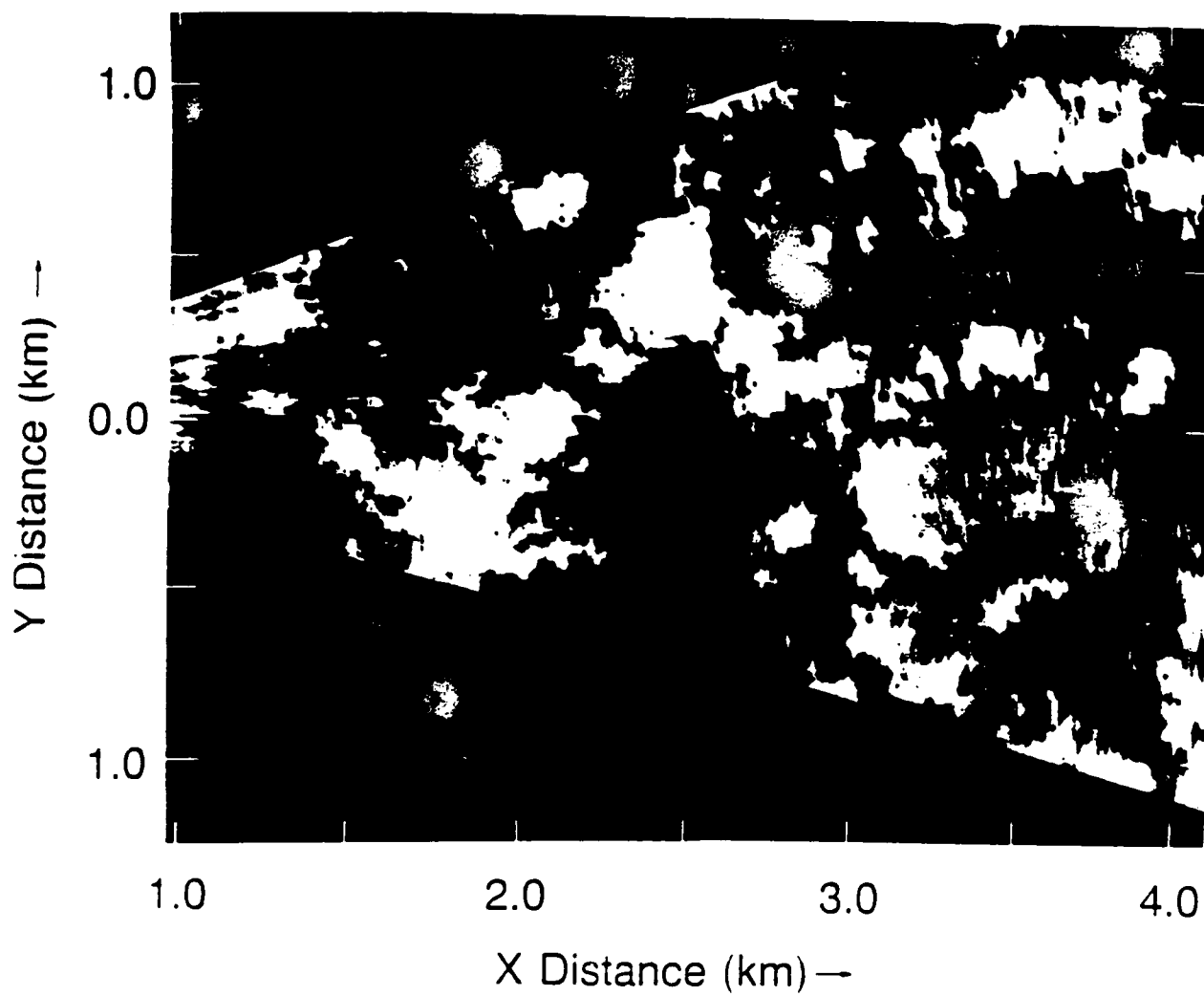


Figure 1. (b) same as (a) except for 09:47 CDT. The elevation angle was 3.0 degrees.

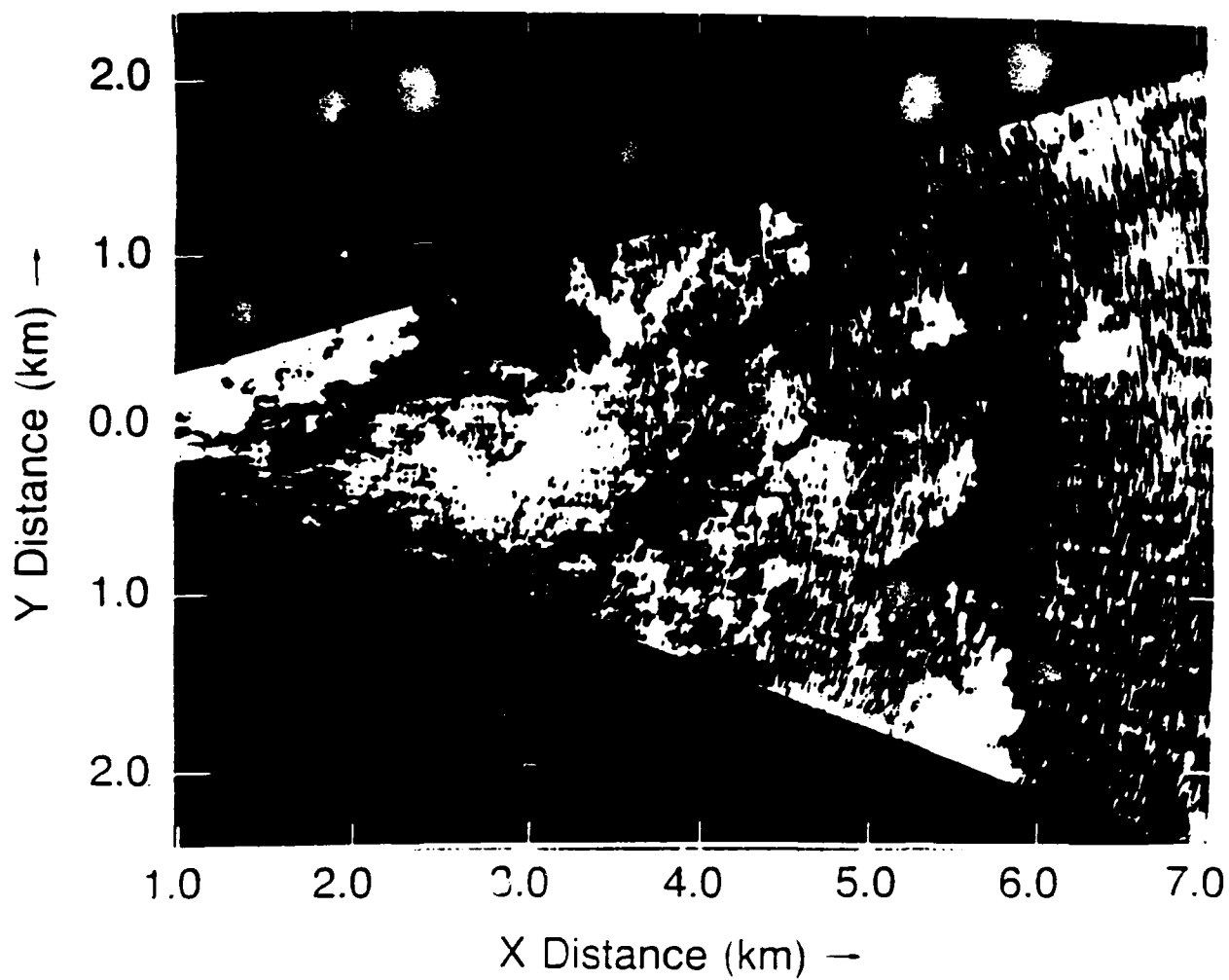


Figure 1. (c) same as (a) except for 10:52 CDT. The elevation angle was 12.0 degrees.

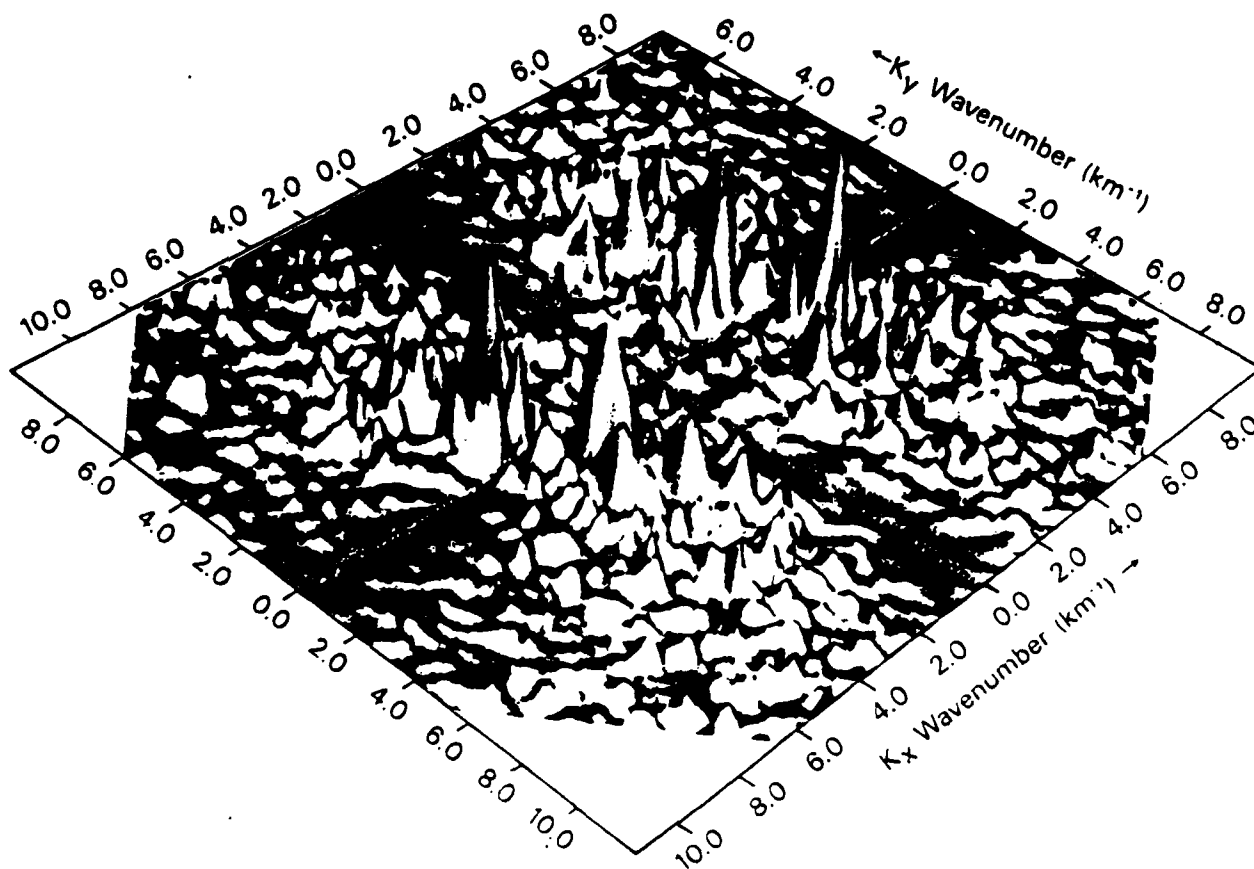


Figure 2. (a) Average spectral power (SP) at 08:46 CDT. The SP is symmetric about the x and y axes. The viewing position is located at 220 degrees counterclockwise from the x axis, at 50 degrees above the horizontal plane, and at a distance of three times the picture diameter. The wavenumbers along the x and y axes are shown as km^{-1} .

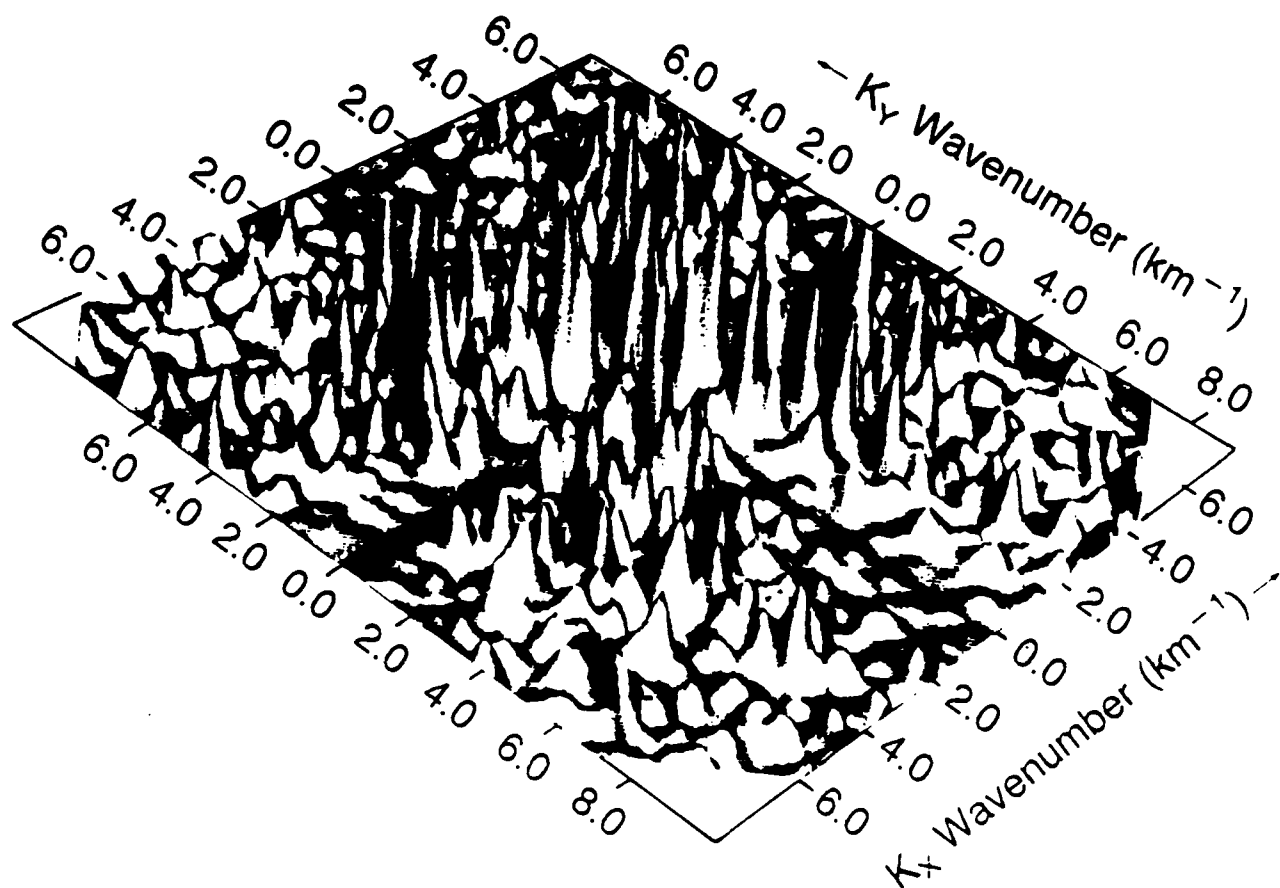


Figure 2. (b) same as (a) except for 09:47 CDT.

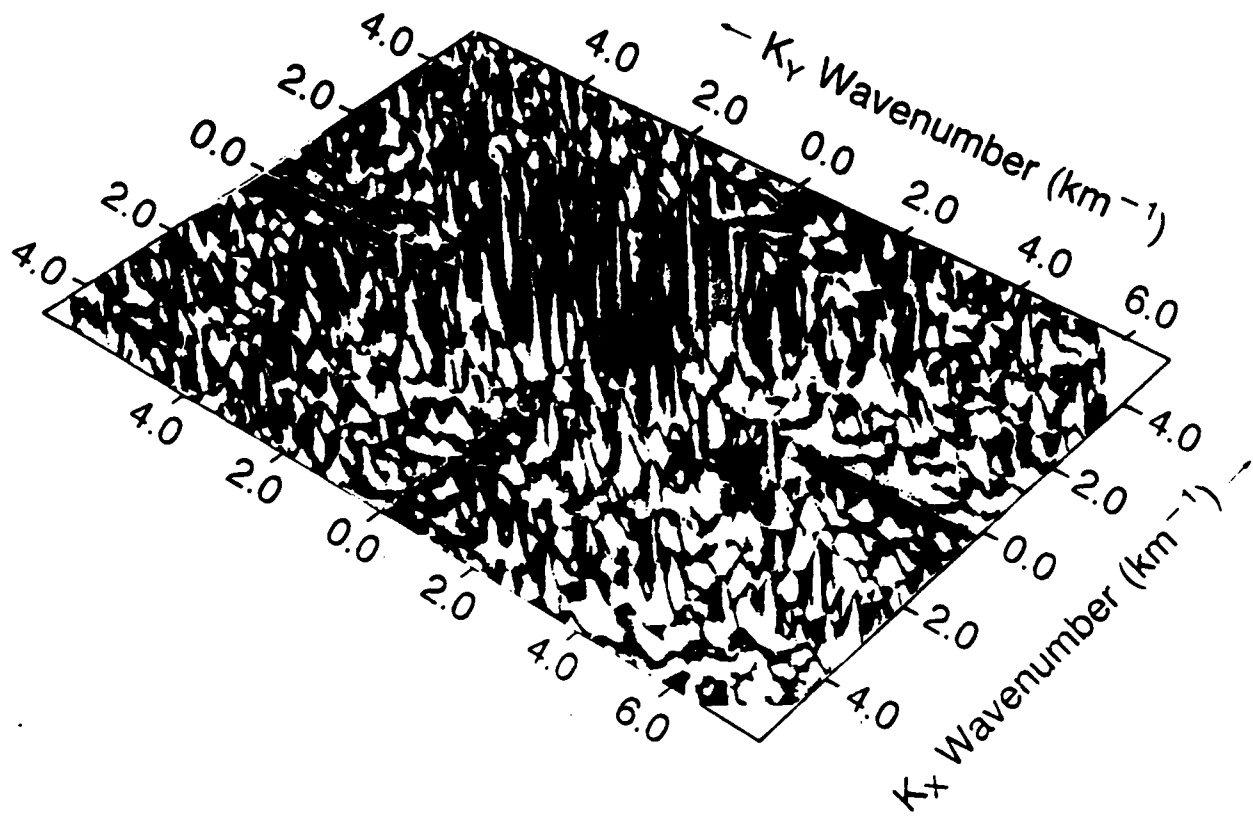


Figure 2. (c) same as (a) except for 10:52 CDT.

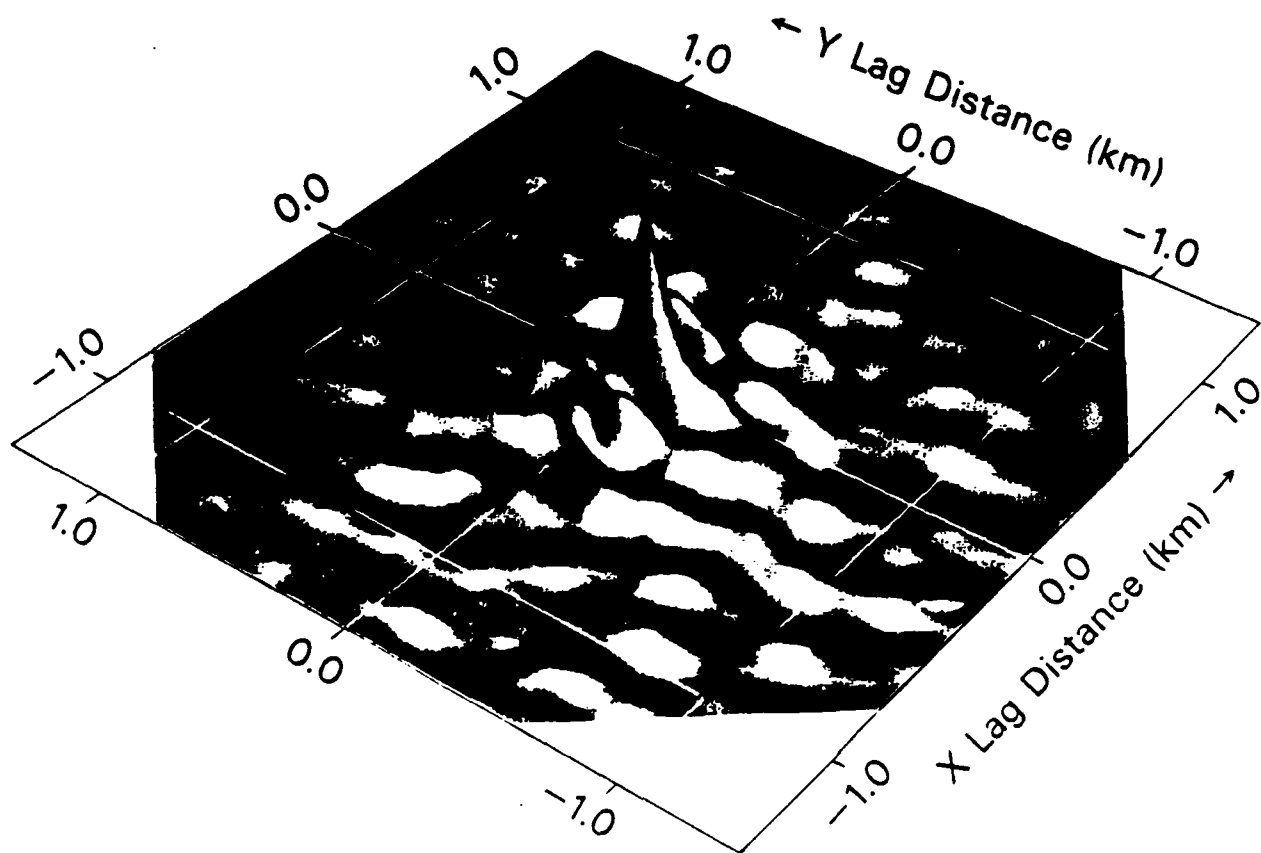


Figure 3. (a) Average autocorrelation function (ACF) at 08:46 CDT. The ACF is symmetric about the origin. The lag distances along the x and y axes are shown as km.

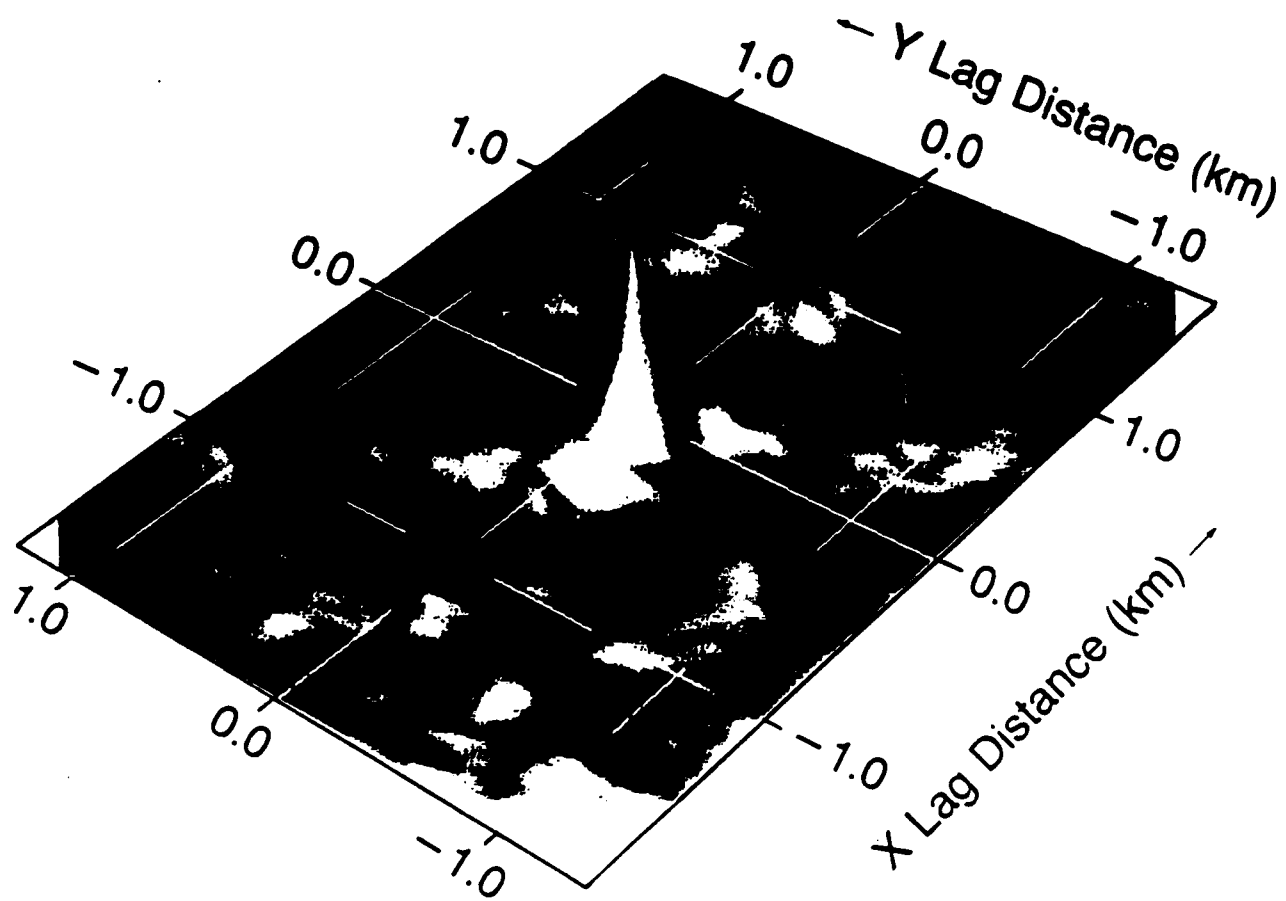


Figure 3. (b) same as (a) except for 09:47 CDT.

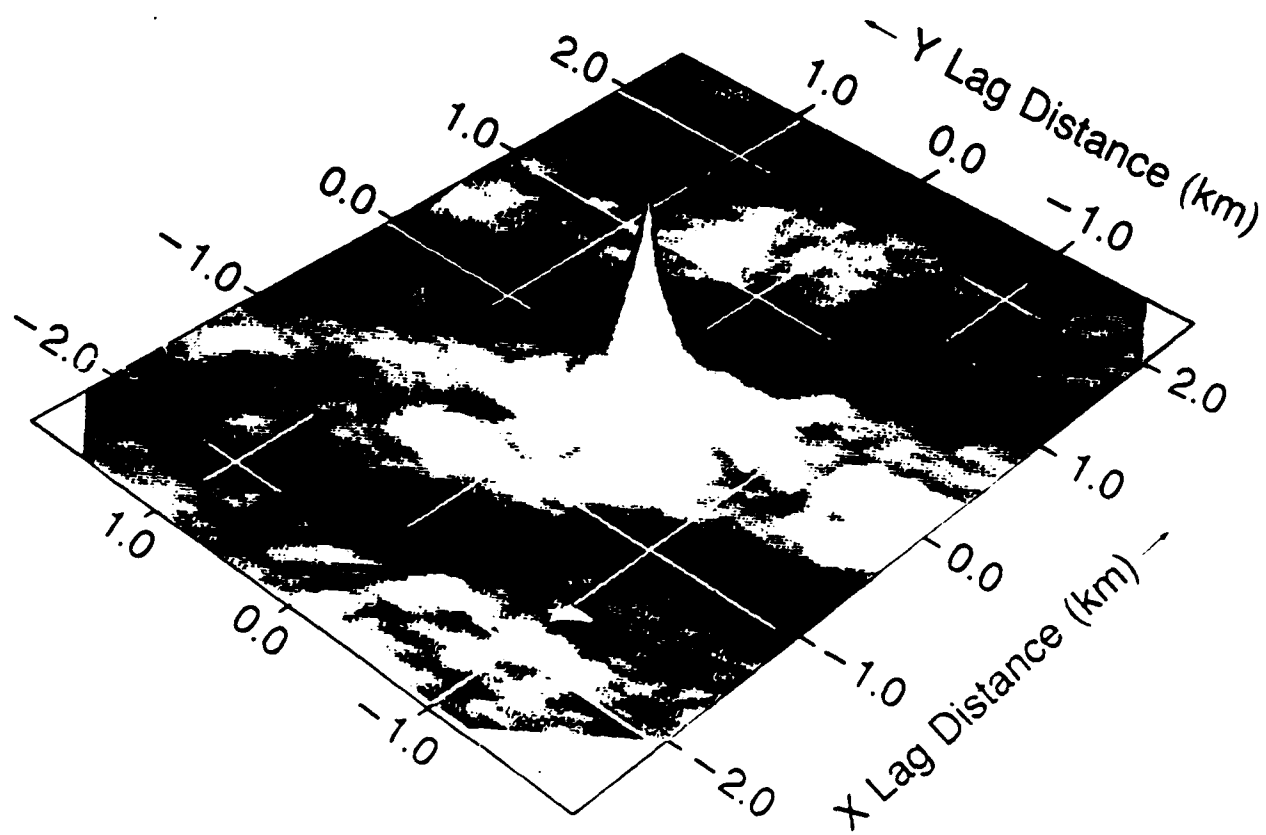


Figure 3. (c) same as (a) except for 10:52 CDT.

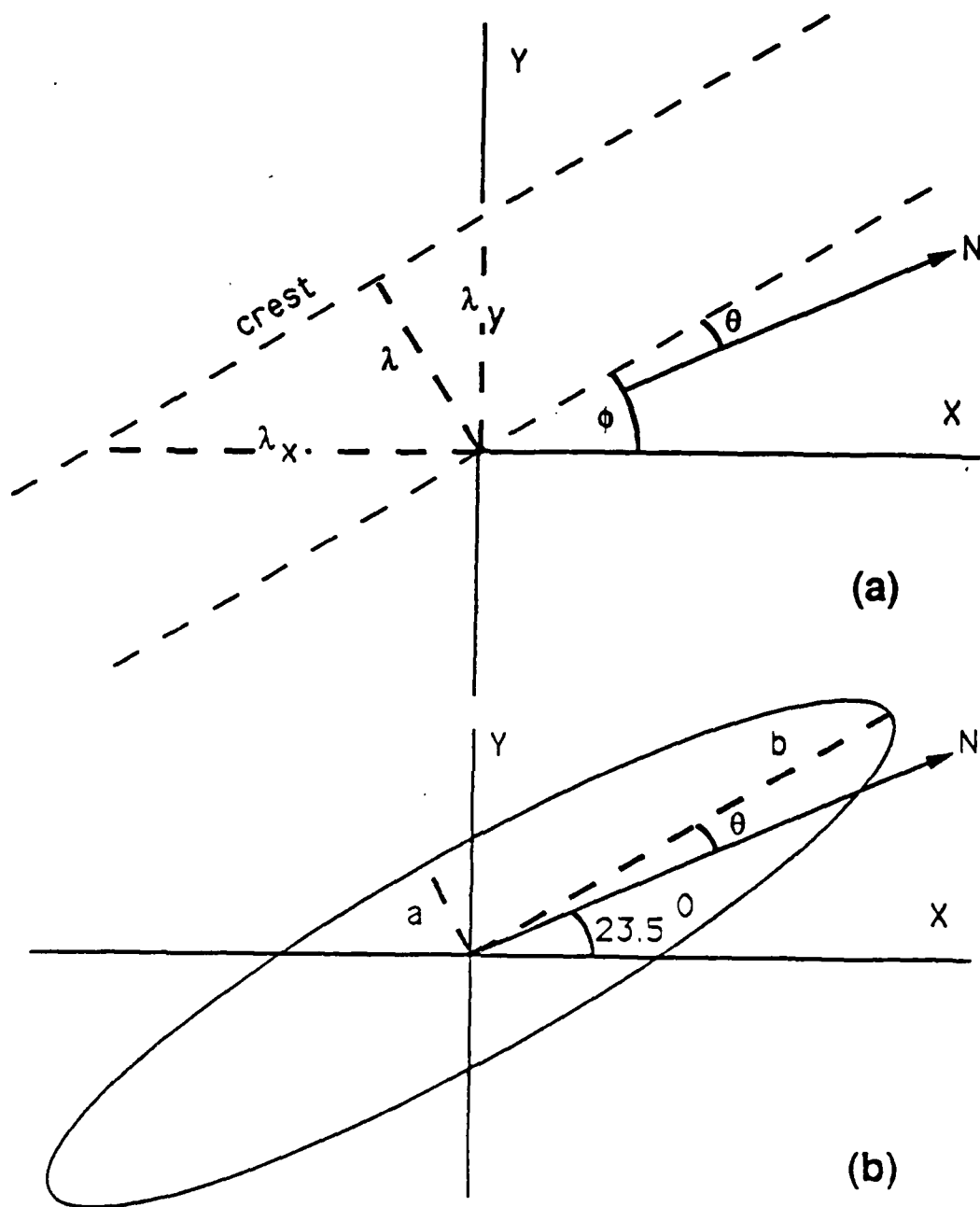


Figure 4. (a) Wave in an image as characterized by its wavelength, λ , and its crest orientation, θ measured clockwise from magnetic north. The angle between the crest of the wave and the x axis (the center azimuth direction in a PPI scan) is ϕ . The orientation of the x axis is 23.5 degrees east of magnetic north ($\theta = 23.5 - \phi$). (b) Ellipse representing the average shape and orientation of the aerosol structures as estimated from the ACF. The ratio of the semi-major to semi-minor axes b/a measures the elongation of the aerosol structures.

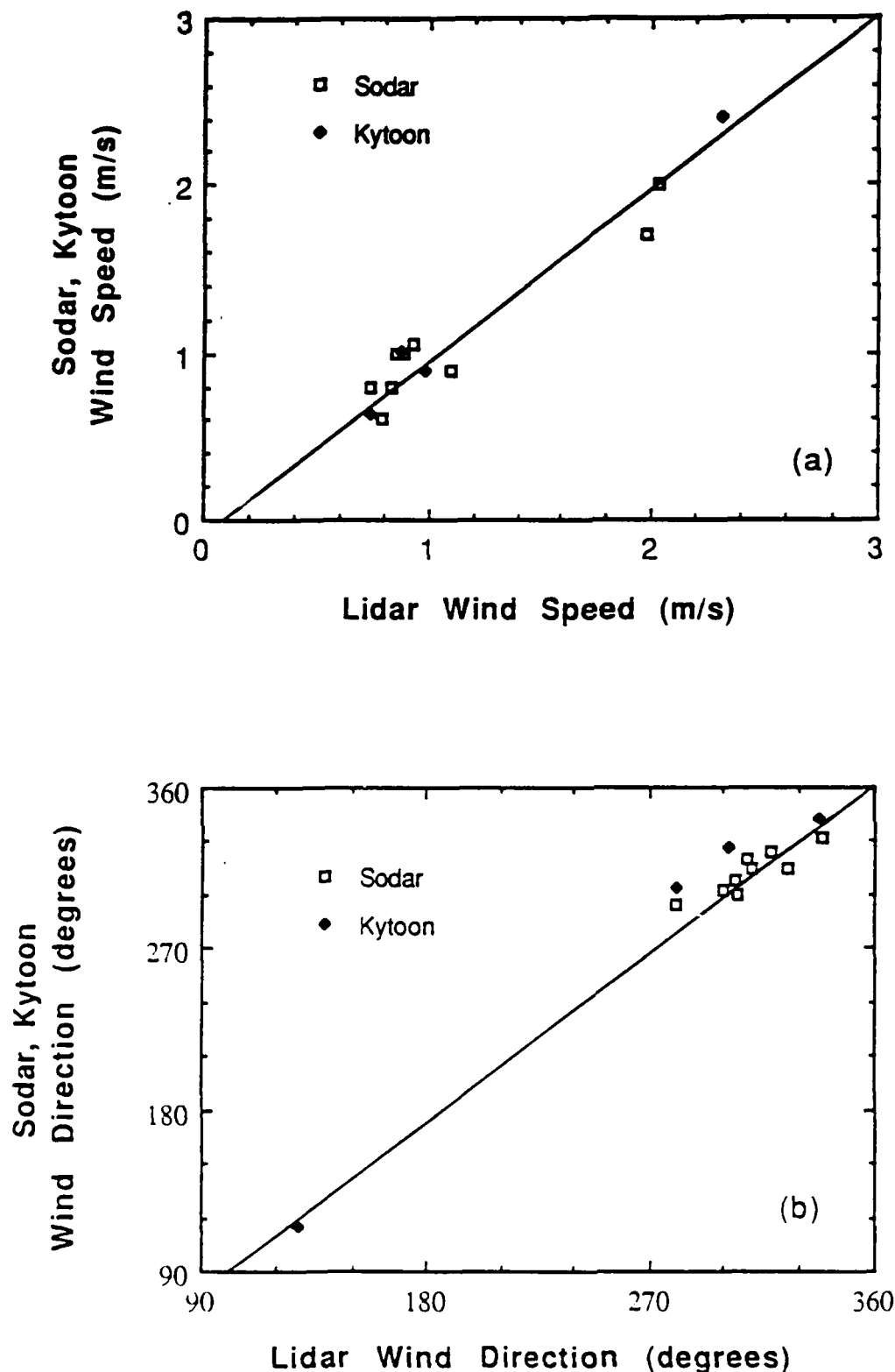


Figure 5. (a) Comparison of the wind speeds derived from the lidar data with those measured by kytoon and Doppler sodar. The comparisons were made for heights and times that matched as closely as possible with the kytoon and sodar measurements. (b) Same as (a) except for wind directions. The lidar-derived wind speeds show excellent agreement with those measured by kytoon and Doppler sodar; differences in wind speed are less than 0.2 m/s and differences in wind direction are less than 20 degrees.

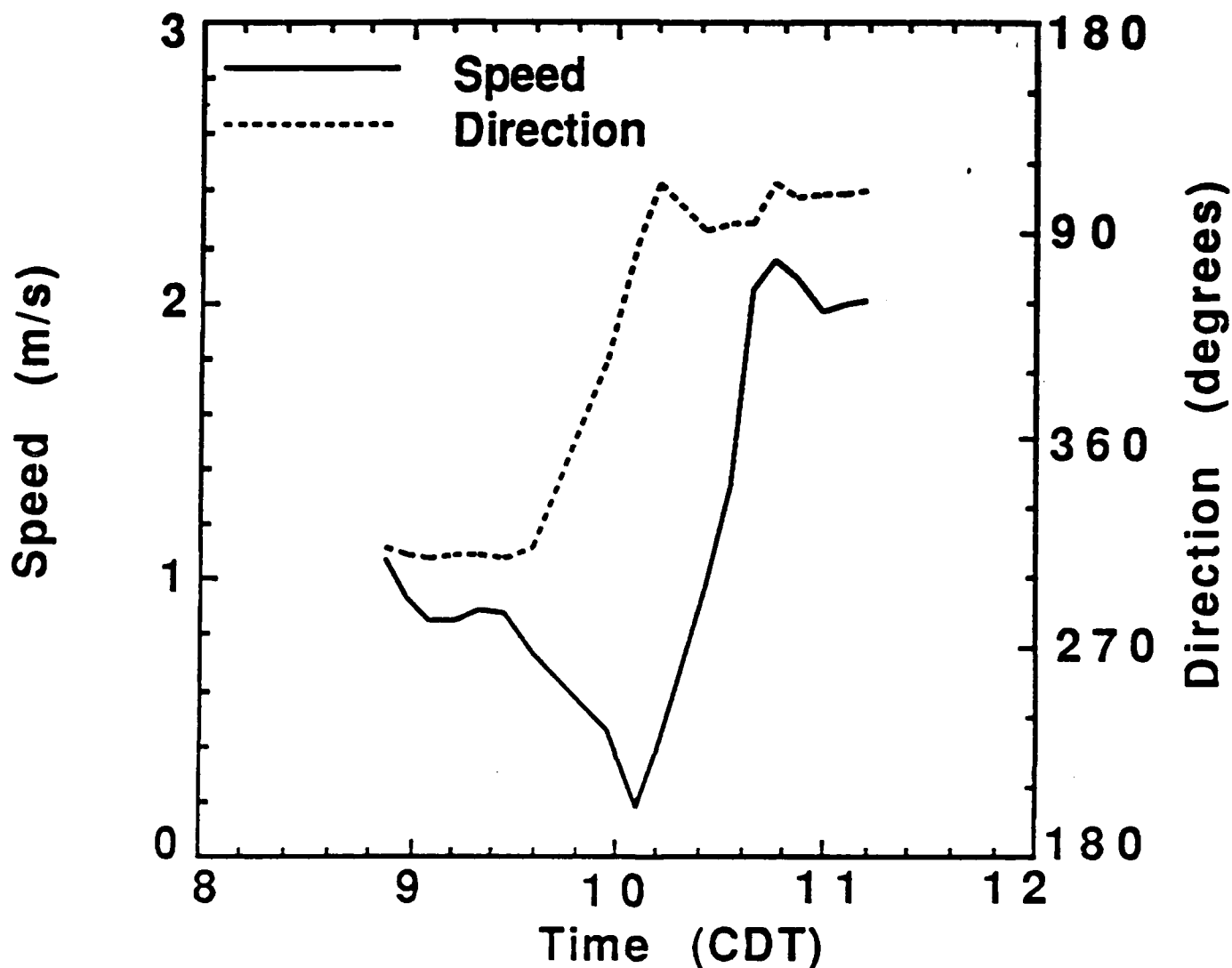


Figure 6. Lidar derived wind speed and direction averaged over the depth of the CBL during the morning of June 7, 1983. The first of the three convective regimes observed by the lidar occurred from 0830 CDT to 0936 CDT when the convective plumes were small and organized into bands. The second regime occurred between 0947 CDT to 1026 CDT, when the winds became calm, and the plumes rapidly grew in size. The third convective period occurred after 1026 CDT when the PPI scans showed elongated individual large plumes.

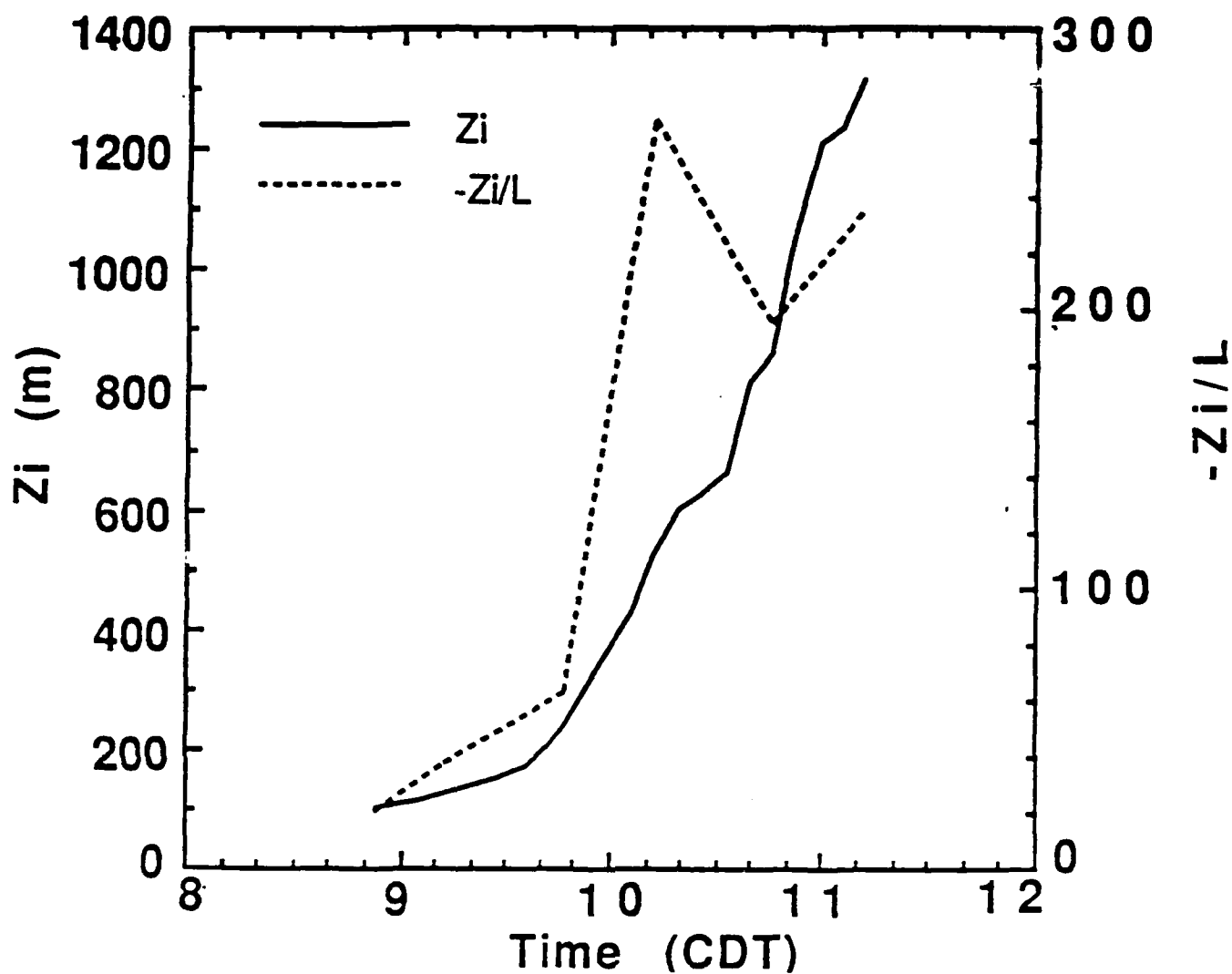


Figure 7. CBL height and instability parameter $-Z_i/L$ during the morning of June 7. Z_i was obtained from the lidar RHI data while L was determined from the ANL surface flux and kyttoon data.

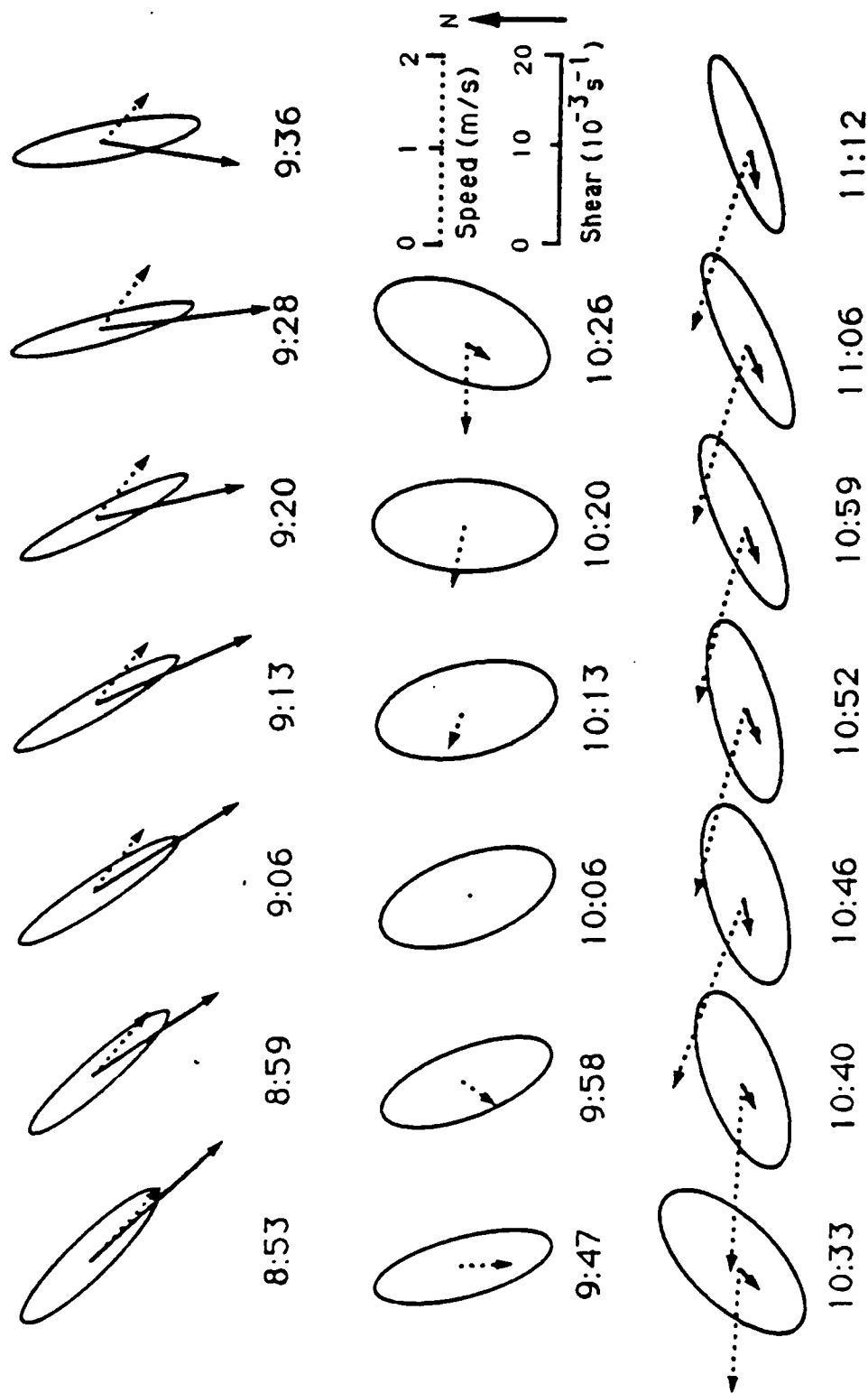


Figure 8. Shape and orientation of the aerosol structures represented by ellipses obtained from autocorrelation function (ACF) analyses of the lidar PPI scan data. These ellipses represent a specified contour level in the ACF. The mean CBL wind (dotted line) and the vertical shear of the wind over the depth of the CBL (solid line) determined from the lidar data are also shown.

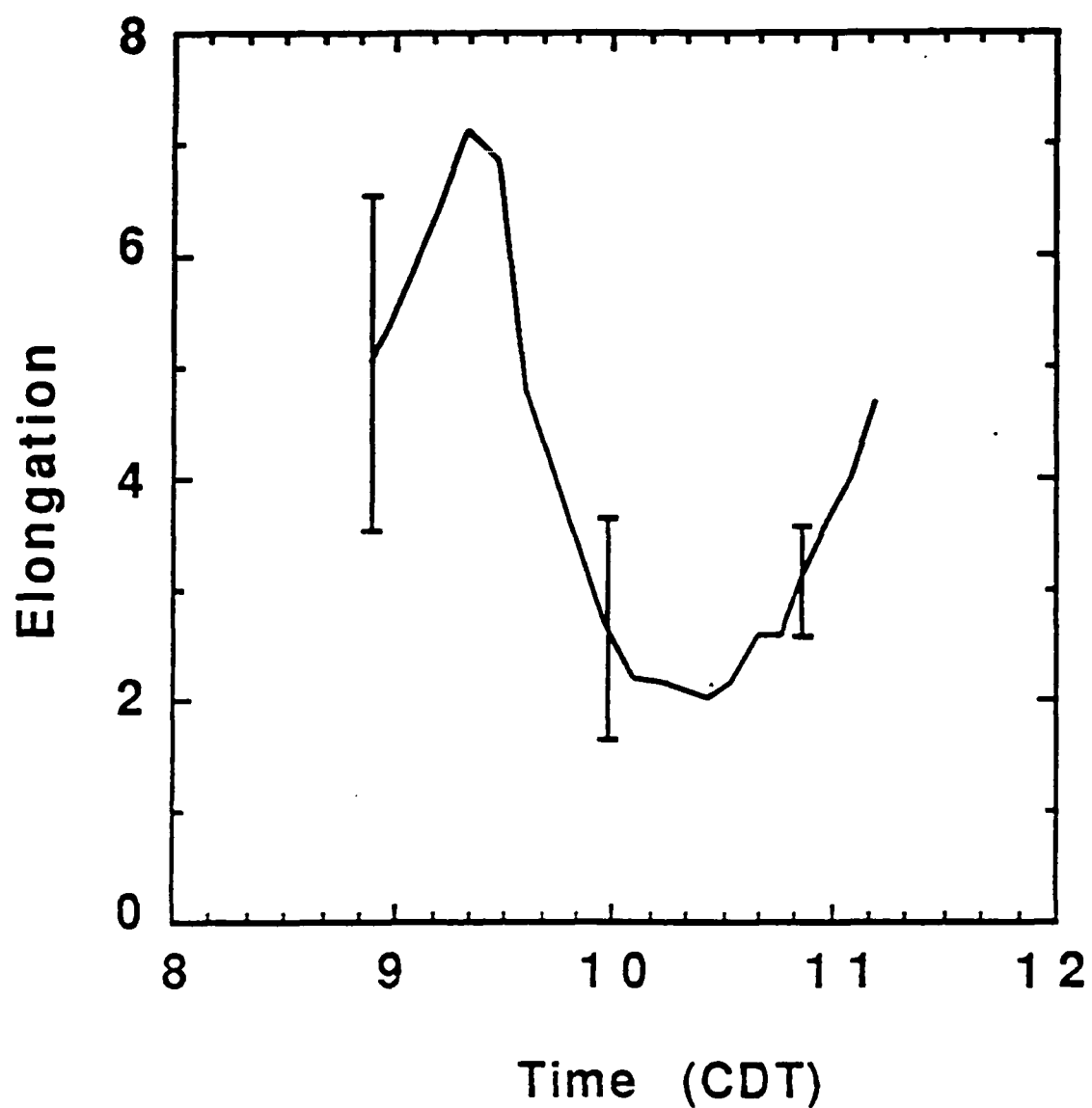


Figure 9. Elongation of the aerosol structures during the morning of June 7. The elongation is defined as the ratio of the semi-major axis to the semi-minor axis of the specified contour line in the ACF.

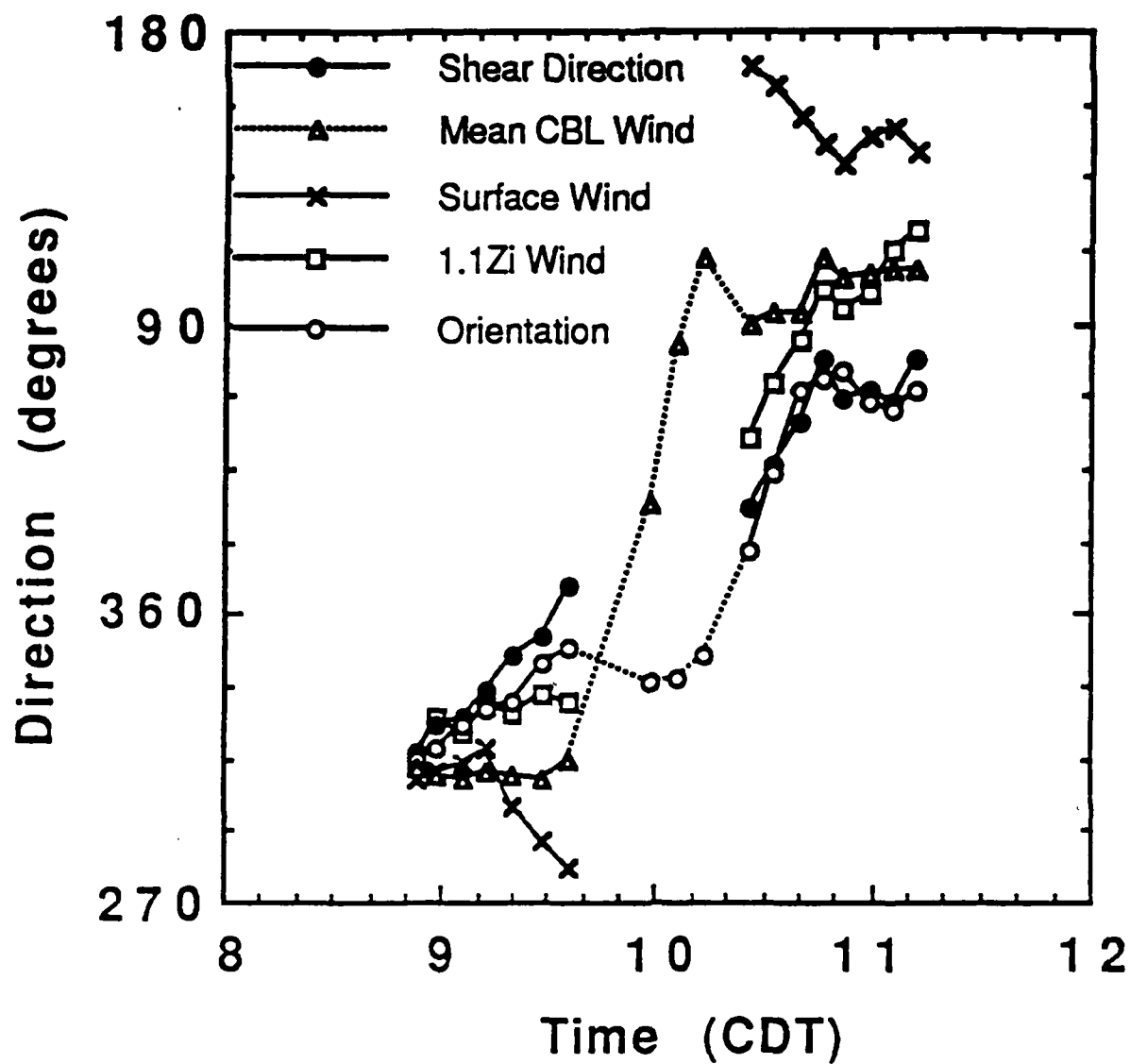


Figure 10. The directions of the vertical shear of the wind over the CBL, mean CBL wind, surface wind, and the wind at a height of $1.1 Z_i$. The orientation of the aerosol structures is also shown.

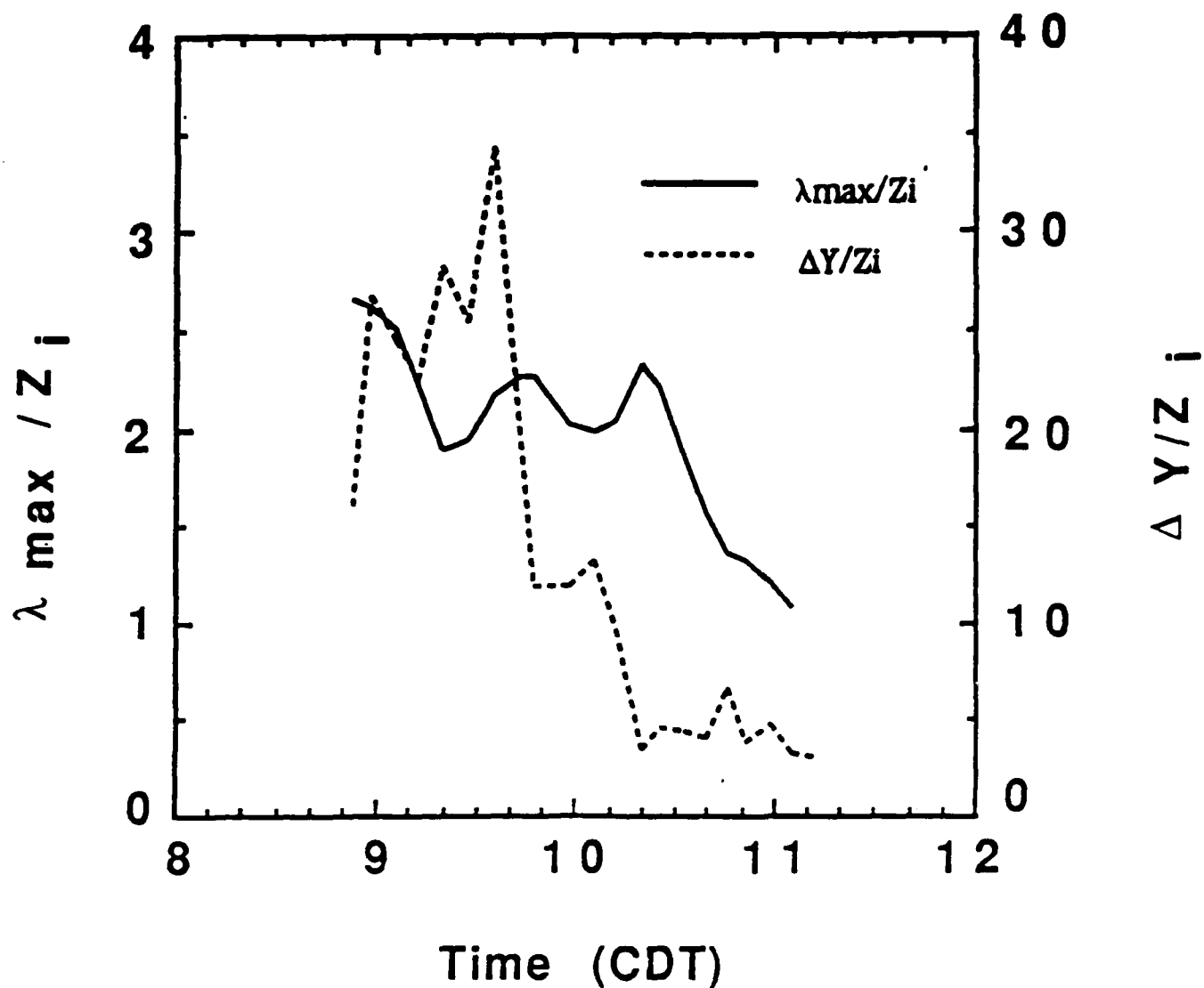


Figure 11. The aspect ratio of the aerosol structures, defined as the ratio of the dominant spectral wavelength λ_{\max} to the CBL height Z_i , for the morning of June 7. The width of the PPI scan area ΔY normalized to the CBL height Z_i is also shown. After 1020 CDT the λ_{\max}/Z_i values became unreliable because of the limitations imposed by the horizontal dimensions of the lidar PPI scan area.

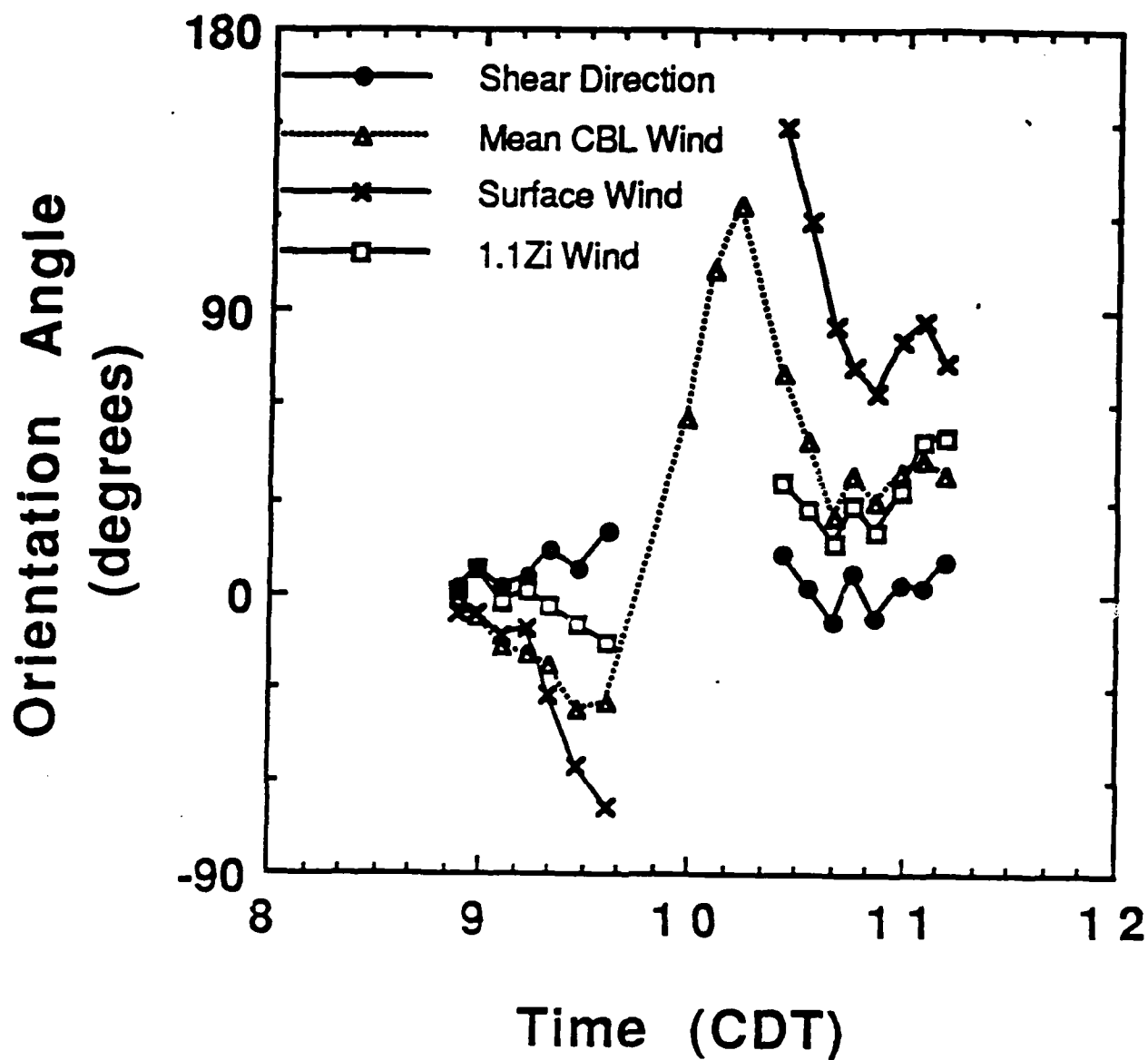


Figure 12. Orientation of the aerosol structures with respect to: the direction of the vertical shear of the wind over the CBL, the mean CBL wind, the surface wind, and the wind at an altitude of $1.1Z_i$. Orientation angles are positive for wind vectors which lie to the right (clockwise) of the axes of the aerosol structures.

Volume imaging lidar observations of the convective structure
surrounding the flight path of a flux measuring aircraft

Edwin W. Eloranta

Daniel K. Forrest

Dept. of Meteorology
University of Wisconsin
Madison, WI 53706

Abstract

The University of Wisconsin Volume Imaging Lidar has been used to image the three-dimensional structure of clear air convective plumes in the volume surrounding the flight path of the instrumented Twin Otter aircraft operated by the National Aeronautical Establishment (NAE) of Canada. Lidar images provide a context for interpretation of the aircraft measurements. The position of data points within a convective element can be determined and the temporal development of the plume can be observed to time the observation with respect to the life cycle of the plume. Plots of $q'w'$ superimposed on lidar images clearly demonstrate the well known sampling difficulties encountered when attempting to measure fluxes near the top the convective layer. When loran was used to determine average aircraft velocity, flight leg-averaged horizontal winds measured by the aircraft and area-averaged winds measured by lidar agree to within 0.2 m/s in speed and 2.5 degrees in direction.

Background

Much of our knowledge of the planetary boundary layer has been acquired from aircraft borne instrumentation. These observations have

produced a rather complete description of the mean properties of the mature mid-afternoon convective boundary layer over homogeneous surfaces. Mean profiles of state variables as well as flux profiles for heat, momentum and water vapor have been measured during many experiments and have allowed the development of a system of convective layer scaling which integrates this information into a usable form (see Stull, 1988).

While aircraft instruments are well suited for observations of established boundary layers over homogeneous terrain, difficulties arise when the layer undergoes rapid temporal changes or the surface properties change rapidly in time or space. Convective layer scaling shows that the depth of the layer is a fundamental length scale, and should be measured simultaneously with flux measurements inside the boundary layer. Interpolation errors are encountered when a single aircraft sequentially measures mixed layer depth and variables inside the layer. In order to obtain statistically reliable estimates of boundary layer variables, aircraft measurements must be averaged over many turbulent eddies; this is particularly true outside the atmospheric surface layer where eddies have scales determined by boundary layer depth and flight legs equal to or exceeding ten's of kilometers are often required (Lenschow and Stankov, 1986). It clearly becomes difficult to separate effects of spatial variability from statistical sampling variability.

Even greater difficulties are encountered when aircraft data are used in attempting to describe the typical structure of individual turbulent eddies. While precise insitu measurements can be obtained along the

flight path it is difficult to determine the aircraft position with respect to the eddy structure. Many of the efforts to elucidate eddy structure have relied on conditional sampling techniques where an indicator function constructed from one or more of the measured variables is used to control the sampling of other variables in a phase coherent manner in order to generate a composite picture of a typical eddy (Greenhut and Khalsa, Khalsa and Greenhut, 1987). The picture of the eddy which results depends critically on the choice of the indicator function (Marht and Frank, 1988). This is due to the fact that the measurement signature depends on how and when the aircraft penetrated the eddy. The measurement path may have penetrated through the center of the eddy or just grazed the edge. In addition, the timing of the observation with respect to the growth and decay of the eddy is unknown. It is very difficult to determine whether a particular observation represents an eddy which is actively extracting energy from the large scale shear/buoyancy field or the inertial remains of a dissipating eddy.

Remote sensors such as radar and lidar allow imaging of large volumes of the atmosphere in a short period of time thus allowing visualization of atmospheric eddy structure (Hardy, and Ottersten, 1969, Kunkel et al 1977). However the images produced often lack quantitative detail provided by insitu sensing. Measurements normally consist of one or two variables. For example radar or lidar reflectivity may be provided; if the system has Doppler capability radial velocities may also be included. Studies of eddy dynamics and vertical fluxes also require measurements of local velocities along with passive and active scalars

such as water vapor, temperature, carbon dioxide etc. While future remote sensors and certain current, but experimental, systems may provide some of these it is clear that insitu observations remain necessary for most investigations.

Combinations of remote and insitu measurements promise to provide considerably more information than the sum of the parts. Many examples of combined observations are available in the literature including: Konrad and Robison, 1973; Eilts and Sundra-Rajan, 1985; Crum et al, 1987.

This paper describes an experiment where the University of Wisconsin Volume Imaging Lidar is used to image the convective structure surrounding the flight path of the Canadian National Aeronautical Establishment (NAE) Twin Otter aircraft.

Instrumentation

The Volume Imaging Lidar

The Volume Imaging Lidar (VIL) is an elastic backscatter lidar designed to image the 4-dimensional structure of the atmosphere. This system couples an energetic, high pulse repetition rate laser with a sensitive receiver, and a fast computer controlled angular scanning system. High bandwidth data acquisition is sustained during extended experiments by using a 2.6 GB write-once optical disk for data storage. A Stardent GS-1000 graphics computer provides 1280x1024 pixel resolution lidar images with 16-bit pseudo color for real time control of data acquisition and data analysis. System specifications and a block diagram are provided in table 1 and Figure 1.

TABLE 1: University of Wisconsin Volume Imaging Lidar Specifications

Transmitter	
Average power	20 W
Repetition rate	30 Hz
Wavelength	106.4 nm
Receiver	
Diameter	0.5 m
Angular scanning rate	25 deg/s
APD quantum efficiency	35 %
Range resolution	7.5 m
Optical bandwidth	1 nm
Average data rate	~0.5 Gb/hr
Data Processing/Storage	Function
DEC VAX 11/750	System control and data storage
DEC LSI 11	Data transfer and formatting
CSPI Array processor	Realtime data processing
Stardent GS-1000	Realtime graphics
2.6 Gb write-once optical disk	Data storage

The high sensitivity of the VIL allows observations of inhomogeneities in natural aerosol backscatter which reveal clear air convective structure. Convective plumes carry surface aerosols aloft into cleaner air. In addition many of the aerosol particles are hygroscopic so that the particles increase in size as the relative humidity increases. Adiabatic cooling of expanding air in a rising parcel increases the relative humidity and thus increases the aerosol scattering cross section. As a result, the lidar easily delineates the boundary between mixed layer air and the free atmosphere above. Parcels of dryer, relatively clean air entrained into the boundary layer at the base of the inversion are also easily detected as they are mixed downward into the convective layer.

Aircraft Instrumentation

The Twin Otter is instrumented to provide three orthogonal components of atmospheric motion over a frequency range of 0 to 5 Hz with a Rosemount 858 5-hole probe. Aircraft motions were determined with three separate systems: 1) A three-axis Decca Doppler radar coupled with a NAE assembled package of accelerometers and rate gyros, 2) A Litton-90 Inertial Reference System, and 3) ARNAV Model R-40-AVA-100 Loran-C navigation system. Temperature was measured with a Rosemount fast-response 102DJ1CG heated probe mounted on the port side of the aircraft nose and from a second identical probe mounted on the nose boom fairing. Fast-response humidity and carbon dioxide measurements used the ESRI infrared gas analyzer developed by Agriculture Canada. These measurements were made in a high flow rate (~300 l/s) duct passing through the aircraft cabin. Slow-response carbon dioxide measurements were made with a LI-COR LI-6251 Carbon Dioxide Analyzer and slow-response water vapor measurements were obtained using an EG & G Model 137 Cambridge dew point sensor.

A more complete description of the aircraft instrumentation can be found in a reference by MacPherson 1990.

Data Acquisition

The data described in this paper was acquired on August 3, 1989 as part of the NASA FIFE experiment. The lidar was operated south of Manhattan, KS near the intersection of Rt 177 and Interstate Hwy 70 (FIFE site ID = 123).

For the observations reported in this paper the lidar was programmed to repeatedly scan an atmospheric volume consisting of the elevation

angles between 0.3 and 10 degrees and between azimuth angles of 215 and 255 degrees. The scan pattern consisted of a sequence of 80 elevation scans separated by 0.5 degree in azimuth; lidar profiles were acquired at elevation angle increments of approximately 0.25 degree. Complete volumes were scanned in 187s. Each scan included approximately 5600 lidar profiles, each consisting of 1024 data points obtained at 15 m intervals.

The Twin Otter acquired data along constant pressure altitude flight legs which began directly over the lidar and extended to approximately 20 km from the lidar. Real time lidar displays of the convective boundary layer were used to measure boundary layer depth as the aircraft approached the lidar. These measurements were used by the lidar operators to select the flight altitude of the aircraft for the data segment. The altitude was normally selected at a fixed fraction of the mixed layer depth. Flight heading was chosen along the center of the lidar scan unless lidar imagery suggested a reason for an alternate heading. The flight altitude was converted to geometric altitude above mean sea level and the altitude and heading were radioed to the aircraft in time for the pilot to stabilize altitude, heading and airspeed before beginning the data segment. This procedure increased the efficiency of data collection by positioning the aircraft at the proper altitude even in the presence of changes in boundary layer depth. During one observation period convective "streeting" was observed in the lidar images. In this case the lidar operators were able to select a flight heading perpendicular to the "streets" in order to clearly delineate the roll pattern in the aircraft data record.

Data analysis-navigation

Superposition of aircraft measurements on the lidar imagery requires careful attention to aircraft navigation and to the advection of atmospheric structure by the wind. The size of clear air convective plumes is comparable to the depth of the convective boundary layer thus the aircraft location must be known to an accuracy of 100 m or better in a typical afternoon boundary layer with a 1 km depth to maintain a 10% positioning error.

At the start of each flight leg the aircraft crew triggered an event flag in the data record at the instant they judged that the airplane was directly over the lidar. This event flag was used to check the accuracy of the aircraft Loran position by comparing the recorded positions with the known position of the lidar. Since the lowest flight was flown at an altitude of ~100 m and ground observations indicated that the pilot was successful in flying directly over the lidar, the event flags are believed to have been triggered with the aircraft within 100 m of the lidar position. On the lowest level flight the Loran showed the aircraft to be 565 m east and 796 m north of the lidar when the event marker was triggered. Because the experiment was located far from existing Loran transmitter chains, inside the "mid-continent gap", the rather large position offset is not surprising. It was assumed this displacement resulted from a systematic error in the Loran position; thus, this displacement has been subtracted from all Loran positions to form a corrected position. To gain a rough check on this correction it was compared with the positions recorded on other overflights. Corrected positions at the time of the event flags for flights at altitudes

of ~400 m and ~800 m were 158 m East, 92 m South and 187 m North, 37 m East respectively. The 400 m flight began 15 minutes before the low level flight and the 800 m flight began 14 minutes later. The position deviations at the time of the event flags on the higher flights seem consistent with an expectation for errors ~100 m considering the difficulty of piloting the airplane over the lidar and determining when the plane was directly above the lidar at the higher flight altitudes.

The lidar position was determined from a USGS topographical map using measured distances between the lidar van and buildings pictured on the map. The error in this position is expected to be less than ten meters: this error does not influence the intercomparisons because the aircraft positions were determined relative to the lidar. The alignment of the lidar's azimuth with geographical coordinates was initially performed using a magnetic compass. Lidar returns from the top of a radio tower at a range of 12.9 km were later used along with a map to provide an exact value for the conversion from lidar azimuths to geographical directions.

Knowing the aircraft position with respect to the lidar solves only a portion of the navigation problem. The wind moves the atmospheric structure during the time it takes the aircraft to fly through the lidar observed volume and during the time it takes the lidar to complete a volume scan. At ~45 m/s it required ~300s for the Twin Otter to fly from the lidar van to the end of 15 km range observed by the lidar. Similarly, the lidar required ~200s to scan a complete volume. Since the wind speed was ~10 m/s when this data was acquired the atmosphere moved ~3.3 km during the flight leg and ~2.2 km during the time of one

lidar scan. At least once during each flight leg the lidar scanned directly past the aircraft; at this point and only at this point the aircraft data and lidar image can be compared directly without compensation for wind displacements. At all other points along the aircraft flight leg the air parcel sampled by the aircraft appears at some other location in the lidar image because of the wind. Both the lidar images and the apparent flight path of the aircraft were transformed to correct for wind displacements.

Lidar image computations

Individual lidar returns were first normalized for laser energy fluctuations between laser firings and corrected for the inverse range-squared dependence contained in the lidar equation. In addition a correction was applied for optical attenuation using the approximation that the attenuation cross section was independent of position in the volume. These corrections are more fully explained in a second paper in this issue (see Schols and Eloranta, 1991). All images displayed in this paper were created with a correction for the distortion produced by the mean wind during the time required for the lidar to scan the volume. All times in the following are measured from zero at the time the aircraft flew over the lidar.

Constant-Altitude-Plan-Position-Indicator (CAPPI) images were generated as follows:

- 1) A synthetic lidar profile was generated for each of the 80 RHI scans making up a volume image. This profile reproduced the corrected lidar return which would be observed by a horizontal pointing lidar fired at the azimuth of the individual RHI scan if it were located at

the altitude of the CAPPI display. At each range data points in the horizontal pointing synthetic profile were created from the corrected data points in the original RHI scan as shown in Figure 2. The synthetic data points are computed from a linear interpolation between the data points in the nearest two lidar profiles.

2) Assuming a constant wind velocity, the individual profiles are translated to the position the air occupied at the instant when the aircraft passed over the lidar van. This process corrects for the distortion introduced by the wind in the ~200s required to complete a volume scan. Notice that since the profiles comprising the CAPPI are synthesized from many individual profiles in the original RHI scan this procedure assumes that the CAPPI profile was acquired instantaneously and neglects the 1-2s time delay between the first and last shot in the RHI.

3) Finally the missing pixels between the synthetic profiles are filled in by linear interpolation. This produces a complete CAPPI image depicting the atmospheric structure at the CAPPI altitude at the instant the aircraft passed over the lidar.

In order to superimpose the aircraft observed data points on the wind corrected CAPPI image, the position of each aircraft data point must be translated back to the position occupied by the air parcel at the instant when the aircraft passed over the lidar. The vector displacement for each point is the negative of the mean wind vector multiplied by the time between the measurement and the time the aircraft passed over the lidar. With this displacement the aircraft data can be plotted directly on the CAPPI image. This procedure corrects for the geometric

distortion introduced by the mean wind field, however, it does not account for temporal evolution in the structure. The comparison between aircraft observations and lidar imagery can be expected to degrade as the time separation between the lidar and aircraft observations of a particular air parcel increases. Superposition of aircraft data on lidar Range-Height-Indicator (RHI) images is slightly more difficult. Individual RHI images are acquired rapidly (1-2s) so that there is little wind induced distortion in an image, however because the aircraft requires ~300s to complete the flight leg a composite RHI image must be formed which images the air parcels actually penetrated by the aircraft. In the following discussion times are measured from the time at which the aircraft passed directly over the lidar van.

The composite RHI images were formed as follows:

- 1) The flight track of the aircraft over the ground was plotted and determined to be very close to a straight line.
- 2) A straight line was fitted to the ground path of the aircraft and the average speed of the aircraft along the path was calculated.
- 3) Each aircraft position on the best fit line was displaced upwind by the vector wind multiplied by the time. This new wind corrected straight line of positions indicated where the aircraft sampled air parcels were at the time the aircraft passed over the lidar.
- 4) For each RHI scan a pair of radial lines $1/4$ degree in azimuth above and below the RHI scan were constructed. These lines were also displaced upwind a vector distance equal to the vector wind multiplied by time.

5) The intersection points of these lines with the wind corrected aircraft position line were then computed. These intersection points indicated the upper and lower range limit in the RHI image where this RHI azimuth provided the best match in space and time to the air parcel sampled by the aircraft.

6) Image points from the RHI scan between these range limits were then mapped onto the composite image.

7) All RHI scans from this volume scan were checked for intersecting segments and a composite image was formed.

8) The aircraft data was now superimposed onto the composite RHI image with each data point plotted on the straight line fit to the aircraft path at the position nearest to the aircraft position at the time the data point was acquired.

Three-dimensional contour surfaces of lidar backscatter were generated as follows:

1) The position of each profile in the lidar scan was displaced upwind by a distance equal to the wind speed multiplied by the time.

2) Inside the transformed data volume a contour algorithm computed elemental polygons separating data points whose lidar backscatter exceeded a selected contour value from all other points.

3) Perspective transforms and a Gouraud shading algorithm were used to display the contour surface as a solid body image.

4) A SPOT panchromatic satellite image of the terrain under the lidar scanned volume was displayed in perspective to show the local topography.

5) Each point in the aircraft flight path was displaced upwind by a distance equal to the wind speed multiplied by the time. This corrected flight path was then displayed as a line penetrating the lidar image.

Data presentation

This paper presents data measured on August 3, 1989. The sky was partly covered with fair weather cumulus clouds: cloud coverage is shown in figure 3. At the time of the measurement the mean boundary layer depth was ~850 m with the tops of the highest cumulus observed at ~1300 m. Cloud base altitude was ~910 m. All heights are expressed as the distances above the lidar.

Wind profiles measured with the lidar, and averaged over the ~70 km squared area of the scan, were nearly independent of height between 200 m and 900 m with a speed of ~10 m/s and a direction of ~213 deg. Lidar wind profiles are presented in figures 4 and 5. This data set was chosen for analysis because the strong winds provide a stringent test of wind corrections and navigation. However, because of mechanical turbulence which mixes the aerosol structure, these rather windy conditions are not ideal for acquiring lidar images with good definition in the lower part of the boundary layer.

Figure 6 presents variables measured by the Twin Otter on a flight leg flown at an altitude of 800 m above the lidar and beginning at 18:54:53 UT (13:54:53 CDT) and ending at 19:01:33 UT. Instantaneous fluxes are also plotted in this figure. Primed quantities have been computed by subtracting the mean value over the flight leg; no other detrending or filtering has been applied. Distances along the flight path were taken from the Loran position using the Loran offset measured

on the lowest altitude flight. Aircraft ground speed calculated from the Loran position was 46.0 m/s averaged over the duration of the data record. Aircraft altitude was computed from a combination of radar altimeter and pressure altitude data. The radar altimeter has a maximum range of 779 m and thus could not be used to directly measure the altitude of this flight leg. The radio altimeter was used to measure altitudes of 436, 436 and 102 m above the lidar on three flight legs which began at 18:17, 18:26 and 18:41 UT respectively. The difference in pressure altitudes between these overpasses and the pressure altitude of the flight beginning at 18:55 was corrected for the difference in temperature of the standard atmosphere and virtual temperature measured by the aircraft to generate true altitude. These three computations produced nearly identical results of 803, 802 and 803 m above the lidar for the 18:55 leg.

Wind measurements were acquired both from aircraft instruments and from lidar observations. Lidar winds were computed by observing the drift of naturally occurring inhomogeneities in the atmospheric aerosol content using the algorithm described by Schols and Eloranta (1991). The measurements represent an average over the area of the lidar scan ($\sim 70 \text{ km}^2$) and the time interval between the scans (187s). Two lidar wind profiles were measured during the aircraft flight leg (figures 4 and 5). Aircraft winds represent the wind averaged over a 15 km data segment flown through the lidar scan. Computation of winds from the aircraft observations required knowledge of the aircraft velocity averaged over the time of the flight leg. This information was derived from the Loran positions at the ends of the data segment and duration of

the flight. A comparison of the Loran positions with the Litton INS showed a 0.485 m/s drift of the INS at 304 degrees with respect to the Loran positions over the duration of the data segment.

The wind measured by the lidar at an altitude of 800m was 10.2 m/s at 215.2 degrees; this was obtained by averaging the two lidar measurements obtained during the aircraft data run. A sequence of seven lidar wind measurements obtained between 18:24 and 19:01 UT, at an altitude of 800 m, show speeds between 10.1 m/s and 10.8 m/s with directions between 211 and 217 degrees. Aircraft wind measurements show speeds of 10.32 m/s at 216.2 degrees using the Loran and 10.35 m/s at 218.9 degrees when using the Litton-90 INS to determine aircraft velocity. A comparison of the lidar winds computed at the time of the aircraft flight leg and the aircraft winds are provided in figures 4 and 5. Notice the excellent agreement between measurements; at the airplane flight altitude the successive lidar measured speeds agree to within 0.1 m/s and direction to within 2.3 degrees. All lidar and aircraft speed measurements agree within 0.2 m/s and directions within 5 degrees.

The ability of navigation and wind corrections to properly place aircraft measurements on the lidar images of air parcels can be judged by superimposing aircraft water vapor measurements on lidar images. Water vapor is selected because relative humidity strongly influences the optical scattering cross section of naturally occurring aerosols. Many of the aerosols are composed of hygroscopic materials (Fitzgerald and Hoppel, 1984, Salemick et al 1984) which grow by the accretion of water when the relative humidity exceeds the deliquescent point of the aerosol. This flight leg was just beneath the bases of small fair

weather cumulus clouds such that the relative humidity was large in the convective plumes and relatively low in the parcels entrained from above the mixed layer. These conditions produce a sharply defined lidar image to compare with the humidity measurements.

A composite RHI lidar scan is displayed with a plot of the water vapor mixing ratio superimposed in figure 7. Wind corrections to the lidar image and the aircraft flight path were derived using the winds measured with the lidar (10.2 m/s at 215.2 degrees).

Aerosol structure in the composite RHI is highly correlated with the aircraft based water vapor measurements: regions of enhanced backscatter correspond to high values of humidity. In particular, notice the tongue of dry air at a range of ~7 km. A close correspondence between the brightness of small scale aerosol structure and the humidity trace is seen at all ranges between 5 and 9 km. The lidar scanned near the aircraft at a range of ~6.8 km providing coincident measurements at this range. Thus, temporal evolution of the structure does little to degrade the aircraft lidar comparison at the left hand side of figure 7. Figure 8 shows the RHI composite generated from the lidar volume scan obtained 187s after figure 7. In this figure the aircraft and lidar data are nearly coincident at the extreme range of the lidar image. When figure 7 is compared to figure 8, temporal evolution of the structure is clearly evident. In figure 8 the comparison between lidar and aircraft observations are best beyond 10 km. Notice that the tongue of dry air shown near 7 km in figure 7 has disappeared in figure 8. Also, the

entire region between 10 and 12.5 km has become darker in figure 8; this is consistent with the downdraft region apparent in the vertical velocity record (figure 6).

The close correspondence between aerosol structure and humidity is further illustrated in figure 9 where humidity is plotted on a wind corrected CAPPI. In the region of the picture near the aircraft the comparison is good; for example, the small plume under the aircraft path 4.5 km south of the lidar appears as a sharp peak in the humidity trace. Up to a point 6 km south of the lidar, even very small features in the image match with the details of the humidity trace. Beyond 6 km south small discrepancies appear. The dry region just beyond 6 km appears to correspond to a dark spot just north of the aircraft track and a dry region just beyond 8 km south appears to correspond to a dark spot south of the aircraft track. This is due to the time difference between the aircraft observations and the lidar image. Temporal evolution has modified the structure so as to reduce the correlation. The extent of the evolution in structure can be judged by comparing the CAPPI displayed in figure 9 with the one observed 187 seconds later (figure 10). In this image the large dry incursion of air which appears under the aircraft path 5 km south of the lidar is partly filled in by new plumes: one of these was just visible on the previous image (4.5 km south, 6.3 km west). In figure 10 the image correlates well with the humidity trace at the south-west end of the picture, but not as well in the northeast. For example, notice the dry region just beyond 8 km south of the lidar, this now corresponds nicely to a dark spot in the image.

Figure 6 illustrates the well known difficulty of measuring fluxes near the top of the mixed layer (Lenschow and Stankov, 1986). In the course of the 15 km flight only about 5 significant 'flux events' are evident; clearly the statistical reliability of an estimate made from such a low number of events is poor. An examination of the vertical velocity trace shows the largest vertical velocity events near the lidar. Clearly, fluxes computed using this record will be very sensitive to the detail of any detrending or low pass filtering of the vertical velocity trace.

The 'top hat' humidity plume measured by the aircraft at 10 km from the aircraft (figure 6) marks the plume directly under a fair weather cumulus cloud shown at ~7 km S, 10 km W in figure 3. Reference to the vertical velocity inside the 'top hat' shown in figure 6 indicates that this plume is no longer supported by rising air. A second cloud at 9 km S, 13 km W in figure 3 corresponds to the humidity 'top hat' between 12.5 and 13.5 km in figure 6. This cloud also shows little support from vertical velocity under the cloud. According to the classification of Stull (1985) both of these clouds are passive. It appears likely that if the aircraft had sampled fluxes under these clouds during their active phase much larger fluxes would have been measured. Although the cloud shown between 12.5 and 13.5 km in figure 6 exhibits little vertical velocity under the cloud a flux contribution is provided by the downdraft directly to leeward of the cloud. The downdraft is clearly evident as a small dark spot in figure 9.

Examination of the instantaneous fluxes of water, temperature and carbon dioxide show the strongest single contribution from the down

draft located at ~ 7 km from the lidar (see figure 6). This downdraft exhibits large fluctuations in the scalar quantities but only rather a small downward velocity (~ 0.25 m/s). It seems reasonable that the vertical velocity is small since the negatively buoyant plume has already penetrated significantly into the mixed layer. The next CAPPI (figure 10) shows elements of mixed layer air rising into much of the region occupied by the downdraft in first image; evidently this parcel is nearing the end of its downward motion when sampled by the aircraft. Thus even though this downdraft represents the largest single flux event observed along the flight leg, it is likely that the local fluxes in the parcel were significantly larger prior to the aircraft observation. At an earlier time, before the negative buoyancy of the plume had time to slow the downward motion we would expect stronger downdraft velocities.

Three of the prominent features in this record appear to have been sampled at times other than the time of maximum flux contribution. This indication, that strong flux contributions by an individual thermal are transient, adds to the difficulty of obtaining reliable flux measurements in the upper part of the mixed layer. Regions of strong vertical motion are sampled infrequently. Regions contributing large fluxes as a result of a combination of both large vertical velocities and large excursions in scalar quantities are therefore even more infrequent.

Conclusions

Volume Imaging Lidar observations can be used to image the atmospheric structure around the flight path of an instrumented aircraft. Because the current lidar technology requires approximately 3 minutes to map the three dimensional structure, images must be corrected

for distortion created by the wind. This paper shows that aircraft and lidar measurements can be successfully combined even in the presence of 10 m/s winds. Loran provided aircraft navigation information; however it was necessary to subtract a constant displacement vector from the Loran positions. Because a low level flight over the lidar van was available to provide this offset, aircraft data matched lidar imagery without any additional navigation corrections. In future experiments aircraft location information is expected to improve greatly with the introduction of GPS navigation. Evolution of the convective structures can be judged from successive lidar images; however the rate of turbulent change is rapid and higher lidar scan rates would be desirable.

A sample flight leg illustrates the well known difficulties of measuring fluxes in the upper part of the mixed layer. It is clear that flight legs much longer than the 15 km legs used in this experiment are required to provide stable estimates.

Winds measured by lidar and aircraft show excellent agreement. When loran was used to determine average aircraft velocity, flight leg-averaged horizontal winds measured by the aircraft and area-averaged winds measured by lidar agree to within 0.2 m/s in speed and 2.5 degrees in direction.

Acknowledgements

The authors wish to express their thanks to Dr. I. McPherson of the NRC/NAE Flight Laboratory, Dr. R. Desjardins of Agriculture Canada Land Resource Research Center and Dr. P. Schuepp of McGill University for providing the aircraft data used in this paper. Assistance in data acquisition was provided by Dr. J. Schols, and D. Sharkey. Research funding for the acquisition and analysis of the lidar data was provided by NASA grant NAG 5-902 and Army Research Office grant DAA03-86-K-0024. Funding for design and construction of the lidar has been provided by a series of grants from the Army Research Office and the Office of Naval Research.

Figure Captions

Figure 1: Schematic diagram of the Volume Imaging Lidar

Figure 2: Preparation of Constant-Altitude-Plane-Position lidar images from volume scans. Profiles corresponding to a horizontal pointing lidar at the altitude of the CAPPI are generated from each RHI scan. The data points between ranges 1 and 2 in the horizontal profile at altitude, h , are generated by linear interpolation between successive lidar profiles obtained along directions p and q . This process is repeated for all other pairs of adjacent profiles in the RHI scan to complete the horizontal profile. Horizontal profiles from all RHI scans in the volume scan are then used to compute the CAPPI image.

Figure 3: Three dimensional solid contour image of clouds and the aircraft flight path derived from the lidar scan obtained between 18:55:43 and 18:58:36 UT. This image has been corrected to represent the position of the clouds when the aircraft passed over the lidar. Wind corrections used the lidar measured wind of speed of 10.2 m/s and direction of 215.2 degrees. Since the lidar penetrates only a short distance into these clouds the image shows the cloud base and unobscured portions of the cloud facing the lidar. The terrain image was computed from a panchromatic SPOT satellite image provided by the SPOT Image Corp. (Copyright CNES 1987).

Figure 4: Lidar measured wind speed profiles for the periods 18:55:43 to 18:58:36 UT (closed squares) and 18:58:50 to 19:01:42 UT (open squares). Leg-averaged winds speeds computed from the aircraft data are also presented. Aircraft wind computations are shown using both the Litton-90 INS (open circle) and the Loran (closed circle) to determine aircraft motion.

Figure 5: Lidar measured wind direction profiles for the periods 18:55:43 to 18:58:36 UT (closed squares) and 18:58:50 to 19:01:42 UT (open squares). Leg-averaged wind speeds computed from the aircraft data are also presented. Aircraft wind computations are shown using both the Litton-90 INS (open circle) and the Loran (closed circle) to determine aircraft motion.

Figure 6: Airborne measurements showing fluctuations about the flight leg mean value for vertical wind, temperature, humidity and carbon dioxide concentration fluctuations as a function of range from the lidar. Data were acquired at a mean altitude of 803 m above the lidar in the time interval between 18:54:53 and 19:01:33 UT. No filtering or detrending has been applied to these records. Flux quantities are simple products of the displayed vertical velocity and scalar fluctuation quantities.

Figure 7: A composite RHI scan where aerosol structure in the volume scan is displaced to correct for motion caused by the mean wind between the time the aircraft sampled an air parcel and the time the lidar scanned the same parcel. The time when the volume scan was completed is displayed on the composite image. Water vapor mixing ratio variations for the flight beginning at 18:54:53 UT on August 3, 1989 are superimposed on the lidar image. The distance of the aircraft from the lidar is shown on horizontal axis. An airplane symbol marks the location where aircraft and lidar measurements are coincident.

Figure 8: The composite RHI scan computed from a lidar volume scan which began 187s after the scan used to produce figure 7. In other respects this figure is identical to figure 7.

Figure 9: Wind corrected CAPPI at the altitude of the aircraft flight measurements derived from the lidar volume scan obtained between 18:55:43 and 18:58:36 UT. Also plotted along the aircraft flight path is the variation of water vapor mixing ratio from its flight leg mean value. The image represents the position of aerosol features when the airplane passed over the lidar. Wind corrections were made using a mean wind speed of 10.2 m/s and direction of 215.2 degrees.

Figure 10: Wind corrected CAPPI derived from the lidar volume scan obtained between 18:58:50 and 19:01:42 UT. This image is derived from the volume scan data acquired 187s after figure 9: otherwise this figure is identical to figure 9.

References

- Crum, D. T., R. S. Stull, and E. W. Eloranta, Coincident lidar and aircraft observations of entrainment into thermals and mixed layers, J. of Climate and Applied Meteor., 26, p 774-788, 1987.
- Eilts, M. D., A. Sundara-Rajan, and R. J. Doviak, The structure of the convective atmospheric boundary layer as revealed by lidar and doppler radars, 31, Boundary Layer Meteor., 31, p 109-125, 1985.
- Fritzgerald, J. W. and W. A. Hoppel, "Equilibrium size of atmospheric aerosol particles as a function of relative humidity: calculations based on measured aerosol properties", Hygroscopic Aerosols, et L. H. Ruhnke, Deepak Publishing, Hampton, VA 1984.
- Greenhut, G. K., S.J.S.Khalsa, Convective elements in the marine atmospheric boundary layer. part I: conditional sampling statistics. J. Climate and App.Meteor., 26, p 813-822, 1987.
- Hardy, K. R., and H. Otterster, Radar investigations of convective patterns in the atmosphere, 26, J. Atmos. Sci, p 666-672, 1969.
- Khalsa, S. J. S., G. K. Greenhut, Convective Elements in the Marine Atmospheric Boundary Layer. Part II: Entrainment at the Capping Inversion, 26, J. Climate and App. Meteor., p 824-336, 1987.

Konrad, T.G., F.L. Robison, Development and characteristics of free convection in the free air as seen by radar and aircraft, 1973, J. of App. Meteor., p 1284-194, 1973.

Lenschow, D. H., and B. B. Stankov, Length scales in the convective boundary layer, 43, J. of Atmos. Sci., p. 1198-1209, 1986.

MacPherson, J. I., NAE Twin Otter Operations in FIFE 1989, Institute for Aerospace Research laboratory technical report LTR-FR-113, National Research Council Canada, Ottawa, Canada, 1990.

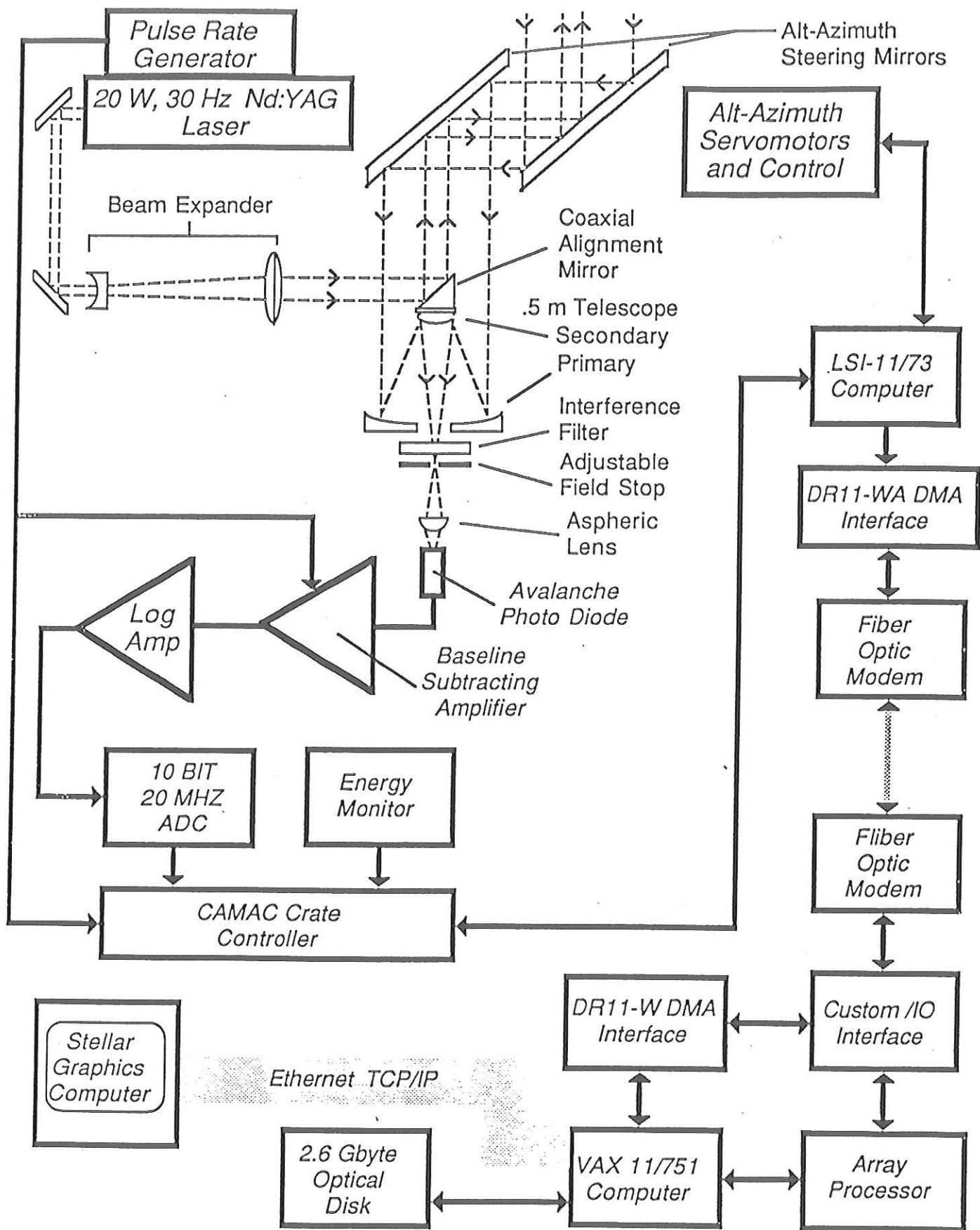
Marht, L. and H. Frank, Eigenstructure of eddy microfronts, 40A, Tellus, p 107-119, 1988.

Salemink, H.W.M. , Schotanus, P., and Bergwerff, J.B., Quantitative lidar at 532 NM for vertical extinction profiles and the effect of relative humidity, Applied Physics, p 2774-2776, 1984.

Schols, J.L., E.W.Eloranta, The calculation of area-averaged vertical profiles of the horizontal wind velocity from volume imaging lidar data. Submitted for publication in JGR.

Stull, R., B., A fair-weather cumulus cloud classification scheme for mixed-layer studies, 24, J. Climate and App. Meteor., p 49-56, 1985.

Stull, R., B., An Introduction to Boundary Layer Meteorology, Kluwer Academic Publishers, Dordrecht, The Netherlands, 1988.



Volume Imaging Lidar

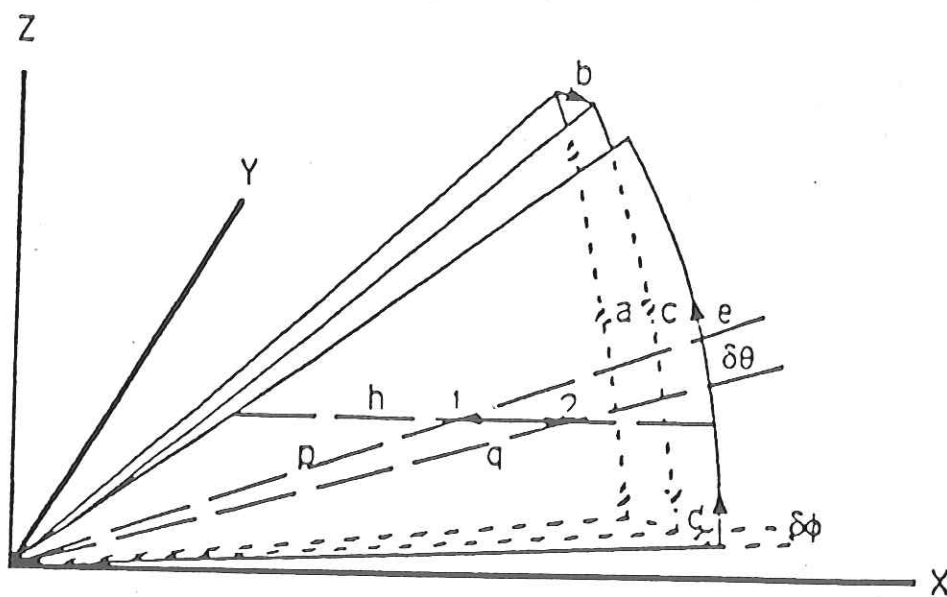
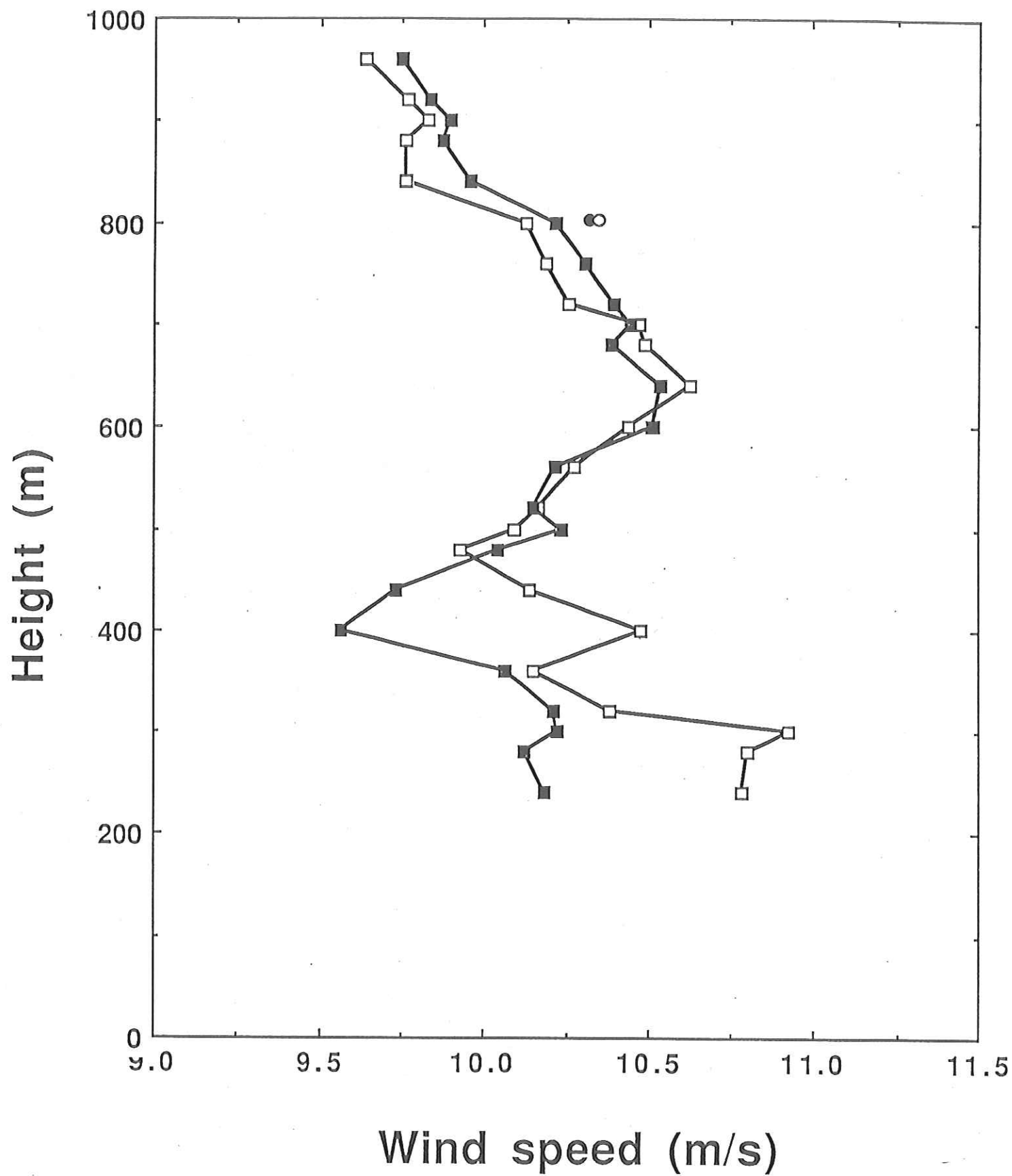


Fig. 2

University of Wisconsin
Volume Imaging Lidar
3-August-1989 13:58:37



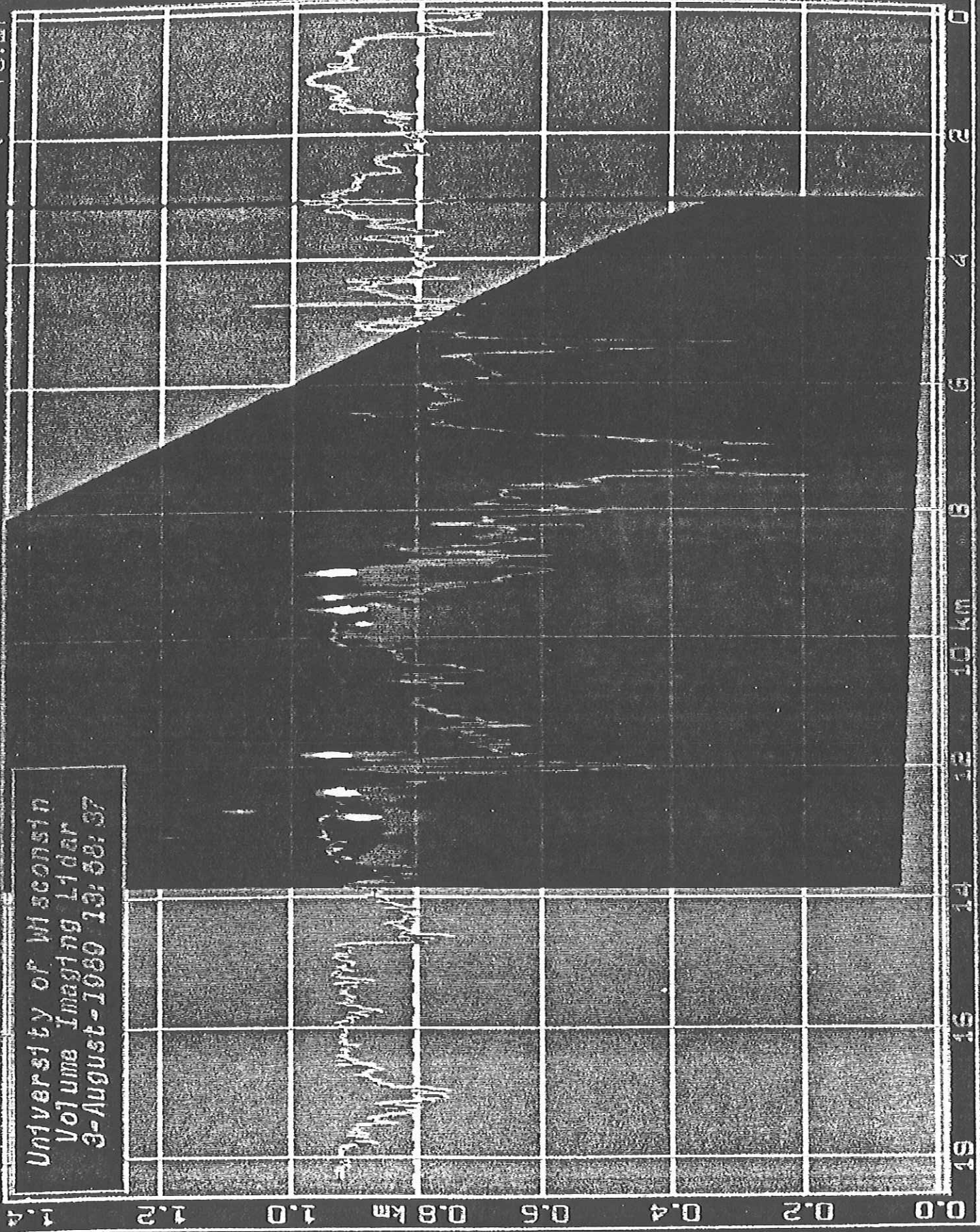


0 = 256.27

0 = 76.27

University of Wisconsin
Volume Imaging Lidar
3-August-1980 13:38:37

Altitude



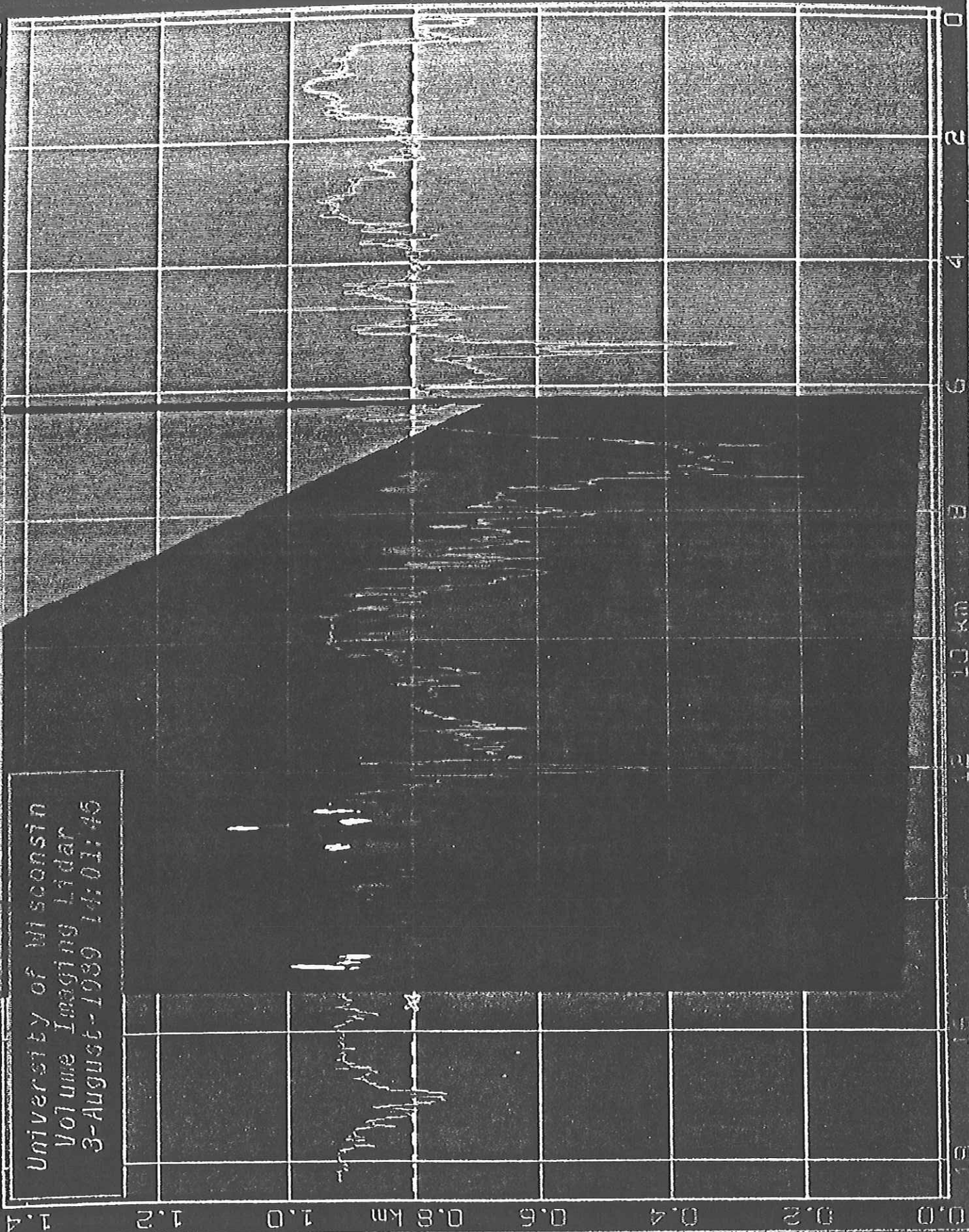
$\theta = 76.26$

RHI

$\theta = 256.26$

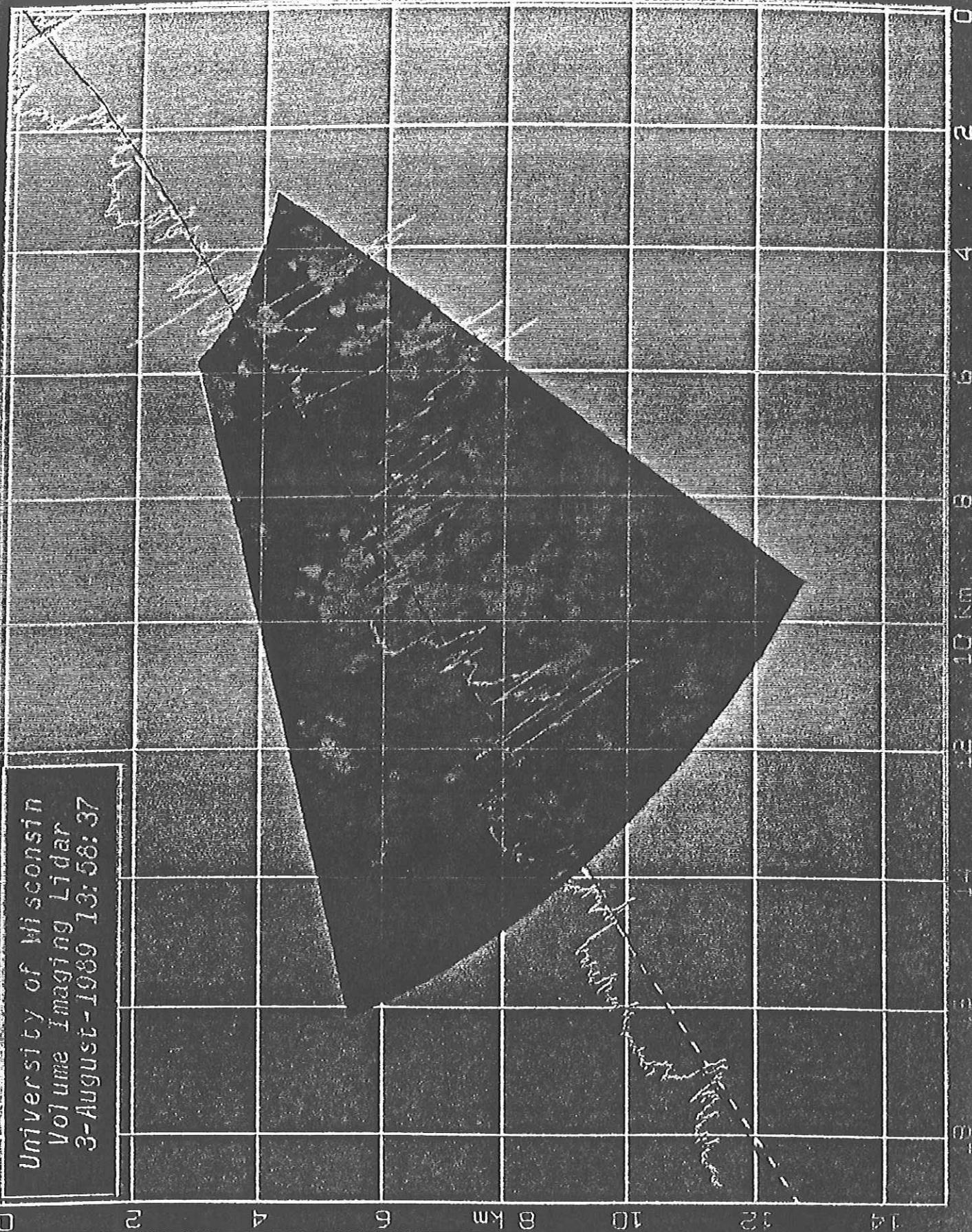
University of Wisconsin
Volume Imaging Lidar
3-August-1989 14:01:46

Altitude



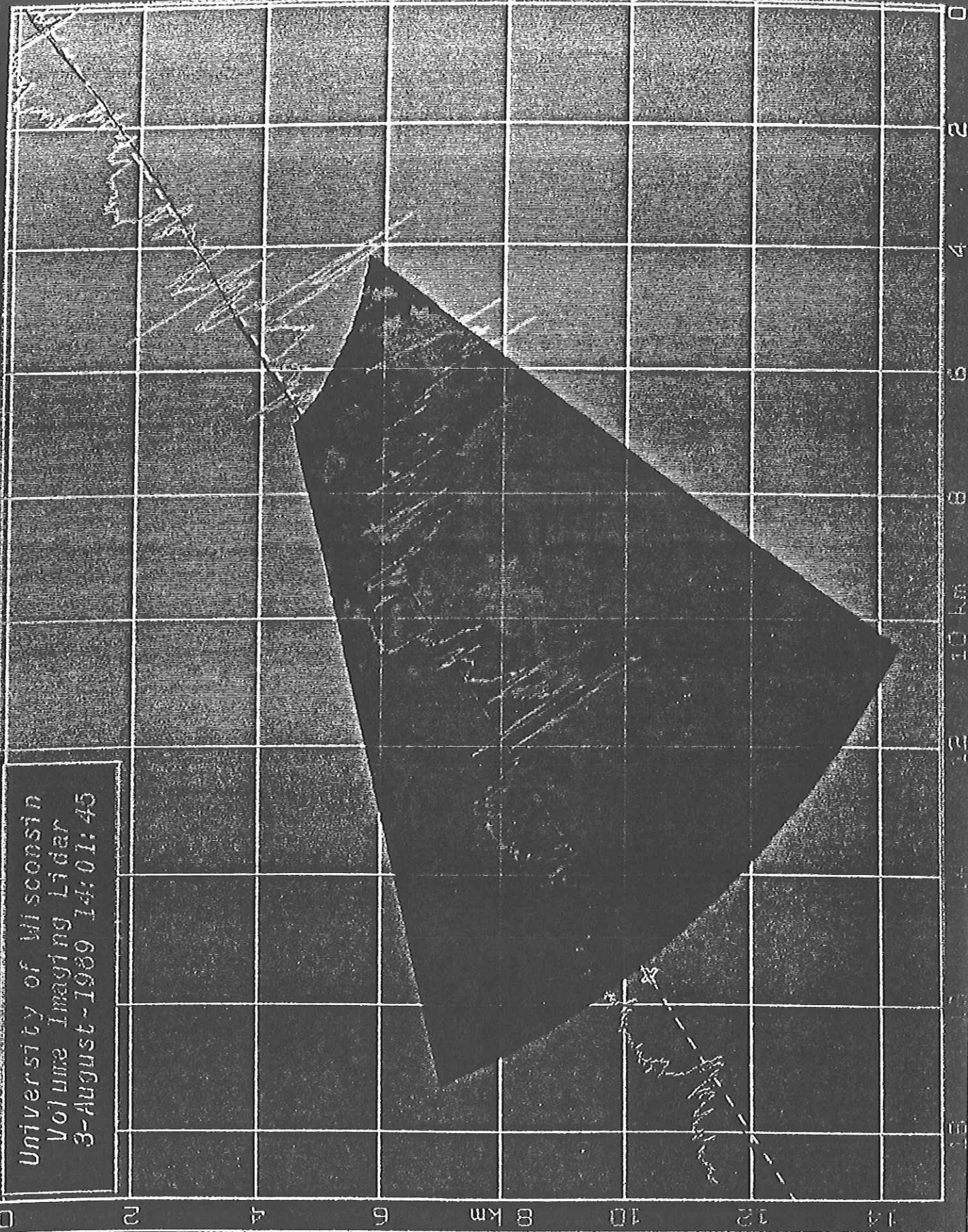
CAPPI z = 803 m

University of Wisconsin
Volume Imaging Lidar
3-August-1989 13:58:37



CAPPI z = 803 m

University of Wisconsin
Volume Imaging Lidar
3-August-1989 14:01:45



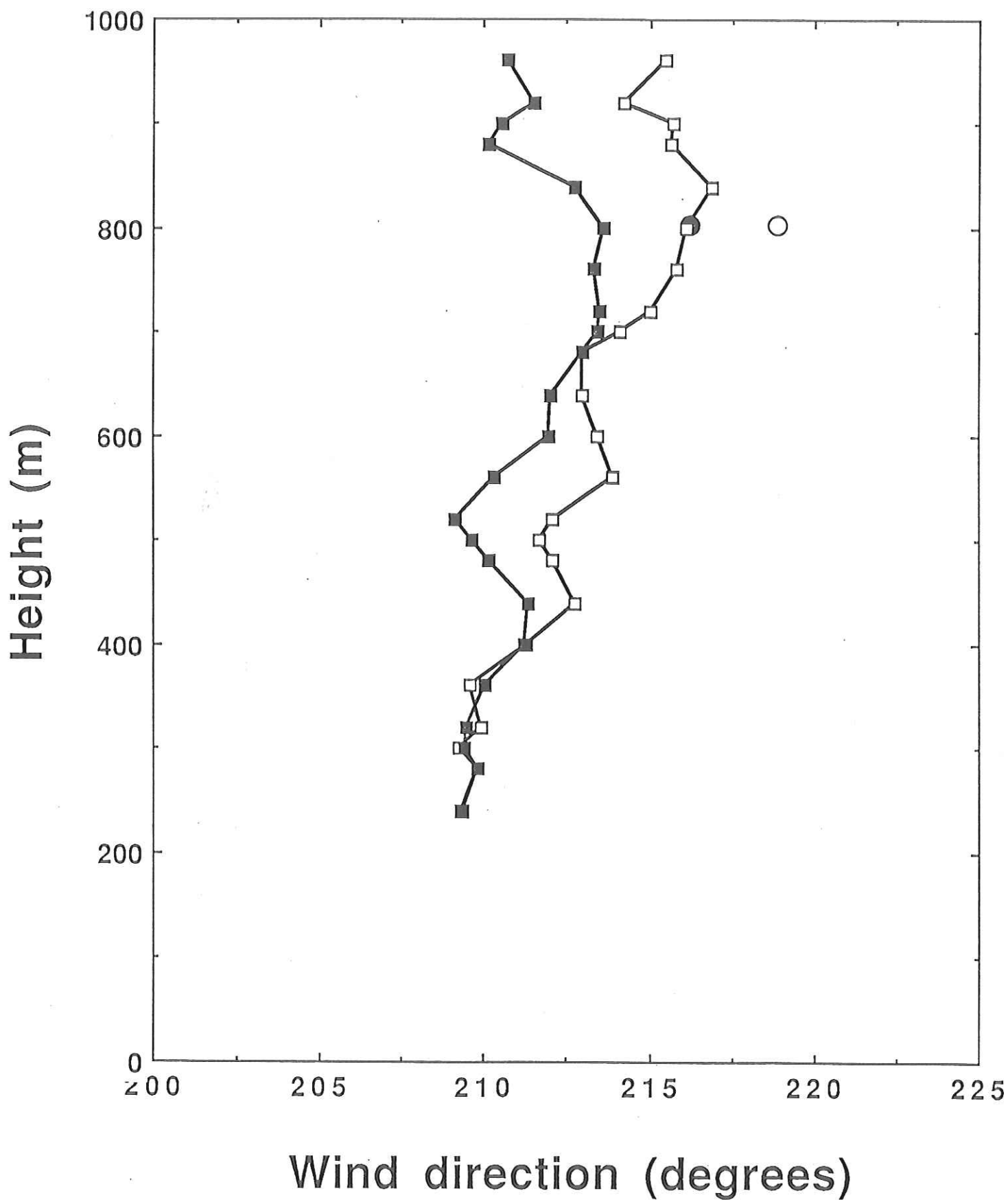


Fig 5

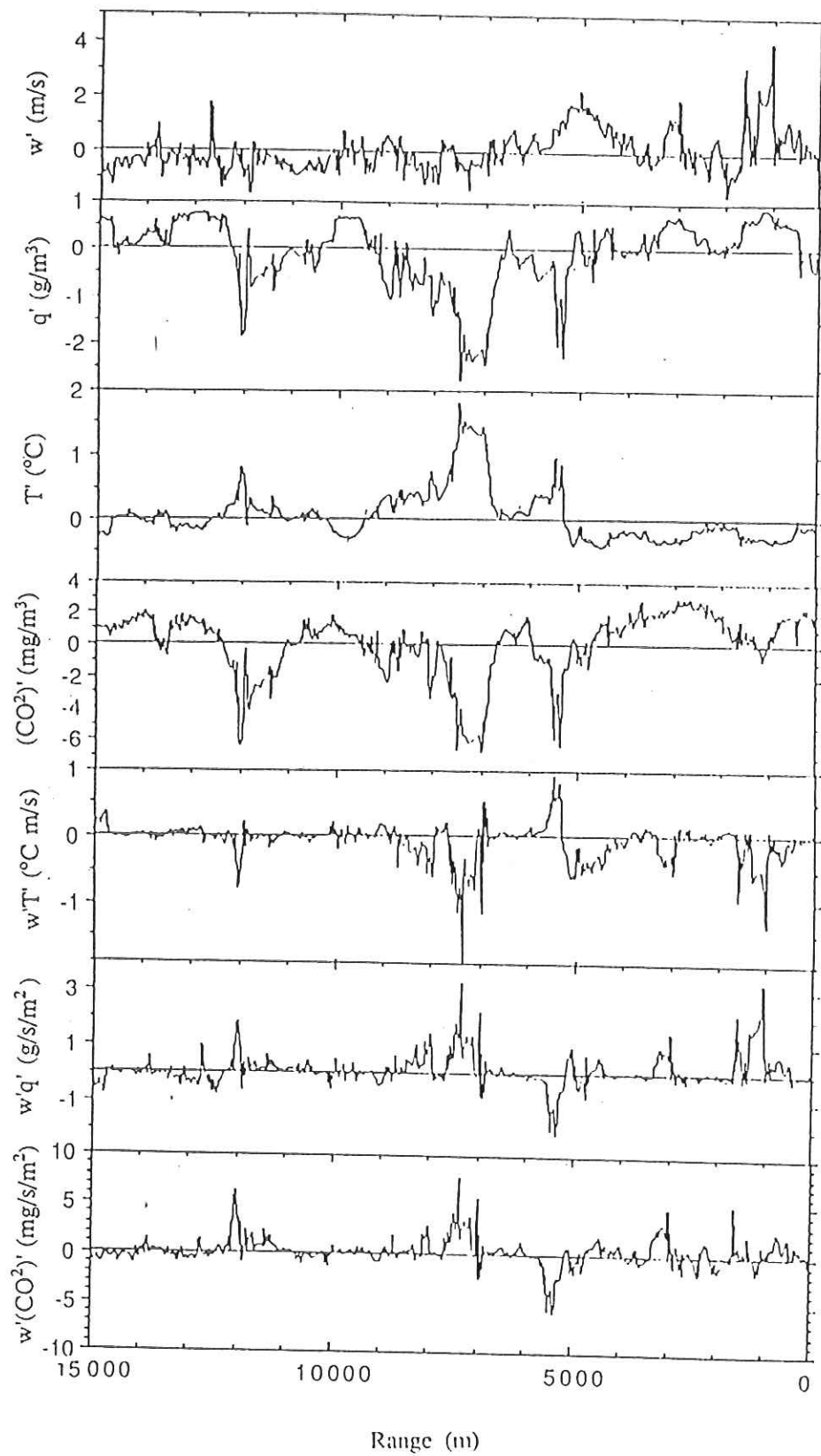


Fig 6

Appendix D

A Prognostic Relationship for Entrainment Zone Thickness

ERIC NELSON, ROLAND STULL AND EDWIN ELORANTA

Boundary Layer Research Team, Department of Meteorology, University of Wisconsin, Madison, Wisconsin

(Manuscript received 11 September 1988, in final form 29 January 1989)

ABSTRACT

The thickness of the entrainment zone at the top of the atmospheric mixed layer is analyzed using measurements made with a ground-based lidar during the BLX83 and CIRCE field programs. When the entrainment-zone depth normalized by mixed-layer depth is plotted as a function of the entrainment rate normalized by the convective velocity scale, with time as a parameter, a hysteresis curve results. Although portions of the curve can be approximated by diagnostic relationships, the complete hysteresis behavior is better described with a prognostic relationship. A simple thermodynamic model that maps the surface-layer frequency distribution of temperature into a corresponding entrainment zone distribution is shown to approximate the hysteresis evolution to first order.

1. Introduction

The entrainment zone (EZ) is the transition region between the top of the convective mixed layer (ML) and the less-turbulent free atmosphere (FA) above it (Deardorff et al. 1980). This region is usually marked by a stable lapse rate, wind shears, a humidity change to drier air aloft, and intermittent turbulence (Stull 1988). Buoyant thermals rising within the ML overshoot into the capping stable air of the EZ before sinking back into the ML, and their height of maximum rise defines the top (h_2) of the entrainment zone (see Fig. 1). Associated with this overshoot process is the entrainment of FA air downward into the ML between thermals—hence the name entrainment zone. The bottom of the EZ is less well defined, but is usually taken as the height (h_0) where 90% or 95% of the air on a horizontal average has ML rather than FA characteristics. The EZ thickness (Δh) is defined by $\Delta h = h_2 - h_0$.

The EZ thickness is important for forecasting cumulus cloud population characteristics, which in turn affects radiation budgets, climate modeling, mixed-layer dynamics and turbulence, pollution venting, and flight operations (Wilde et al. 1985). The first cumulus clouds form when the highest thermals (by definition at the top of the EZ) reach their lifting condensation level (LCL). Cloud cover increases as more thermals rise above their LCL. If the whole EZ is higher than

the LCL, then a nearly overcast stratocumulus deck can occur. Since the EZ defines the region of greatest variation of thermal population, the location and thickness of the EZ are critical for determining cumulus onset and cloud cover.

To forecast cumulus population characteristics in a climate or weather forecast model, it is desirable to be able to diagnose or forecast Δh in terms of known boundary-layer parameters and boundary conditions. Most previous parameterizations have been *diagnostic*, relating Δh to a negative power of the convective Richardson number (reviewed in section 2). We will demonstrate with field experiment data in section 3 that a *prognostic* relationship is more appropriate. In section 4 we present a theory to explain the observed behavior for free-convection cases, and suggest a simple prognostic model to forecast EZ thickness under conditions with little wind shear.

2. Diagnostic relationships for EZ thickness

a. Similarity theory

In the absence of shear-generated turbulence, mixed-layer free-convection similarity arguments suggest that the entrainment zone depth, Δh , is some function (F_1) of four other terms:

$$\Delta h = F_1(t, z_i, w_*, w_e) \quad (1a)$$

where t is time since the surface heat flux first becomes positive in the morning, z_i is average ML depth, w_* is the free-convection velocity ($w_*^3 = z_i B$), $B = (g/\theta_{s0}) \cdot w'\theta'_{s0}$ is the surface kinematic buoyancy flux,

Corresponding author address: Dr. Roland B. Stull, Boundary Layer Research Team, Department of Meteorology, University of Wisconsin, 1225 West Dayton St., Madison, WI 53706.

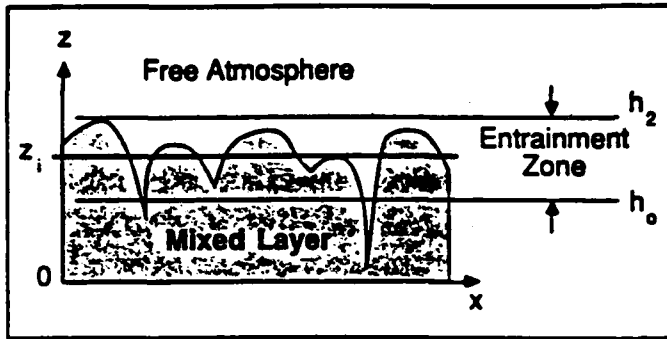


FIG. 1. Schematic of the convective boundary layer, showing the entrainment zone as the transition between the mixed layer and the free atmosphere.

g is gravitational acceleration, $\theta_{v0} [\approx \theta_v(h_0)]$ is the average virtual potential temperature within the ML, $\overline{w'\theta'_{vz}}$ is the turbulent virtual potential temperature flux at the surface, and w_e is the entrainment velocity into the top of the ML. If free convection is not assumed, then other terms such as wind shear across the EZ should be added to (1a).

Using dimensional analysis [Buckingham Pi theory is reviewed by Stull (1988)] we can rewrite (1a) in terms of dimensionless groups:

$$\frac{\Delta h}{z_i} = F_2\left(\frac{t}{t_*}, \frac{w_e}{w_*}\right) \quad (1b)$$

where $t_* = z_i/w_*$. Diagnostic relationships ignore the time dependence, leaving:

$$\frac{\Delta h}{z_i} = F_3\left(\frac{w_e}{w_*}\right). \quad (1c)$$

Similarity theory does not give information on the functional relationship between the dimensionless groups. Instead, it must be estimated empirically from observations. This functional relationship is the crux of the debate (see section 2c).

b. Definitions

Many of the published theories are based on the convective Richardson number (Ri^*) instead of w_e/w_* , where Ri^* is defined by

$$Ri^* = \frac{g}{\theta_{v0}} \frac{\Delta\theta_v z_i}{w_*^2} \quad (2)$$

and $\Delta\theta_v$ is the strength of the capping stable layer [$\Delta\theta_v = \theta_v(h_2) - \theta_v(h_0)$]. We have decided against using Ri^* because one of its key factors, $\Delta\theta_v$, is very poorly defined and difficult to determine from soundings. In certain circumstances, however, it is possible to relate the Richardson number to the entrainment velocity, as shown next.

For the special case of free convection in an idealized cloud-free ML, the entrainment velocity is proportional to the buoyancy flux at the top of the ML. It is often assumed that the buoyancy flux at z_i is proportional to the surface buoyancy flux for this case: $\overline{w'\theta'_{vz_i}} = -A\overline{w'\theta'_{vz}}$ (Ball 1960; Carson 1973; Tennekes 1973; Stull 1988), where A is an entrainment closure parameter approximately equal to 0.2 (Stull 1976a). The entrainment velocity is thus related to the surface buoyancy flux [see review by Stull (1988)] by

$$w_e = \frac{A\overline{w'\theta'_{vz}}}{\Delta\theta_v}. \quad (3)$$

Using these assumptions and a little algebraic manipulation, we find that the entrainment velocity and the convective Richardson number are related by

$$\frac{w_e}{w_*} = \frac{A}{Ri^*}. \quad (4)$$

We will use (4) to translate the various diagnostic theories based on Ri^* into the corresponding theories using w_e/w_* , in order to test those theories against our data. Some of the potential hazards associated with this translation are that A could be a function of time, latent heat release associated with clouds alters the flux and EZ thickness, and that (3) neglects the effects of mechanical turbulence induced by wind shear.

The average ML depth is defined as the height where 50% of the air on a horizontal average has ML characteristics. As shown in Fig. 1, this height is roughly in the middle of the EZ, between h_2 and h_0 . This height increases with time during the day as entrainment adds air to the ML, but can decrease in subsidence as air diverges laterally out of the mixed layer.

$$\frac{\partial z_i}{\partial t} + U \frac{\partial z_i}{\partial x} + V \frac{\partial z_i}{\partial y} = w_e + w_L \quad (5a)$$

where w_L is the large-scale mean vertical velocity (negative for subsidence). When clouds are present, other terms must be added to this mass balance. In situations of light mean wind or a horizontally homogeneous ML depth, the horizontal advection terms disappear, leaving

$$\frac{\partial z_i}{\partial t} = w_e + w_L. \quad (5b)$$

c. Literature review

Stull (1973), Zeman (1975), Zeman and Tennekes (1977), and Mahrt (1979) use a momentum balance to calculate the thermal overshoot distance, d , as a function of its initial upward velocity (assumed proportional to w_*) and the stratification of the capping inversion:

$$d \propto \frac{w_*^2}{(g/\theta_{v0})\Delta\theta_v} \quad (6a)$$

Assuming the EZ thickness is proportional to d , and using the definitions above, we find

$$\frac{\Delta h}{z_i} \propto Ri^*-1. \quad (6b)$$

Relationship (4) also tells us that $\Delta h/z_i$ is proportional to w_e/w_* ; thus, the functional form of (1c) is

$$\frac{\Delta h}{z_i} \propto \frac{w_e}{w_*} \quad (6c)$$

Indeed, one expects that in cases of strong convection with weak capping inversion, there is little resistance to the overshooting thermals, leading to both a thick EZ and a large entrainment rate.

Based on laboratory tank data, Willis and Deardorff (1974) note that Δh decreases as stability of the capping inversion increases. Some of the data from their later laboratory tank study of the EZ (Deardorff et al. 1980) supports the -1 power relationship of (6b).

Boers (1989) approaches the problem using an energy balance, relating the kinetic energy of turbulence to the potential energy of the overshooting thermals. He finds a $-1/2$ power relationship between EZ depth and Richardson number:

$$\frac{\Delta h}{z_i} \propto (Ri^*)^{-1/2} \quad (7a)$$

or

$$\frac{\Delta h}{z_i} \propto \left(\frac{w_e}{w_*}\right)^{1/2} \quad (7b)$$

The lidar observations of Boers and Eloranta (1986) and Boers (1989) support (7a), yielding a least-squares best fit power relationship of -0.52 .

Deardorff (1983) reexamined his laboratory tank data, and found that a -0.25 relationship provides a better empirical fit to some of the data:

$$\frac{\Delta h}{z_i} = \beta(Ri^* + \beta^4)^{-1/4} \quad (8a)$$

where the empirical parameter is $\beta = 1.2$. This relationship also has the appealing feature of preventing Δh from approaching infinity when Ri^* approaches zero. Focusing on just the Richardson number dependence, we find that:

$$\frac{\Delta h}{z_i} \propto (Ri^*)^{-1/4} \quad (8b)$$

In terms of entrainment velocity, the relationship above becomes

$$\frac{\Delta h}{z_i} \propto \left(\frac{w_e}{w_*}\right)^{1/4} \quad (8c)$$

Boers (1989) points out that the capping inversion is very strong for most of the laboratory tank data, while the lidar data was obtained under a weaker capping inversion. When Boers segregates the tank data by strength of the capping inversion, he finds that the strong inversion cases support a -0.24 power relationship of the Richardson number, while the weaker inversion cases support a -0.3 power relationship.

Table 1 summarizes these relationships. Each relationship is supported by data, yet each apparently disagrees with the others. We intend to show that the relationship between $\Delta h/z_i$ and w_e/w_* (or equivalently between $\Delta h/z_i$ and Ri^*) should also be a function of time (1b) that depends on initial and boundary conditions, and that the various diagnostic relationships above are not really in conflict when viewed in terms of a unified time-dependent process.

3. Lidar observations of entrainment zone depth

a. The BLX83 field program

During the summer of 1983 a boundary layer experiment (BLX83) was performed in the plains near Chichasha, Oklahoma (Stull and Eloranta 1984). As part of this experiment a ground-based pulsed ruby lidar was operated in a RHI mode to create vertical scans approximately every 3 min. Each scan has a range of about 7 km. In any one scan, the ML was visible by the enhanced scattering off of aerosols, and the FA evident as a cleaner layer of air. The contorted EZ interface was clearly visible, similar to the sketch in Fig. 1. Note that any single lidar scan, such as sketched in Fig. 1, intersects ML thermals at arbitrary locations and at arbitrary stages in their overshoot lifecycle.

Although the BLX83 field program lasted from 25 May through 18 June 1983, the lidar did not operate at all times because of bad weather and equipment failures. Table 2 summarizes the days for which there was sufficient lidar and supporting surface flux data to perform the EZ study. As can be seen from the table,

TABLE 1. A summary of publications having data and/or diagnostic relationships between normalized entrainment zone depth, Δh , convective Richardson number, Ri^* , and entrainment velocity, w_e . A power relationship is assumed: $\Delta h/z_i \propto Ri^{*-a}$ or $\Delta h/z_i \propto (w_e/w_*)^a$.

a	Investigators
1.0	Stull (1973), Zeman (1975), Deardorff et al. (1980), Zeman and Tennekes (1977), Mahrt (1979)
0.5	Boers and Eloranta (1986), Boers (1989)
0.25	Deardorff (1983)

TABLE 2. Case study days selected from the BLX83 and CIRCE experiments, and the associated weather. Abbreviations: Cu: cumulus; Ac: altocumulus, As: altostratus, Sc: stratocumulus, Cs: cirrostratus, few: less than 10% coverage, o: "fair weather" case.

Date	Weather
BLX83 (June 1983):	
•1	High pressure centered over Arkansas. Fair weather and light winds over the field site. Few Cu in late morning and early afternoon. A solid layer of As moved over the area at about 1400 local time.
•4	A weak warm front across Texas. Strong subsidence, fair weather, light winds, and drying over the field site. Few Cu formed at noon, but disappeared, leaving clear skies for the remainder of the day.
•7	High pressure centered over Oklahoma. Fair weather and light winds over the field site. First few Cu formed shortly before 1100 local time, with coverage increasing to about 20% by 1400.
12	Tight east-west pressure gradient and strong southerly winds (160° at 7 m s^{-1} , with gusts to 15 m s^{-1}), advecting in a low-level moist layer of thickness 20 kPa (200 mb). Fog and haze at 0800 local time lifted to become broken to overcast Sc for most of the day.
14	Cold front swept through Oklahoma during the night before, and high pressure moved in during the day. Overcast Ac in morning cleared out by noon. Few Cu formed over the site during the afternoon.
•15	High pressure centered over eastern Oklahoma. Fair weather and light winds. 10% Cu coverage by 1330 local time, dissipated by 1600. Thin Cs overcast in afternoon.
16	Weak high pressure between two cold fronts. Ac and Cs covered the area at 0800 local time, but breaks in the clouds allowed strong solar heating between 1000 and 1200. Mid- and upper-cloud decks increased again between 1200 and 1400, followed by rapid clearing and strong solar heating during the remainder of the day.
CIRCE (July 1979):	
17	High pressure centered over Minnesota caused variable mid- and upper-level clouds, and strong surface winds of $6\text{--}10 \text{ m s}^{-1}$ over central Illinois, with $u^* = 0.45 \text{ m s}^{-1}$ at noon. Cumulus clouds formed in the afternoon after 1300 CDT. $w^* = 1.58 \text{ m s}^{-1}$ at noon.
•21	Light winds (less than 3 m s^{-1}) and clear skies occurred over central Illinois, where pressure gradients were weak. Strong solar heating created a nearly free-convective mixed layer, with scattered cumulus forming after noon. $w^* = 1.65$ and $u^* = 0.11 \text{ m s}^{-1}$ at noon.

1, 4, 7, and 15 June provided nearly classic fair-weather conditions with minimal advection, while the other days were characterized by stronger winds or varying upper-level clouds. Shallow forced clouds (Stull 1985) were observed on many of the days (see Table 2), but did not significantly alter the EZ thickness because they did not reach their level of free convection, and because their coverage was usually less than 10%. Additional details concerning weather maps, the operations and data log, and forecaster remarks are listed by Stull (1983).

Boers and Eloranta (1986) also report EZ data from the Central Illinois Rainfall Chemistry Experiment (CIRCE), where the UW lidar was also used to determine EZ characteristics. The 21 July 1979 case had fair weather with very light winds, while the 17 July 1979 case had stronger winds. Data series from the other cases reported by Boers and Eloranta were too short to use here.

b. Analysis methods

Each lidar scan from the BLX83 experiment was computer enhanced and displayed as a video image similar to Fig. 1. They were analyzed by eye to identify the altitudes where there was (100%, 50%, 10%) FA air to define the heights (h_2 , z_i , and h_0). We used the definition of 10% FA air to define the lower limit of the EZ rather than 5% as suggested by Deardorff et al. (1980) and Deardorff (1983), because of the difficulty

in segregating the thin wisps of entrained air from the surrounding aerosol-laden ML air. As those thin FA wisps penetrated down into the ML, small-scale mixing added aerosols to the entrained air and reduced the contrast between the two fluids, making it difficult to precisely identify the 5% level. The resulting time series of raw EZ heights was of high temporal resolution, often with about 150 data points per curve per 8 h period. Boers and Eloranta (1986) used a similar analysis method for the CIRCE data.

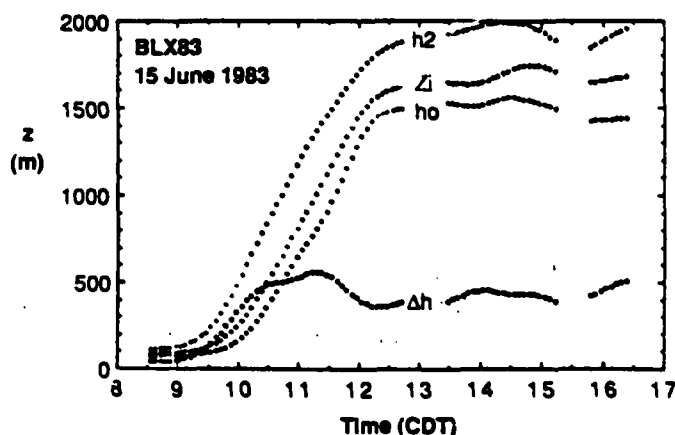


FIG. 2. Smoothed evolution of the mixed layer depth, z_i , and the top and bottom of the entrainment zone, h_2 and h_0 respectively, for 15 June 1983 at the BLX83 field site in Oklahoma. The bottom curve is entrainment zone thickness, Δh .

The resulting time series for BLX83 were smoothed to produce the EZ and ML curves such as shown in Fig. 2. The raw EZ time series have a scatter of ± 10 m about the smooth curves in the early morning, increasing to approximately ± 100 m by midafternoon. The scatter is associated mostly with sampling error, because any one lidar scan views only a small portion of the EZ and intersects only one to three thermals during the afternoon. The raw data for h_0 , z_i , and h_2 was filtered using a Gaussian weighting function, with standard deviation of the weights at ± 20 min, and a cutoff at ± 1 h. One-sided filtering was used at the ends of the time series. A new time series with data evenly spaced at 5 min intervals (as in Fig. 2) was then calculated by linear interpolation from the smoothed values. Missing data over periods of 10 min or greater are left blank. The filtered curves provide a more representative spatial and time average that hopefully captures most of the statistical distribution of the local ML top, with net errors of approximately ± 2 m in the morning and ± 20 m in midafternoon. Curves for the other case-study days are plotted in appendix A. For the CIRCE data, a five point smoother was used on the data reported in the appendices of Boers and Eloranta (1986). Although the smoothing operations reduce the sampling error, they could potentially induce time lags in the smoothed signals compared to the original raw curves. This effect was carefully examined, and found not to cause significant changes to the hysteresis curves to be presented here.

Figure 2 shows the typical three-stage ML evolution (Stull 1988). In early morning the shallow ML rises slowly as the nocturnal stable layer is being "burned off." By late morning [1000–1200 CDT, where CDT (Central Daylight Time) = UTC – 5 h] the ML rises rapidly through the previous day's weakly stable residual layer. Finally, the ML top hits the previous day's capping inversion, resulting in a quasi-steady deep convective boundary layer.

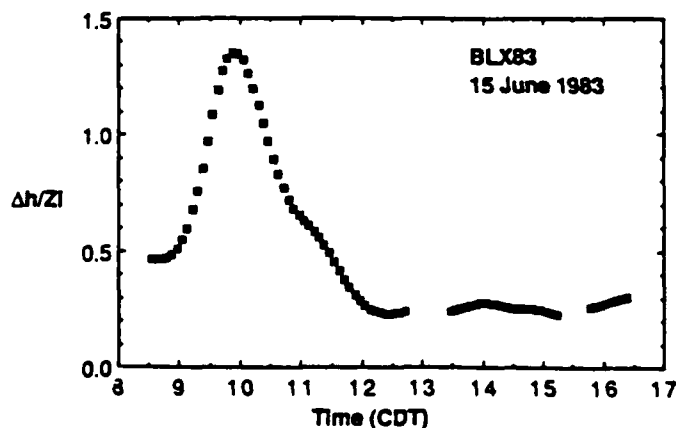


FIG. 3. Entrainment zone depth, Δh , normalized by mixed-layer depth, z_i .

The normalized EZ depth evolution ($\Delta h/z_i$ vs t) is plotted in Fig. 3 for the 15 June 83 BLX83 case. A well-defined peak occurs at the 1000 CDT initiation of the rapid-rise phase. Lidar scans show that this large EZ thickness occurs because some of the thermals are breaking through the nearly eroded nocturnal stable layer and rising up to the capping inversion, while other weaker thermals are still trapped near the surface by the nocturnal inversion. Similar peaks occur for the other fair-weather cases, as shown in appendix B.

To test relationships (6) through (8), we need to calculate w_e and w_* from the data. The evolution of w_* was found using eddy-correlation heat flux data from both the NCAR Queen Air flight legs near the surface (mean altitude above ground was 50–100 m, which was usually well within the surface layer), and from a 10 m surface micromet tower operated by Argonne National Laboratory (ANL) during BLX83. Both the ANL site and the aircraft track were in the same plane as the lidar scan. The aircraft observations were used to provide the magnitude of the leg-averaged flux, while the ANL data provided the time continuity to extend the heat flux curves before and after the flight times. In addition, portable automated mesonet surface station (PAM) temperature evolution was used to help define the morning and evening times of zero heat flux. A smooth sine-wave curve was then fit to the resulting data, with drops below the smooth curve whenever clouds caused shading of the ground. The buoyancy flux, B , was calculated from the sensible heat fluxes, latent heat flux was neglected for simplicity, and $\partial z_i/\partial t$ was found from the lidar data (as in Fig. 2). The resulting evolution of w_* is plotted in appendix C for all of the BLX83 cases.

To find w_e for the BLX83 dataset, we neglected horizontal advection and used (5b). The local rise rate of the ML measured by lidar (Fig. 2) gives us $\partial z_i/\partial t$. Mean vertical motion (w_L) at the top of the ML was estimated from $w_L = -(\text{div})z_i$, where div is mean ML divergence. In an independent study (Vachalek 1987, 1988), divergence in the BLX83 ML was estimated from Doppler radar data, the network of PAM stations, a rawinsonde triangle, and lidar observations of subsiding elevated haze layers. As is always the case for divergence and subsidence data, the scatter and errors in the data are quite large [in the area of 100%, see Vachalek (1987) for details]. A summary of the divergence for the various cases is plotted in appendix D. We used these data values as our best guess, with the full understanding of the magnitude of the errors. Figure 4 shows the local rise rate of the ML, the mean vertical velocity at the ML top, and the calculated entrainment velocity using (5b). In appendix E are plots of the corresponding curves for the other cases. Boers and Eloranta (1986) provide similar data for the CIRCE cases.

The neglect of advection is an adequate assumption for the cases of high pressure and light winds, but it is

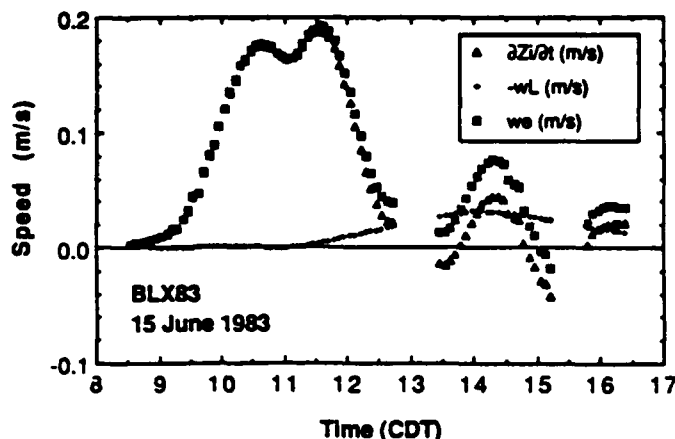


FIG. 4. Entrainment rate (w_e) as calculated from observations of local mixed-layer top rise rate ($\partial z_i/\partial t$) and subsidence velocity ($-w_L$).

likely to be a very poor assumption for the other cases. Unfortunately, we have no data on the horizontal variability of z_i , and must recognize that the potential errors of this neglect could easily be in the area of 100%.

c. Hysteresis entrainment zone behavior

Comparing Figs. 3 and 4, the EZ depth peaks between 0900 and 1100 CDT, while the entrainment velocity peaks between 1000 and 1200 CDT. There is clearly a time difference between these two peaks. Such

a time difference is also evident in the raw (unfiltered) data as well. Figure 5, a plot of normalized EZ depth vs normalized entrainment rate, shows the highly time-dependent behavior. This figure clarifies that many power law diagnostic relationships could be suggested as a tangent to the curve. Examples of the linear, $1/2$, and $1/4$ power relationships from section 2 are plotted in Fig. 5.

Figure 5 establishes clearly that a diagnostic relationship between normalized EZ depth and entrainment velocity is not appropriate. For any given value of w_e/w_* , there are multiple possibilities for EZ thickness depending on the state of the time evolution. The power-relationship curves plotted in Fig. 5 approximate small portions of the whole curve. We suggest that these curves were proposed in the literature based on data from small segments of the total time evolution. As such they are valid for the special conditions upon which they were derived, but not to describe the whole time evolution.

Hysteresis-like evolution of EZ depth similar to that in Fig. 5 was observed for the other three BLX83 fair-weather cases and for the 21 July 79 CIRCE case as well (see Fig. 6). Starting in the mornings with weak convection, near zero entrainment, and a strong capping nocturnal inversion (at approximately 0830 CDT), the entrainment zone thickness is on the order of 0.5 to 0.8 times the average ML depth. A bit later

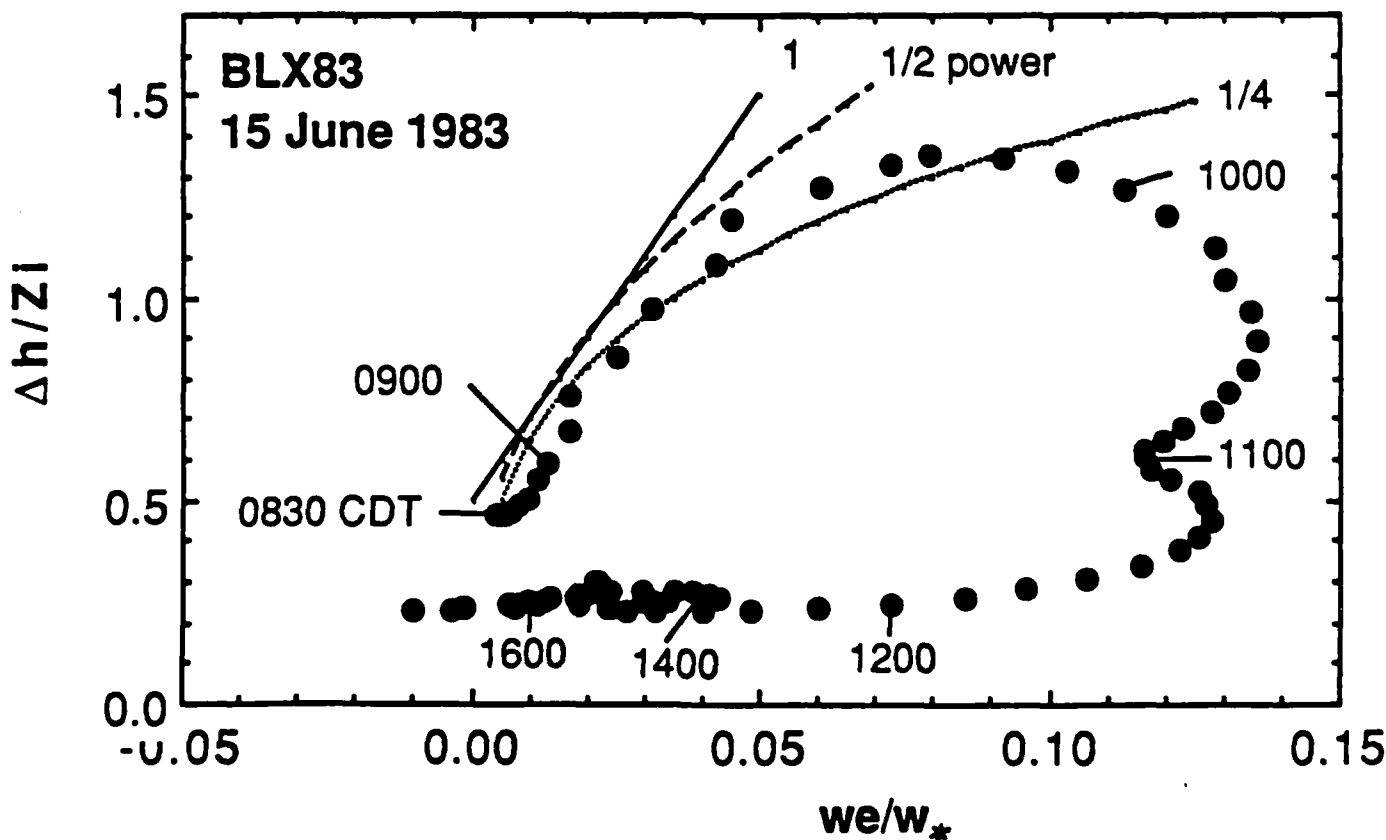


FIG. 5. Evolution of normalized entrainment zone depth (Δh) with entrainment velocity (w_e) for the same case as the previous figures. Power law relationships (offset in the vertical for easier comparison with the data points) are also sketched.

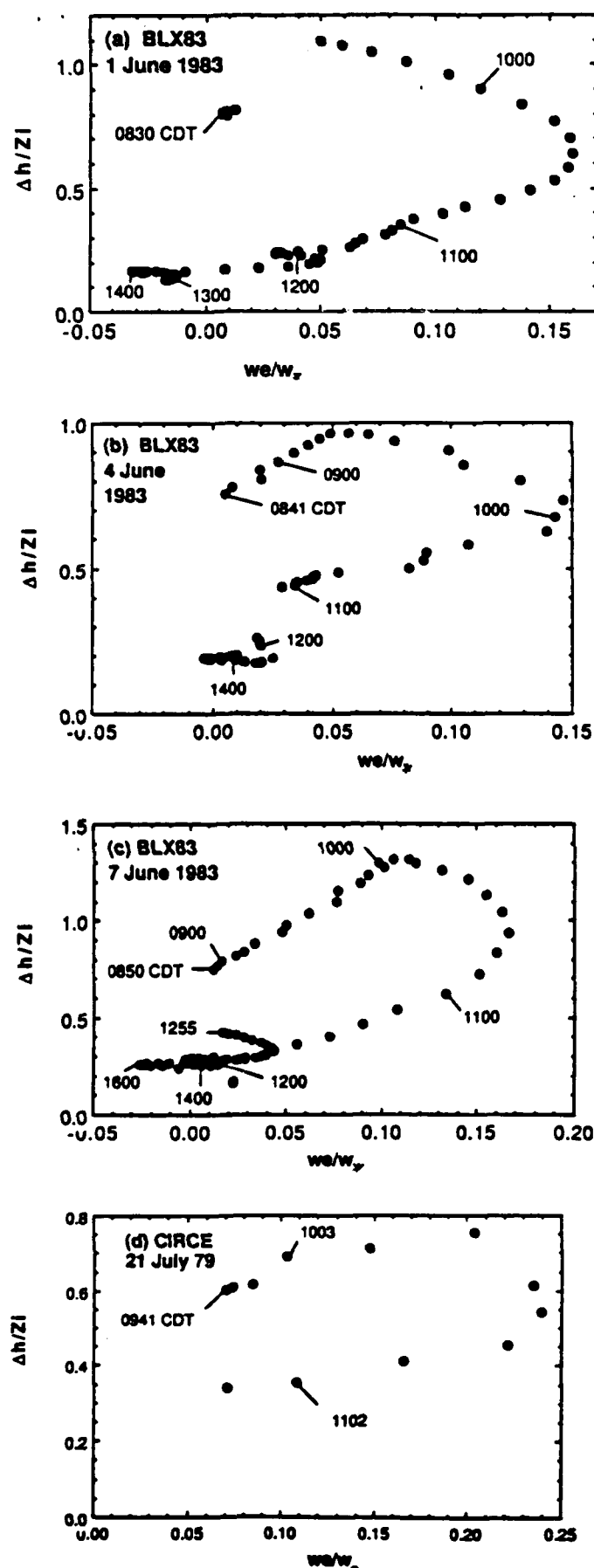


FIG. 6. Evolution of the entrainment zone thickness for the other fair-weather cases, similar to Fig. 5: BLX83: (a) 1 June; (b) 4 June; (c) 7 June 1983; and CIRCE: (d) 21 July 1979.

in the morning (between about 0900 and 1000 CDT) as the entrainment rate increases and the capping nocturnal inversion weakens, the EZ depth increases to its maximum thickness of about 0.8 to 1.5 times the average ML depth. By mid- to late morning (1000 to 1100 CDT), the EZ thickness begins to decrease. During the period of rapid ML rise through the residual layer, the EZ thickness is about 60%–70% of its earlier maximum thickness.

Between about 1000 and 1200 CDT for these BLX83 cases, both the EZ thickness and the entrainment rate smoothly decrease, as the ML reaches the strong capping inversion remaining from the previous day's ML. Then, during much of the remainder of the afternoon when there is virtually no net entrainment (during 1200 through 1600 CDT), the EZ thickness is remarkably constant, equal to about 15%–25% of the average ML depth (which is also nearly constant during this period).

An obvious problem with Fig. 6 are the (unrealistic) negative entrainment velocities in the late afternoon. In many of these fair-weather cases, the top of the ML was observed to lower, probably because subsidence was greater than the entrainment rate, perhaps also because of advection. Our calculations of subsidence velocity based on ML divergence are difficult to make because of the small signal-to-noise ratio. As a result, we underestimate the subsidence at the ML top for this case, resulting in the calculation of negative entrainment rates when (5b) is used. In conclusion, we suggest that if subsidence had been properly accounted for, then the bottom loop of the curves in Figs. 5 and 6 would be shifted to the right. We can estimate the apparent subsidence at the end of each time series by adding the w_L velocities from Figs. 5 and 6 (based on the amount each curve is shifted to the right to prevent negative w_e) to those given in appendix E. For the 1, 4, 7 and 15 June cases, the net subsidence at the ML top is estimated to be $-w_L = 0.007, 0.038, 0.066$, and 0.033 m s^{-1} , respectively.

For the variable-weather cases with stronger winds, a time evolution of the EZ thickness is again observed, but not with the simple hysteresis structure noted above. Figure 7 shows that these time series are quite complex, and are not amenable to a simple description. No subsidence data was available for Figs. 7a and 7b; hence, $[\partial z_i/\partial t]/w_*$ is plotted instead of w_e/w_* on the horizontal axis. One statement we can make, however, is that a diagnostic power-relationship is also not appropriate for these cases.

4. A simple thermodynamic theory for entrainment-zone evolution

While the previously published theories for EZ thickness have approached the problem using momentum or energy balances, a thermodynamic ap-

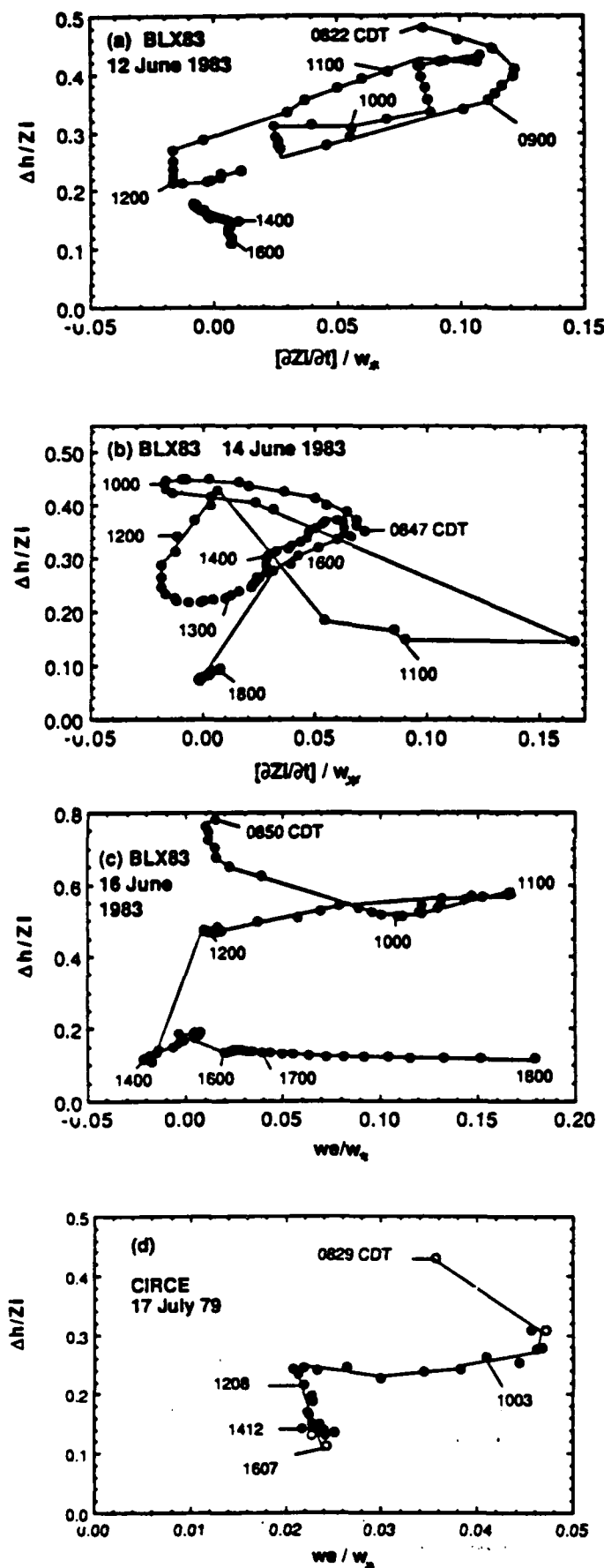


FIG. 7. Evolution of the entrainment zone for variable-weather cases: BLX83: (a) 12 June; (b) 14 June; (c) 16 June 1983; and CIRCE: (d) 17 July 1979. The open data points for CIRCE (d) are unsmoothed values at the ends of the time series.

proach has not been tried. We will show how a thermodynamic theory, while not capturing all of the complexities, can describe the bulk behavior of EZ thickness including a hysteresis cycle.

A similar evolution of theories occurred in the previous 15 years for average ML depth, where a variety of turbulence kinetic energy (TKE) budget approaches were tested, but were found (Stull 1976b; Boers et al. 1984) to ultimately be controlled to first order by the thermodynamics. For example, if turbulence is vigorous and entrainment is temporarily rapid, the ML will rise and the temperature jump across the capping inversion will increase. This increase of inversion strength reduces the entrainment rate, and the entrainment remains small until there is sufficient warming of the ML to reduce the inversion strength. A balance is eventually reached where the ML top rise rate is limited primarily by the heating rate of the ML, and the characteristics of the morning sounding into which the ML is growing. This thermodynamic approach is sometimes called "encroachment" method (Carson and Smith 1974; Stull 1988).

a. Concept

The following first-order thermodynamic approximation is suggested for EZ thickness. First, it is known that there is a distribution of temperatures of air within the heated surface layer (Caughey 1982; Mahrt and Paumier 1984; Deardorff and Willis 1985; Stull 1988). Such distributions could be caused by natural random interthermal variability, and by differential heating rates over nonhomogeneous surfaces. Using a very simplistic parcel approach and assuming a typical fair-weather early-morning environmental sounding, one would expect the warmer rising parcels to reach their level of neutral buoyancy at a higher altitude than relatively cooler ones. Neglecting overshoot (consistent with an encroachment method), we see that the distribution of surface-layer temperatures at any time of day can be remapped (using the morning environmental sounding) into a corresponding distribution of local ML depths. This distribution of ML depths defines the EZ, as is sketched in Fig. 8.

Although it is clear that intromission (lateral entrainment) into thermals causes dilution of the thermal edges, measurements during the BLX83 experiment (Crum et al. 1987; Crum and Stull 1987) show that a large central core of the thermal remains relatively undiluted. In these cores the potential temperature and humidity near the top of the thermal are nearly unchanged from their surface values. Thus, variations in surface thermal strength cause associated variations near the top of the ML. Although we will assume for simplicity that all rising parcels are undiluted, one should recognize the limitations of this assumption (Turner 1973; Hunt et al. 1988).

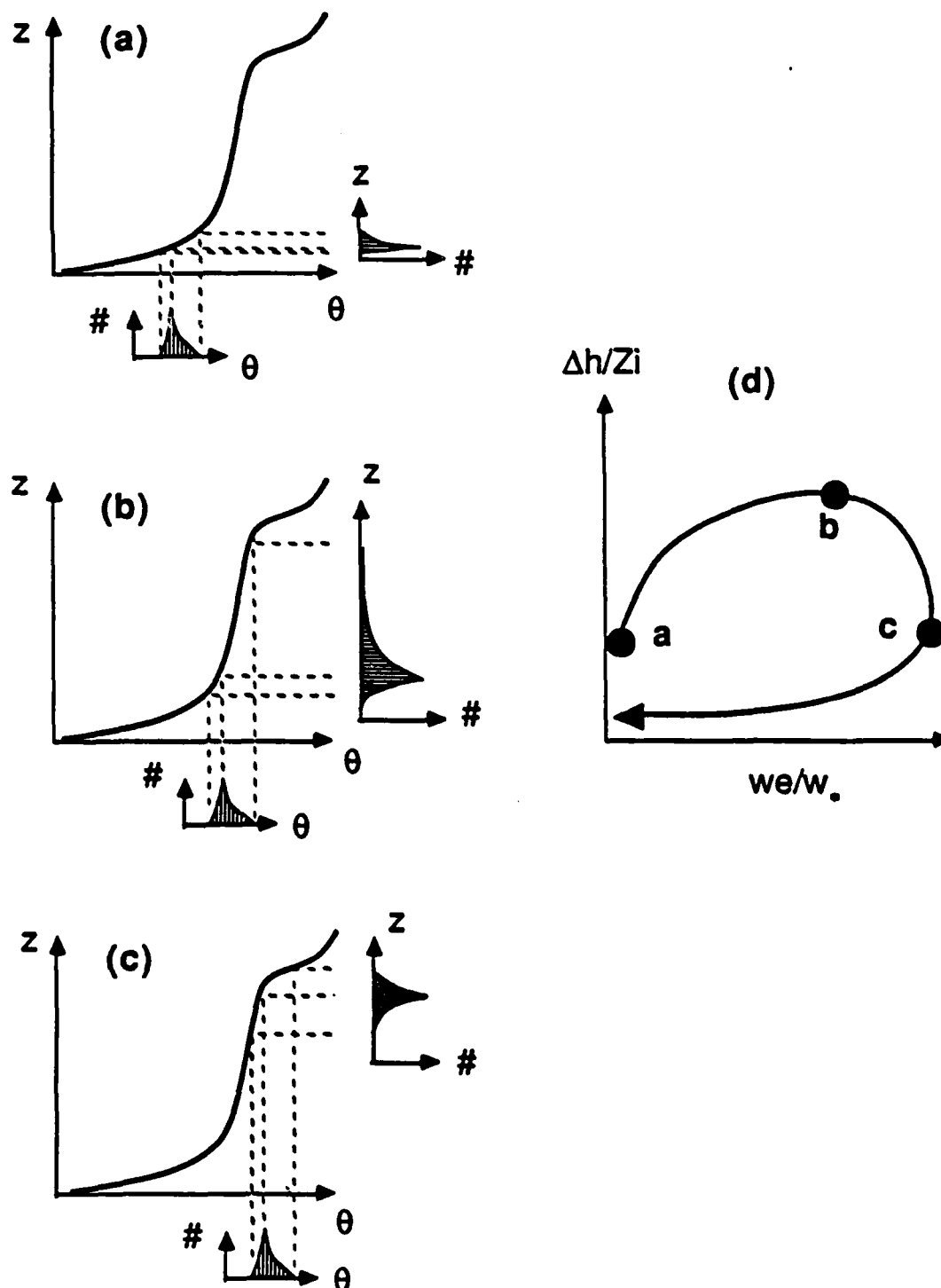


FIG. 8. Simple thermodynamic theory for entrainment zone evolution, based on the temperature distribution and equilibrium heights of rising thermals. (a) In mid-morning the frequency distribution of surface-layer air temperatures (θ versus θ) is remapped into an entrainment zone distribution (z versus θ) based on the early morning potential temperature sounding (heavy solid line). (b) By late morning the whole distribution of surface layer temperatures has shifted to the right because of warming, allowing the hottest thermals to penetrate to the higher capping inversion. This causes a thick entrainment zone, while the average ML depth is still relatively small. (c) A bit later, the average ML top (the peak in the z vs θ distribution) rapidly rises, and the entrainment zone thickness decreases. (d) The resulting normalized entrainment zone depth vs w_e/w_* exhibits a hysteresis cycle (a, b, c marks correspond to the times of the respective subfigures), assuming that the surface layer temperature distribution is asymmetric and the initial temperature sounding is nonlinear.

The distribution of surface-layer temperatures has strong central tendency, and is well described by a Gaussian-like curve, or by double-exponential curves

(used here). Although the average surface layer temperature is usually warmer than that of the ML, not all surface-layer parcels might be warm enough to rise.

Thus, we anticipate that some portion of the cooler parcels don't rise. The resulting subset of parcels that rise has a double exponential distribution with a truncated cold-tail (Fig. 8).

When this truncated distribution is remapped with the environmental sounding into a distribution of local ML heights, we find that the ML height distribution can become more or less skewed because the warm side encounters a part of the sounding with different lapse rate than that encountered by the cooler rising thermals. This skewness, and particularly the asymmetric spreading of the tails away from the mean ML height, are most obvious during the rapid-rise phase of the ML in early morning (Fig. 8). Also, the coolest temperature of the truncated cold-tail is remapped into the truncated bottom definition of the EZ (Deardorff et al. 1980). The probability distribution of ML heights $p(z_i)$ is related to the distribution of parcel temperatures $p(\theta_v)$ by: $p(z_i)dz = p(\theta_v)d\theta_v$, where $d\theta_v/dz$ is the local lapse rate at z_i .

The asymmetry of the truncated surface-layer temperature distribution and the nonlinear lapse-rate shape of the initial temperature sounding are the primary reasons for the hysteresis cycle in the EZ evolution. Without the asymmetry, the normalized EZ thickness and entrainment velocity would increase during the start of the early-morning rapid rise, and both would decrease along the same curve after the rapid-rise phase. Asymmetric surface layer temperature distributions have been reported by Deardorff and Willis (1985), Mahrt and Paumier (1984), and Stull (1988). The asymmetry associated with only rising thermals is probably even greater than we can estimate by the data from the low-altitude aircraft flights, because some of the cooler air in the frequency distribution might not rise.

The above theory neglects second-order effects such as the change of temperature distribution shape during the day, and variable overshoot distance as a function of capping inversion strength. These effects appear to play only a minor role, and is discussed in section 4c. Nevertheless, we must recognize that the thermodynamic approach is an oversimplification of a complex set of interacting physical processes.

b. Model

To test this theory, we will use a simple thermodynamic model for ML growth and temperature evolution. First, the variation of surface buoyancy flux with time must be supplied as a boundary condition. This is integrated over time, from $t'' = 0$ representing the time shortly after sunrise when the surface buoyancy flux first becomes positive (i.e., heating), to time $t'' = t$, where t is the time of interest. The resulting integral gives the heat available, H_a , that can warm the ML:

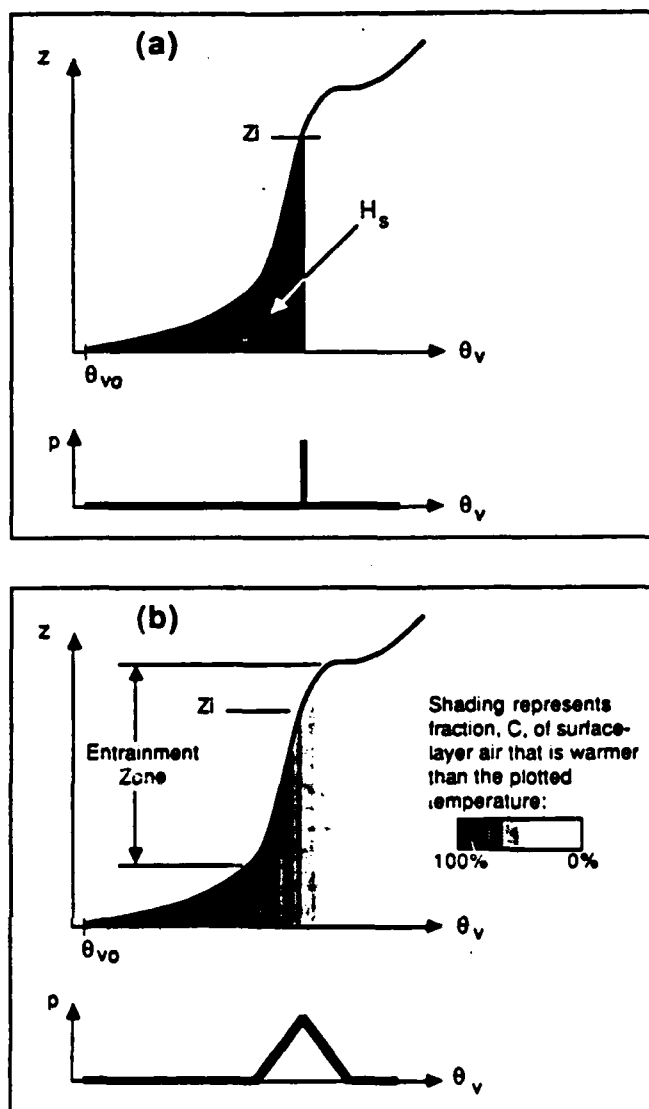


FIG. 9. (a) If all the air in the ML has the same potential temperature, then the probability, p , of finding air of that temperature is a Dirac delta function, and the average mixed layer depth can easily be determined from the projection of the ML temperature onto the early morning sounding, plotted as the heavy line. The shading under the sounding indicates the heat stored since sunrise. (b) If the probability distribution of air temperatures is as shown in the bottom then the shading under the sounding indicates the fraction of air that is warmer than the plotted temperature.

$$H_a = \int_{t''=0}^t \overline{w'\theta'_{vs}} dt'' \quad (9)$$

where kinematic units of $K \cdot m$ are used for H_a and H_s . As heating causes the ML potential temperature to warm, the warmer air represents heat stored, H_s , in the air. If we neglect the heating associated with entrainment (an appropriate assumption for the simple encroachment approach), then the heat stored must equal the heat available: $H_s = H_a$.

For a simple idealized thermodynamic ML model with adiabatic potential temperature in the ML up to

the altitude where it intersects the morning sounding (Fig. 9a), the heat stored is simply the area under the curve (shaded in Fig. 9a):

$$H_s = \int_{\theta_v''=\theta_{v0}}^{\theta_v''} z(\theta_v'') d\theta_v'' \quad (10a)$$

where $z(\theta)$ describes the early morning temperature sounding, and θ_{v0} is the potential temperature of the sounding at the surface (i.e., it is the initial ML temperature in the early morning).

We assume a distribution, $p(\theta)$, of temperatures at any given time during the day. For example, suppose that 20% of the air has a temperature of 20° (± 0.5)°C, 60% is 21° (± 0.5)°C, and 20% is 22° (± 0.5)°C. This means that 100% of the air was heated to 19.5°C or warmer, 80% of the air was heated to 20.5°C or warmer, and 20% was heated to 21.5°C or warmer. For an arbitrary distribution, we can rewrite (10a) in its more general form as

$$H_s = \int_{\theta_v''=\theta_{v0}}^{\infty} C(\theta_v'') z(\theta_v'') d\theta_v''. \quad (10b)$$

The "complementary cumulative probability distribution" [$C(\theta_v'') = 1 - P(\theta_v'')$, where $P(\theta_v'')$ is the cumulative probability distribution] is defined by

$$C(\theta_v'') = 1 - \int_{\theta_v''=\theta_{v0}}^{\theta_v''} p(\theta_v'') d\theta_v''. \quad (11)$$

To make a forecast, the heat available is first calculated by numerically integrating (9) up to the time of interest. Then a functional form for the *shape* of p (or alternately C) is assumed. Next, an iterative procedure is used to shift the *location* of the p or C distribution to warmer or cooler temperatures until the heat stored equals the heat available. A numerical integration of (10b) is performed at each step of the iteration to determine the heat stored. When the procedure is repeated for a sequence of times during the day, the result is a quantitative prognostic solution for ML depth and EZ depth analogous to the qualitative sketch of Fig. 8.

c. Forecasts of EZ depth

To determine the shape of the probability distribution, p , we fit a double exponential function to the temperature distribution from the aircraft data (surface-layer flights) by equating the second moments (and therefore the standard deviations, s_θ). For simplicity, we used potential temperature rather than virtual potential temperature for these forecasts, and for the associated soundings and surface heat fluxes. A symmetric double-exponential probability distribution *shape* is used:

$$p(\theta) = \frac{(0.5/\theta_e) \exp(-|\Delta\theta|/\theta_e)}{[1 - \exp(-\Delta\theta_w/\theta_e)]} \quad \text{for} \quad -\Delta\theta_w \leq \Delta\theta \leq \Delta\theta_w \quad (12)$$

where $\Delta\theta = \theta - \theta_m$; θ_m is the temperature of the mode (i.e., the *location*) of the frequency distribution (θ_m is median for the symmetric distribution, and corresponds to z_i when remapped into an entrainment zone distribution), θ_e is the e -folding distance of the exponential, and $\Delta\theta_w$ is the temperature difference between the warm tail cutoff and the mode.

Although (12) is normalized to make 100% of the modeled temperatures fall between $\pm\Delta\theta_w$, we assume less than 100% of the temperatures are warm enough to rise as buoyant thermals. Thus, a cold-tail cutoff is chosen based on the observed data such that $|\Delta\theta_c| < |\Delta\theta_w|$, where $\Delta\theta_c$ is the temperature difference between the cold tail cutoff and the mode. The result is an asymmetric distribution accounting for 90% of the surface-layer air, which maps into an entrainment zone distribution that also accounts for 90% of the air (as discussed in section 3b).

Using the entrainment zone results from Deardorff et al. (1980), we truncated the warm tail at $|\Delta\theta_w| = 3.0s_\theta$, and the cold tail at $|\Delta\theta_c| = 1.53s_\theta$. This approach was taken because the resulting distribution of potential temperatures maps directly into the proper distribution of ML height as was modeled by Wilde et al. (1985), assuming a linear early-morning sounding. An alternative would have been to truncate the warm tail at the maximum temperature observed by the aircraft, and the cold tail at something warmer than the minimum observed temperature (because the minimum temperature would probably not be buoyant

TABLE 3. Temperature frequency distribution parameters calculated from Queen Air surface-layer (low altitude) flights during BLX83. The parameters are: e -folding temperature, θ_e ; difference between the warm temperature cutoff and the mode, $\Delta\theta_w$; and difference between cold temperature cutoff and the mode, $\Delta\theta_c$ (see text for distribution function equation). Also listed are the observed standard deviation of temperature s_θ , and half the observed temperature range (to compare to $\Delta\theta_c$ and $\Delta\theta_w$). Due to lack of aircraft data for 1 June 83, the e -folding parameter for that case was set equal to the mean of the other e -folding parameters.

Date (June 1983)	Parameters			Observations	
	θ_e (°C)	$\Delta\theta_c$ (°C)	$\Delta\theta_w$ (°C)	s_θ (°C)	Half width (°C)
1	(0.184)	(0.282)	(0.552)	no data	no data
4	0.185	0.280	0.555	0.217	0.635
7	0.181	0.277	0.543	0.241	0.909
12	0.194	0.297	0.582	0.224	0.643
14	0.176	0.269	0.528	0.222	0.728
15	0.180	0.274	0.540	0.239	0.900
16	0.190	0.291	0.570	0.245	0.853

enough to rise to the entrainment zone). We tried both methods, and found that the forecast is sensitive to the distribution chosen (see the sensitivity analysis of section 4d). Table 3 lists the distribution parameters used.

From Table 3, it is obvious how little the distribution parameters vary from day to day at the BLX83 field site. During any of the individual fair-weather days used in this study, no consistent trends or variations of distributions parameters were observed with time, although apparently there were random fluctuations associated with sampling error. Based on this data, we will assume for simplicity that the distribution shape is invariant during any one day. We expect, however, that the distribution shape would be different over other sites, because of differences in land-use patterns (Hechtel and Stull 1985).

For the 15 June 83 case, there were early morning soundings from Canton, Ft. Sill, and Oklahoma City (OKC) [see Stull and Eloranta (1984) for a map of instrument locations]. Oklahoma City was the closest to the lidar, but Canton provided the greatest vertical resolution. We used an average smooth sounding (drawn by eye) with elevated temperature inversion location and residual layer potential temperature midway between those of the observed soundings, shown in Fig. 10a. This sounding provides the *initial condition* for the forecast. Figure 10b shows the average surface-heat-flux evolution for 15 June 1983, and the associated error bars based on the observed range of the data. This dataset provides one of the *boundary forcings* for the model.

The complementary cumulative probability distribution is computed from (12) to be

$$C(\theta) = \begin{cases} 1.0 & \text{for } \Delta\theta < -\Delta\theta_w \\ 0.5 + A[1 - \exp(\Delta\theta/\theta_e)] & \text{for } -\Delta\theta_w \leq \Delta\theta \leq 0 \\ 0.5 - A[1 - \exp(-\Delta\theta/\theta_e)] & \text{for } 0 \leq \Delta\theta \leq \Delta\theta_w \\ 0 & \text{for } \Delta\theta_w < \Delta\theta \end{cases} \quad (13)$$

Although this is the full symmetric distribution, we use only the range between $\Delta\theta_e < \Delta\theta \leq \Delta\theta_w$ (i.e., we use an asymmetric subrange of the distribution, as listed in Table 3).

While the thermodynamic forecast model is run, subsidence is applied as an additional external forcing. The initial sounding is compressed by the subsidence, and the overall heat stored and heat available are reduced by an appropriate amount (assuming the ML potential temperature is adiabatic within the ML and does not vary due to subsidence, but the area under the curve is less because the sounding is lower). The entrainment zone heights from the forecast model are then smoothed with the same Gaussian weighting

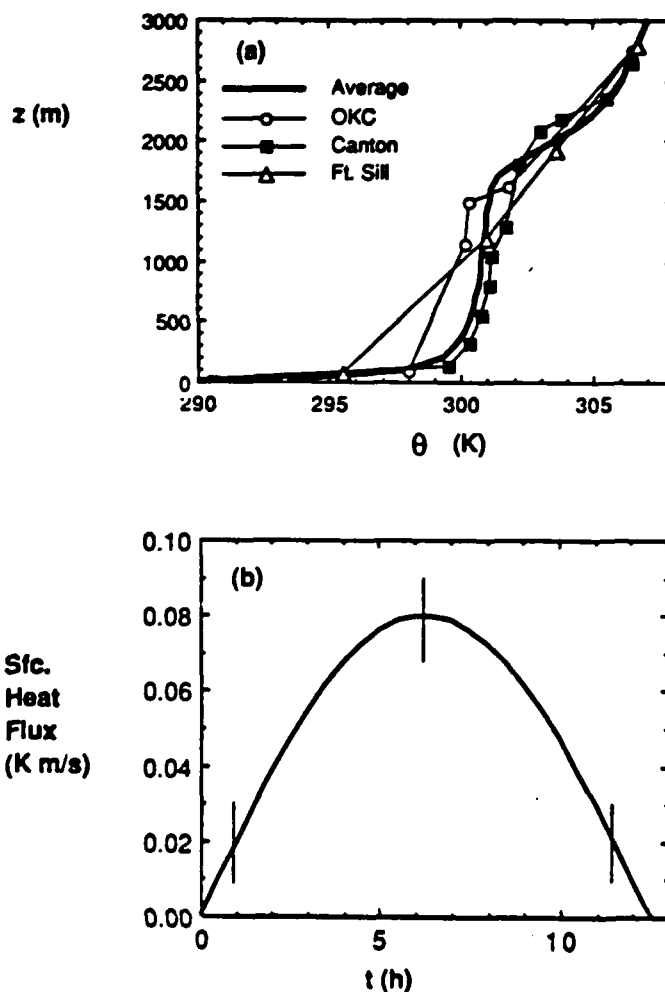


FIG. 10. Initial and boundary conditions for the 15 June 83 forecast. (a) Early morning soundings observed near the BLX83 field site, and the smooth sounding used for the forecast (heavy line). (b) Surface heat flux evolution, and associated range indicated by the error bars.

function as described in section 3b to make the forecasts comparable to the observed data.

The forecast result shown in Fig. 11 is an EZ curve that shows hysteresis-like behavior similar to that of the observed 15 June 1983 case. The magnitudes of both the normalized EZ thickness and the entrainment velocity are realistic, but the timing is incorrect. This error in timing is believed to be associated with errors in the thermodynamic initial and boundary conditions. The sensitivity of the forecast to these conditions are summarized in section 4d.

Appendix F shows the EZ forecasts for the other BLX83 case-study days for which there were initial and boundary condition data. For all of the fair-weather cases (Fig. F1) the model produces a hysteresis cycle. The vertical spreads in the modeled cycles, however, are much too narrow compared to the observed vertical spreads (Fig. 6). Also, the magnitudes of the peak entrainment velocities are only about half of the observed values. The modeled normalized EZ depths are also

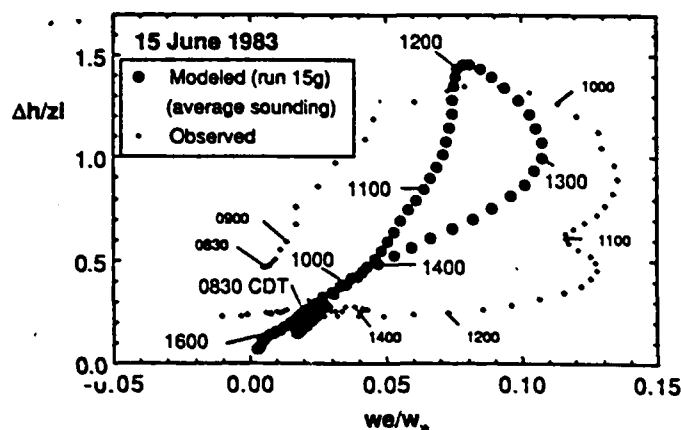


FIG. 11. Model simulation of the entrainment zone thickness evolution for 15 June 1983, using the smooth "average" sounding from Fig. 10a.

too small. Both of these problems might be related to the smoothed sounding that was specified for these cases. If a more-nearly adiabatic residual layer had been used in the smooth sounding (similar to portions of the individual observed soundings) then both the EZ thickness and the normalized entrainment velocity would have been significantly larger during the rapid rise phase of the ML. This is demonstrated in the next section for the 15 June case.

d. Sensitivity study

Although we find that hysteresis-cycle EZ behavior is predicted for a large variety of soundings and heat-flux profiles, we also note that the precise shape and timing of the cycle was very sensitive to the thermodynamic input: the heat flux (giving heat available) and the initial sounding (giving heat stored, when integrated to the ML potential temperature). Since heat available equals the heat stored, it is apparent that changes of either forcing cause similar impacts on the forecast. We will look at just the impact of the initial sounding here.

Figure 12a shows the forecast using the Oklahoma City sounding for the 15 June 1983 case, instead of the smoothed "average" sounding. The peak EZ thickness and entrainment rate are reached at about 0930 CDT, much earlier than that using the smooth sounding. If the Canton sounding is used instead, the peaks are reached between 1200 and 1300 CDT, and the entrainment rate is not as great, as shown in Fig. 12b. Also, there are other extra loops in the hysteresis behavior. The extra loops are associated with changes of stability with height (i.e., with kinks or nonlinearity in the sounding), and the change in timing is associated with both the mean temperature of the residual layer and the altitude of the inversion that caps the residual layer. The same surface heat flux forcings were used for both cases.

Appendix G compares observed and predicted values of z_i and Δh as a function of time for the various soundings used in this sensitivity study. For this one case, the observed average ML depth rises to about 1700 m, compared to a modeled rise to only about 1200 m. This might be related to subsidence and advective changes in the location and strength of the capping inversion. It can also be partially explained by the neglect of overshoot in the simple thermodynamic model. The EZ thickness, however, is approximately of the correct magnitude. For both z_i and Δh , there are large differences in the model forecasts when OKC vs Canton soundings are used for the initial conditions. For example, the time when Δh first increases differs by about 2 hours between the OKC and Canton cases.

The change in EZ forecast appears to be very sensitive to these thermodynamic initial and boundary conditions. We suggest that the real atmosphere is just as sensitive to these conditions as our model, because the real atmosphere must also conserve heat. Given the typical errors in rawinsonde soundings and typical mesoscale horizontal variability, one should expect model forecast errors of the same order as we demonstrated here.

e. Discussion

The differences between the observed and modeled EZ curves might be based on the oversimplifications

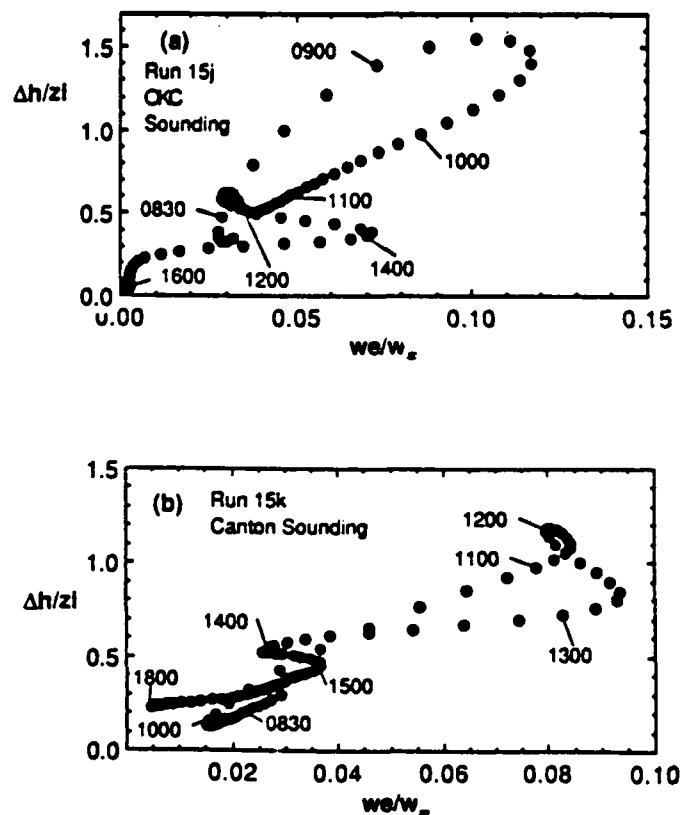


FIG. 12. Same as Fig. 11, except using the (a) Oklahoma City, and (b) Canton rawinsonde soundings for the initial conditions.

of the model. First, the neglect of wind shear across the EZ, and the neglect of surface stress can play a role. Second, advection is almost always a large term over nonuniform land surfaces, but was not included in either the model or the observations. Third, the model describes an EZ where all thermals are always at their level of neutral buoyancy, whereas the lidar measures slices through thermals (and does not always see the tops of thermals) that can overshoot above their level of neutral buoyancy, and which might have not reached their maximum height at the time of observation. Fourth, momentum and kinetic energy balances can cause the EZ thickness to temporarily deviate from that given by simple thermodynamic equilibrium. Fifth, interactions between individual thermals are neglected.

Another aspect of the oversimplification is based on the mapping of the temperature distribution into an entrainment zone distribution. By using the near-surface temperature distribution, we are implicitly requiring that all of the air associated with this distribution rise into the entrainment zone. The entrainment zone also includes downward-moving entrained air by definition, however, which we have neglected. One possible way to incorporate the downward-moving air is to use the continuity equation. Each rising thermal must be associated with a corresponding amount of downward moving air, by continuity. Thus, it might be possible to use an even more skewed temperature distribution to give only the top portion of the EZ (i.e., in the range $h_2 > z > z_1$), and assume that the thickness of the bottom portion (i.e., in the range $z_1 > z > h_0$) is proportional to the thickness of the top portion. This approach might open the modeled hysteresis EZ curves to look more like those observed.

5. Conclusions

Measurements of the convective ML made during the BLX83 and CIRCE field experiments with a ground-based lidar indicate that the normalized EZ depth ($\Delta h/z_1$) exhibits a cyclic or hysteresis behavior with time, when plotted against normalized entrainment velocity (w_e/w_*). Although portions of the hysteresis curve can be approximated by diagnostic relationships (Stull 1973; Boers 1988; and Deardorff 1983), the complete behavior over the period from sunrise

until sunset is better described with a prognostic relationship.

At least a portion of the hysteresis cycle for free-convection cases can be explained by simple thermodynamic arguments. At any instant in time, the surface layer contains air of a variety of temperatures, associated with both natural fluctuations and with variations in land use. Simple parcel theory suggests that the different-temperature air parcels will rise to different equilibrium heights, where the thickness of this height range defines the EZ. Asymmetry of the surface-layer temperature distribution, when mapped into an entrainment zone distribution using the initial sounding, is responsible for the cyclic EZ behavior with time, as sketched in Fig. 8. Downward entrainment associated with the upward rising thermals might also contribute to the cyclic EZ behavior.

A simple thermodynamic model for entrainment zone thickness simulated the hysteresis-cycle evolution of the normalized EZ thickness as a function of the normalized entrainment velocity. The shape of the cyclic curve from this model is sensitive to the shape of the initial temperature profile in the morning, and to the evolution of surface heat flux. This simple thermodynamic approach does not appear to work as well for days of strong wind shear, mechanical mixing, and advection.

Acknowledgments. This research was supported by National Science Foundation (NSF) grants ATM-8211842, ATM-8414371, ATM-8511196, and ATM-8822214, and by Army Research Office (ARO) grant DAAL 03-86-K-0024. The Queen Air aircraft was operated by the National Center for Atmospheric Research (sponsored by NSF). We thank Roger Vachalek for his extensive and expert analysis of the lidar data to determine the entrainment-zone heights. Marv Wesely, Rich Coulter and their colleagues at Argonne National Laboratory (ANL) are gratefully acknowledged for their micromet, sodar, and kytoon measurements during both BLX83 and CIRCE. During the final stages of this research, the second author was supported as a visiting scientist at DFVLR (Deutsche Forschungs- und Versuchsanstalt für Luft- und Raumfahrt e.V.) German Aerospace Research Establishment. For this invitation to work with the German scientists, we thank Anne Jochum.

APPENDIX A

Observed Entrainment Zone and Mixed-Layer Depth Evolution

Observed evolution of the top (h_2) and bottom (h_0) of the entrainment zone, of average mixed-layer depth (z_i), and of entrainment zone thickness (Δh) are plotted (similar to Fig. 2). The dataset is from BLX83 field program ground-based lidar observations that were smoothed (see main text).

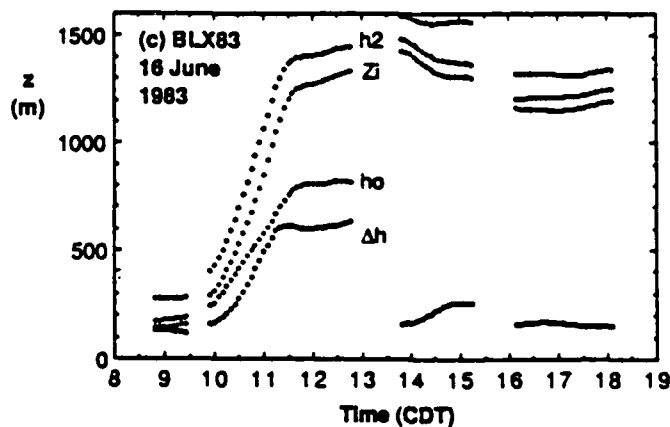
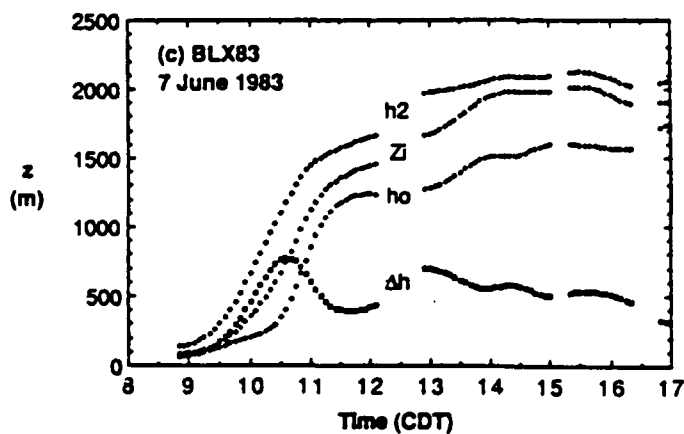
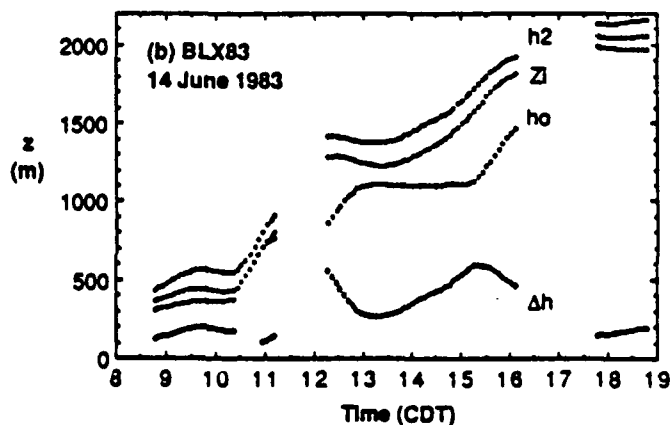
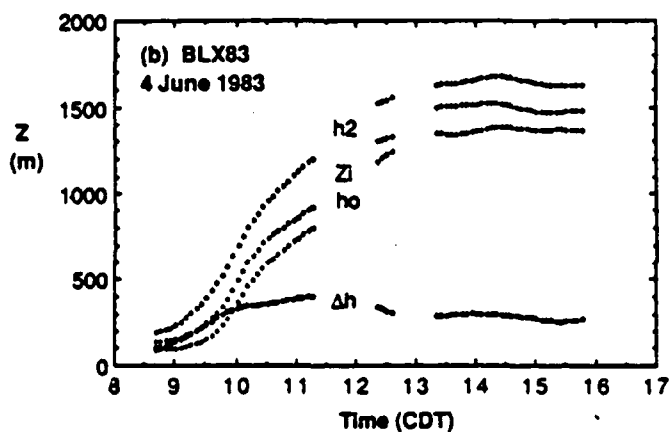
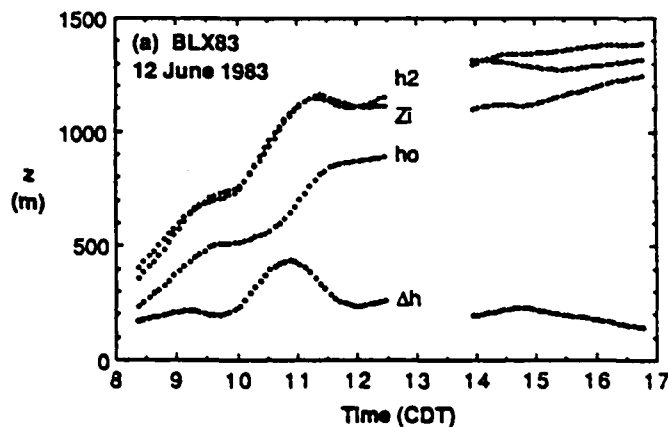
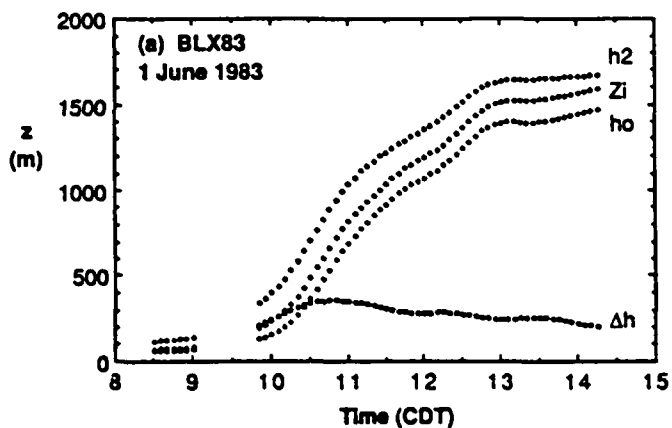


FIG. A1. Fair-weather cases for BLX83: (a) 1 June; (b) 4 June; and (c) 7 June 1983.

FIG. A2. Variable-weather cases for BLX83: (a) 12 June; (b) 14 June; and (c) 16 June 1983.

APPENDIX B

$$\Delta h/z_i$$

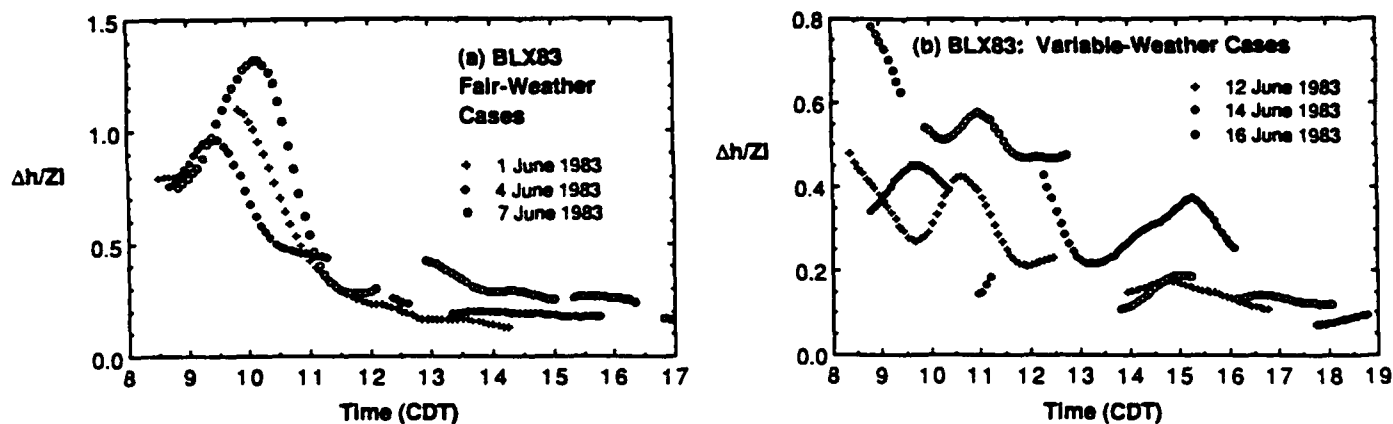


FIG. B1. Plotted is the observed evolution of entrainment zone thickness (Δh) normalized by the average mixed-layer depth (z_i) for the BLX83 field experiment (similar to Fig. 3 in the main text) for: (a) fair-weather cases; and (b) variable-weather cases.

APPENDIX C

$$w_e$$

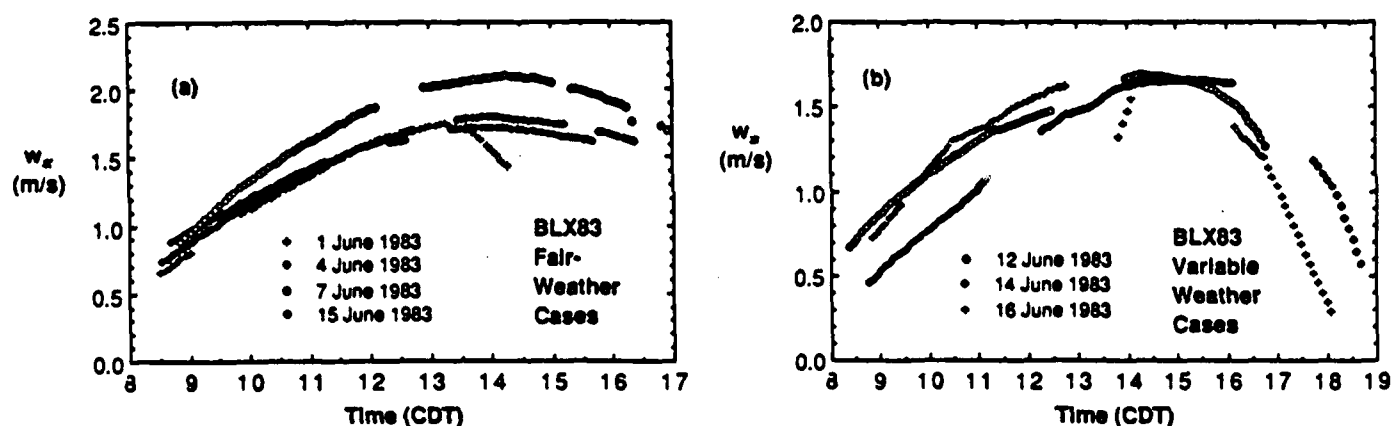


FIG. C1. Observed evolution of the free convection scaling velocity, w_e during the BLX83 field program are shown for: (a) fair-weather cases; and (b) variable-weather cases.

APPENDIX D

Divergence

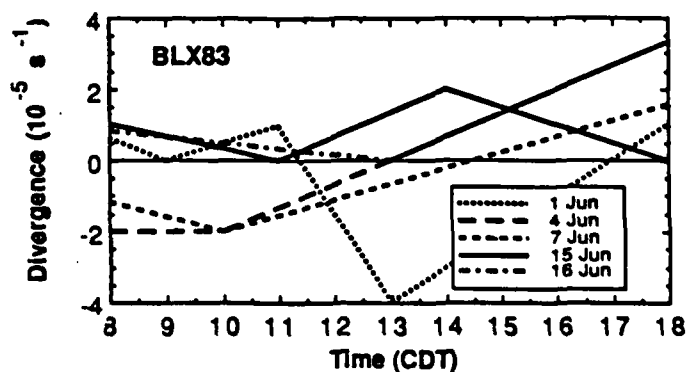


FIG. D1. Observed evolution of mean mixed-layer divergence during the BLX83 field experiment are presented based on estimates from Doppler radar, surface stations, lidar, and rawinsonde observations (Vachalek 1987, 1988).

APPENDIX E

Observations are presented for: local rise rate of the average top of the mixed layer ($\partial z_i/\partial t$) as observed by lidar; subsidence rate ($-w_L$) at the mixed-layer top based on divergence from appendix D; and entrainment rate (w_e) calculated as the sum of the other two terms, neglecting advection and assuming no venting of air through cumulus clouds.

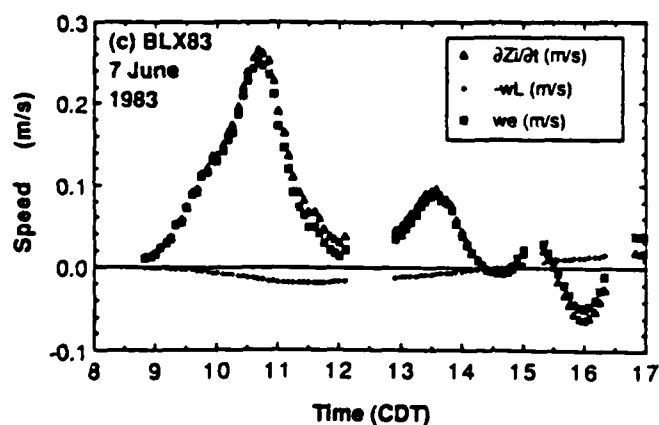
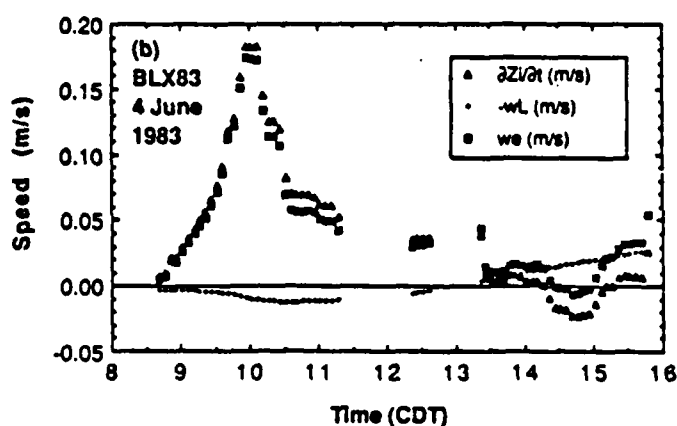
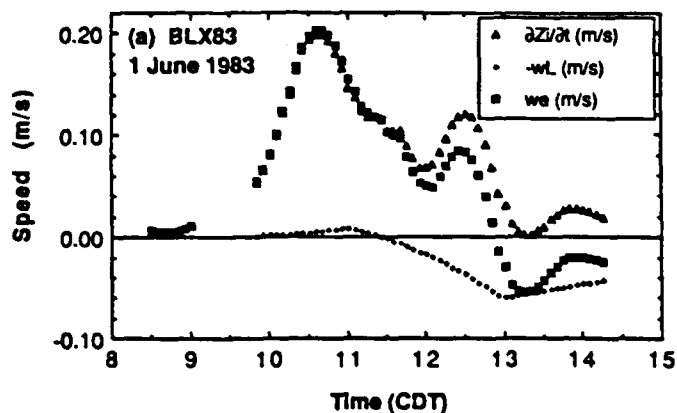


FIG. E1. Fair-weather cases for BLX83: (a) 1 June; (b) 4 June; and (c) 7 June 1983.

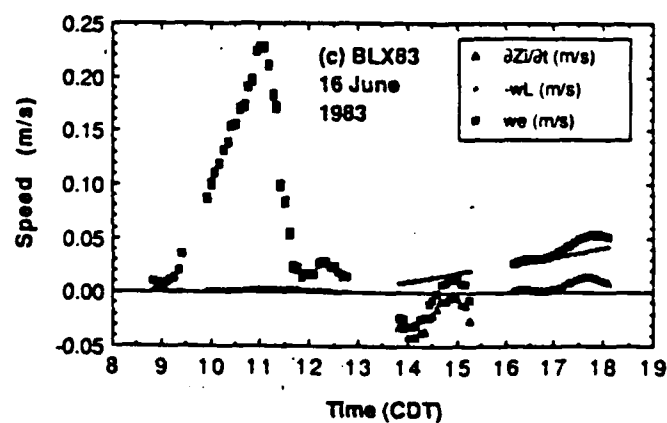
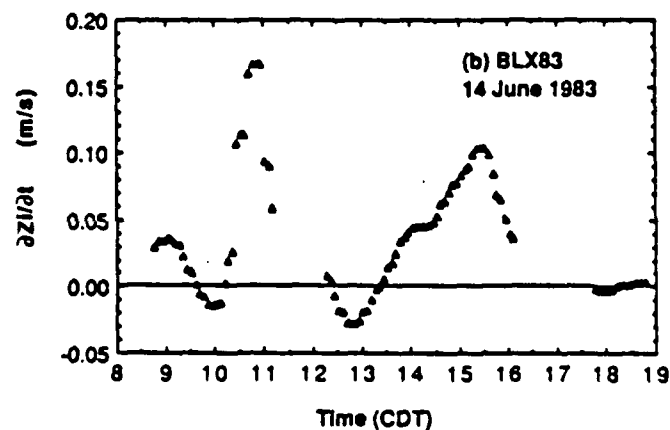
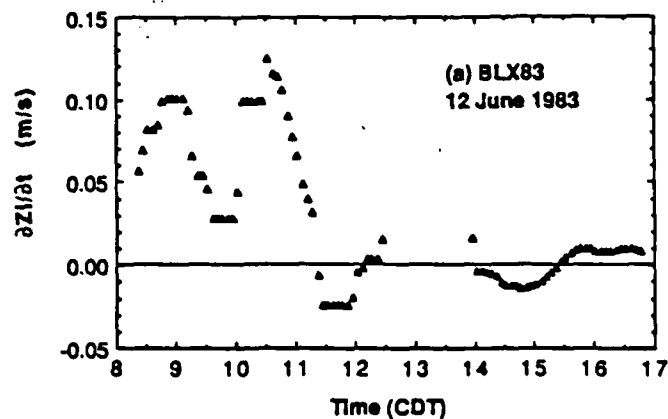


FIG. E2. Variable-weather cases for BLX83: (a) 12 June; (b) 14 June; and (c) 16 June 1983. Divergence data was not available for 12 and 14 June, therefore observations of only the local rise rate are given.

APPENDIX F

Forecasts of Cyclic Entrainment Zone Behavior

Model simulations of the normalized entrainment zone thickness ($\Delta h/z_i$) as a function of normalized entrainment rate (w_e/w_*). Local times (CDT) are indicated along the curve.

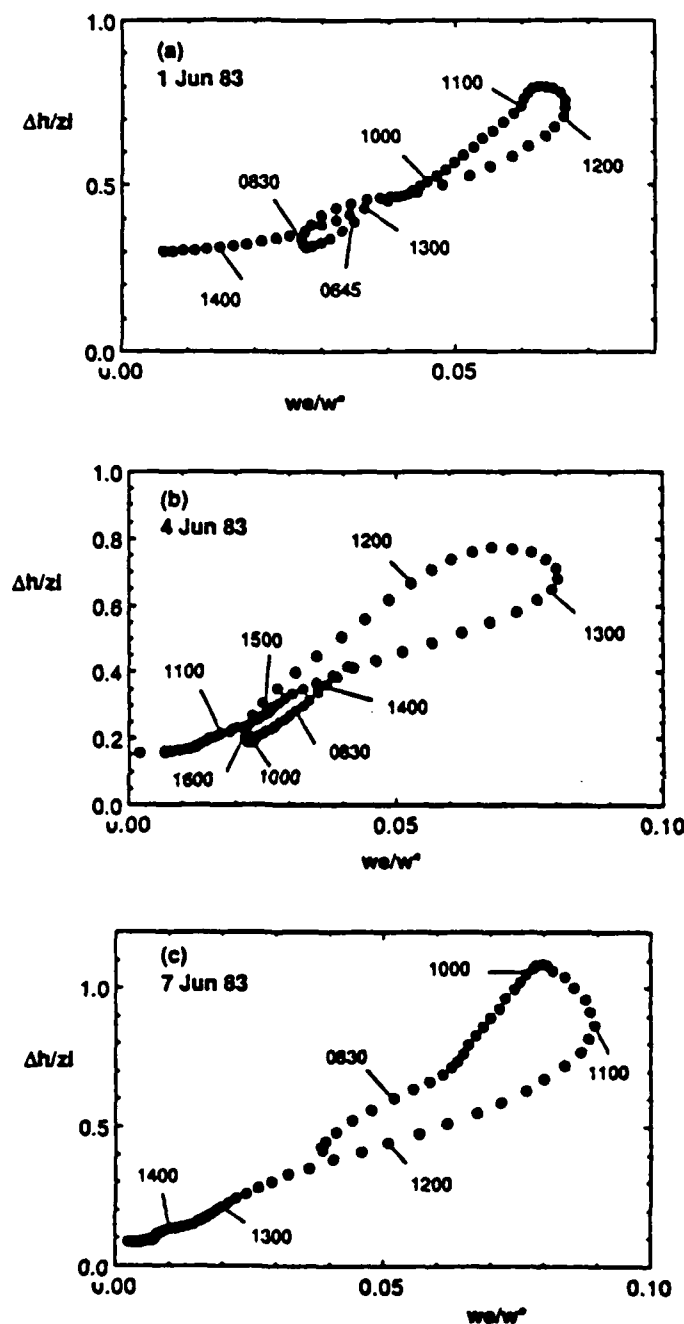


FIG. F1. Fair-weather cases for BLX83: (a) 1 June; (b) 4 June; and (c) 7 June 1983.

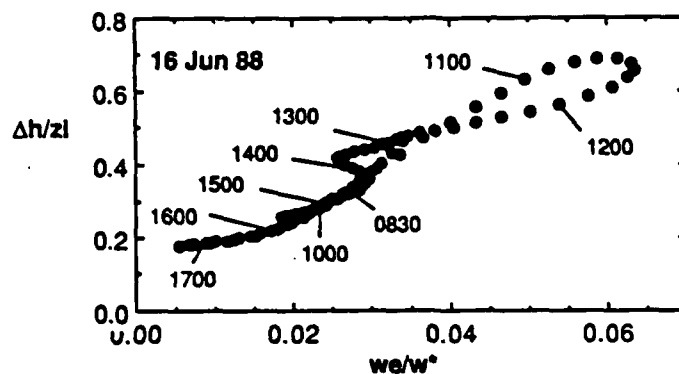


FIG. F2. Variable-weather case for BLX83 on 16 June 1983.

APPENDIX G

Sensitivity to the Initial Sounding

Model simulations of the entrainment zone thickness Δh and mean mixed layer depth z_i are plotted as a function of time, starting from three different initial soundings: Averaged, OKC (Oklahoma City), and Canton. The corresponding observed characteristics are also plotted for comparison.

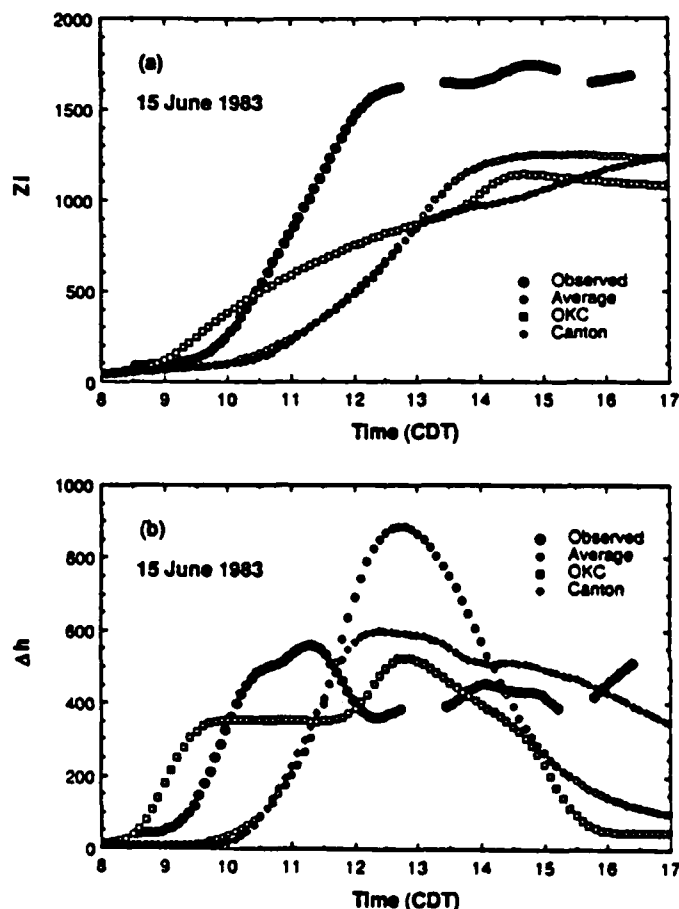


FIG. G1. (a) Mean ML depth and (b) entrainment zone thickness are plotted with time for the fair-weather case of 15 June 1983, BLX83. Both observed characteristics and model forecasts from different initial soundings are plotted.

REFERENCES

- Ball, F. K., 1960: Control of inversion height by surface heating. *Quart. J. Roy. Meteor. Soc.*, **86**, 483–494.
- Boers, R., 1989: A parameterization of the depth of the entrainment zone. *J. Appl. Meteor.*, **28**, 107–111.
- , and E. W. Eloranta, 1986: Lidar measurements of the atmospheric entrainment zone and the potential temperature jump across the top of the mixed layer. *Bound.-Layer Meteor.*, **34**, 357–375.
- , E. W. Eloranta and R. L. Coulter, 1984: Lidar observations of mixed layer dynamics: tests of parameterized entrainment models of mixed layer growth rate. *J. Climate Appl. Meteor.*, **23**, 247–266.
- Carson, D. J., 1973: The development of a dry inversion-capped convectively unstable boundary layer. *Quart. J. Roy. Meteor. Soc.*, **99**, 450–467.
- , and F. B. Smith, 1974: Thermodynamic model for the development of a convectively unstable boundary layer. *Advances in Geophysics*, **18A**, 111–124.
- Caughey, S. J., 1982: Observed characteristics of the atmospheric boundary layer. *Atmospheric Turbulence and Air Pollution Modeling*, F. T. M. Nieuwstadt and H. van Dop, Eds., D. Reidel Publ., 107–156.
- Crum, T. D., and R. B. Stull, 1987: Field measurements of the amount of surface layer air versus height in the entrainment zone. *J. Atmos. Sci.*, **44**, 2743–2753.
- , R. B. Stull and E. W. Eloranta, 1987: Coincident lidar and aircraft observations of entrainment into thermals and mixed layers. *J. Climate Appl. Meteor.*, **26**, 774–788.
- Deardorff, J. W., 1983: A multilimit mixed-layer entrainment formulation. *J. Phys. Oceanogr.*, **13**, 988–1002.
- , and G. E. Willis, 1985: Further results from a laboratory model of the convective boundary layer. *Bound.-Layer Meteor.*, **32**, 205–236.
- , G. E. Willis and B. H. Stockton, 1980: Laboratory studies of the entrainment zone of a convectively mixed layer. *J. Fluid Mech.*, **100**, 41–64.
- Hechtel, L. M., and R. B. Stull, 1985: Statistical measures of surface inhomogeneity, and its potential impact on boundary layer turbulence. *Extended Abstracts: Seventh Symposium on Turbulence and Diffusion*, Boulder, Colorado, Amer. Meteor. Soc., 144–146.
- Hunt, J. C. R., J. C. Kaimal and J. E. Gaynor, 1988: Eddy structure in the convective boundary layer—new measurements and new concepts. *Quart. J. Roy. Meteor. Soc.*, **114**, 827–858.
- Mahrt, L., 1979: Penetrative convection at the top of a growing boundary layer. *Quart. J. Roy. Meteor. Soc.*, **105**, 969–985.
- , and J. Paumier, 1984: Heat transport in the atmospheric boundary layer. *J. Atmos. Sci.*, **41**, 3061–3075.
- Stull, R. B., 1973: Inversion rise model based on penetrative convection. *J. Atmos. Sci.*, **30**, 1092–1099.
- , 1976a: The energetics of entrainment across a density interface. *J. Atmos. Sci.*, **33**, 1260–1267.
- , 1976b: Mixed layer depth model based on turbulent energetics. *J. Atmos. Sci.*, **33**, 1268–1278.
- , 1983: *Operations Log and Data Inventory*. A technical document of the Boundary Layer Experiment—1983. 71 pp. (Available from Meteorology Department, University of Wisconsin, Madison.)
- , 1985: A fair-weather cumulus cloud classification scheme for mixed-layer studies. *J. Climate Appl. Meteor.*, **24**, 49–56.
- , 1988: *An Introduction to Boundary Layer Meteorology*. Kluwer Academic Publishers (Reidel), 666 pp.
- , and E. W. Eloranta, 1984: Boundary Layer Experiment 1983. *Bull. Amer. Meteor. Soc.*, **65**, 450–456.
- Tennekes, H., 1973: A model for the dynamics of the inversion above a convective boundary layer. *J. Atmos. Sci.*, **30**, 558–567.
- Turner, J. S., 1973: *Buoyancy Effects in Fluids*. Cambridge University Press, 367 pp.
- Vachalek, R. E., 1987: Case studies of divergence and vertical velocities calculated using different sensing systems. M.S. thesis, University of Wisconsin, Madison, 176 pp.
- , 1988: Subsidence estimates in the boundary layer. Preprints, *Eighth Symposium on Turbulence and Diffusion*, San Diego, CA, Amer. Meteor. Soc., 305–308.
- Wilde, N. P., R. B. Stull and E. W. Eloranta, 1985: The LCL zone and cumulus onset. *J. Climate Appl. Meteor.*, **24**, 640–657.
- Willis, G. E., and J. W. Deardorff, 1974: A laboratory model of the unstable planetary boundary layer. *J. Atmos. Sci.*, **31**, 1297–1307.
- Zeman, O., 1975: The dynamics of entrainment in the planetary boundary layer: a study in turbulence modeling and parameterization. Ph.D. thesis, The Pennsylvania State University, 150 pp.
- , and H. Tennekes, 1977: Parameterization of the turbulence energy budget at the top of the daytime atmospheric boundary layer. *J. Atmos. Sci.*, **34**, 111–123.

The calculation of area-averaged vertical profiles of the horizontal wind velocity from volume imaging lidar data

J. L. Schols* and E. W. Eloranta

Department of Meteorology, University of Wisconsin, Madison, Wisconsin

(Manuscript submitted 1 April 1990)

Abstract

Area-averaged horizontal wind measurements are derived from the motion of spatial inhomogeneities in aerosol backscattering observed with a volume imaging lidar. Spatial averaging provides high precision, reducing sample variation of wind measurements well below the level of turbulent fluctuations even under conditions of very light mean winds and strong convection, or under the difficult conditions represented by roll convection.

Wind velocities are measured, using the two-dimensional spatial cross correlation computed between successive horizontal plane maps of aerosol backscattering, assembled from three-dimensional lidar scans. Prior to the calculation of the correlation function, three crucial steps are used : The scans are corrected for image distortion by the wind during a finite scan time, a temporal high pass median filtering is applied to eliminate structures that do not move with the wind, and a histogram equalization is employed to reduce biases to the brightest features.

*Present affiliation : General Sciences Corporation, Laurel, Maryland 20707

1. Introduction

Convective motions in an unstable atmospheric boundary layer produce fluctuations in wind speed and direction. These velocity fluctuations scale with the convective scaling velocity, w_* , and have typical magnitudes of 1 m/s (Kaimal et al. 1976) which are spatially correlated within individual thermals. Thermal sizes scale on the boundary layer depth and have typical dimensions on the order of 1 kilometer; when longitudinal rolls exist the stream-wise correlation length becomes much larger. The above mentioned velocity fluctuations limit the accuracy with which the mean boundary layer wind can be estimated. In order to reduce errors in the mean much below w_* , instruments which make point measurements must rely on temporal averaging over a period long compared to the lifetime of a thermal or long compared to the time for a thermal to advect over the instrument. When the mean wind is small the required averaging times become long. For example with a 1 m/s mean wind and a 1 km deep boundary layer a single cell requires approximately 1000 seconds to pass a fixed sensor. Reduction in the sampling error much below w_* requires the passage of many thermals; this requires many hours of averaging.

Spatial averaging offers the possibility of reducing thermal scale fluctuations in the wind without long averaging times. This paper describes a lidar technique for obtaining area averaged winds measured using lidar observations of the drift of inhomogeneities in naturally occurring atmospheric aerosols. Spatial inhomogeneities in atmospheric boundary layer aerosol content are produced by a variety

of processes, including localized sources, and by the vertical entrainment of air from above. The displacement of these inhomogeneities can be measured between successive observations with an incoherent lidar system. These displacements allow calculation of wind velocities without use of Doppler techniques. Wind measurements have been obtained using space-time correlations (Eloranta et al. 1975, Kunkel et al. 1980, Sroga et al. 1980, Hooper and Eloranta 1986, Kolev et al. 1988) and two-dimensional spatial cross correlation techniques (Leese and Epstein 1963, Sasano et al. 1982, Ferrare 1984).

The University of Wisconsin Volume Imaging Lidar (VIL) is designed to produce a continuous sequence of three-dimensional maps of aerosol backscattering (Eloranta 1987, 1988). A relatively fast laser pulse repetition rate, fast angular beam scanning, and a fast data acquisition system allows this lidar to image Atmospheric Boundary Layer (ABL) structure over a ≈ 50 to 70 km^2 square area at ≈ 3 to 4 minute intervals. Each of these volume images contains ≈ 6 million measurements of aerosol backscattering.

In the present paper lidar profiles observed with the VIL are used to produce images of the aerosol structure on vertically stacked horizontal planes. These images are compared to similar images obtained a short time later to obtain independent estimates of the wind velocity at the altitude of each plane. The vertical profiles of the horizontal wind obtained by this process represent an area average over ≈ 50 to 70 square km.

2. Method of data analysis

The backscattered power, incident on the lidar receiver from a pulse of laser light, is described by the single scatter lidar equation (Collis and Russell 1976), which reads in a slightly modified form

$$P(r) = \frac{E}{r^2} \frac{A \cdot c}{2} \beta'(\pi, r) e^{-2 \int_0^r \beta_e(r') dr'} \quad (1)$$

where

- r = range from lidar,
- $P(r)$ = received power,
- E = transmitted laser pulse energy,
- A = area of receiver,
- c = speed of light,
- $\beta'(\pi, r)$ = volume backscatter coefficient per steradian
 = product of the aerosol scattering cross
 section per unit volume and the aerosol
 backscatter phase function
 = $\beta_s(r) P(\pi, r)/(4\pi)$,
- $\beta_e(r)$ = extinction cross section per unit volume.

The VIL data system : 1) normalizes each lidar profile to remove the energy variations between pulses, 2) corrects for the inverse range squared dependence and, 3) forms the natural logarithm of the normalized lidar profile. The stored data points S_{ij} are given by :

$$S_{ij} = \ln \left(\frac{P_{ij} \cdot r_j^2}{E_i} \right) \quad , \quad (2)$$

where

- i = index for i-th lidar profile ,
- j = index for j-th range element,
- r_j = $\delta r \cdot j$
= distance between lidar and j-th scattering range element,
- δr = range increment between successive data points

As a first step in the data analysis each lidar profile, S_{ij} , is rangewise high pass filtered by subtracting a moving median. The filtered lidar profile, S_{ij}^f , is given by

$$S_{ij}^f = S_{ij} - S_{ij}^m \quad , \quad (3)$$

where

$$S_{ij}^m = \text{Median} \{ S_{il} \} ; j-n \leq l \leq j+n \quad , \quad (4)$$

and n is the width of the spatial median. This filter eliminates small intensity fluctuations produced by errors in the energy normalization of individual lidar profiles and large scale spatial variations produced by atmospheric attenuation. A median filter is used instead of a running average because it is much less sensitive to perturbation by extreme values, such as cloud reflections. In the ABL, aerosol inhomogeneities, which have spatial scales on the order of the boundary layer depth typically have the largest backscatter fluctuation (Kunkel et al. 1980). Since the boundary layer depth during the present experiment was ≈ 1

km, a filter length of 2 km proved to be a suitable choice.

The filtered lidar profiles making up a volume scan provide a spherical coordinate (range, elevation, azimuth) representation of aerosol inhomogeneities. In the second step of the data analysis, the representation is changed to cylindrical coordinates (altitude, range, azimuth). In this new Constant Altitude Plan Position Indicator (CAPPI) format, individual profiles appear to have been acquired by a lidar located at an altitude, z , and scanning horizontally through the same azimuth angles sampled in the original data. These new profiles are formed by linear interpolation between the nearest two lidar profiles recorded at the same azimuth angle. Figs. 1 and 2 show the geometry of this conversion.

Wind velocities are obtained from the CAPPI scans using an algorithm that includes the steps described below.

a. Correction for wind distortion

During the 3 to 4 minutes, required to complete a volume scan, the aerosol structures move along with the wind. The spatial structure is therefore distorted in the resulting lidar images. This effect is illustrated in Fig. 2. During one scan, the scanning radius, r , completes an arc, C , of length $r \cdot (\partial\phi/\partial t) \cdot T_s$, where $(\partial\phi/\partial t)$ is the azimuth angular scanning rate, ϕ the azimuth angle, t time, and T_s is the time needed to complete a volume scan. At the same time, an aerosol structure moves over a distance $D = V_t \cdot T_s$, measured along the scanning direction (V_t is the component of the aerosol velocity

perpendicular to the scanning radius).

The shape distortion of the aerosol structures in the CAPPI scans is corrected by a method similar to that described in Sasano et al. (1982). The correction for shape distortion is carried out by moving the individual aerosol backscatter profiles making up a CAPPI scan a distance

$$d = -v \cdot \delta t \quad , \quad (5)$$

where v is the average horizontal wind velocity in the scan area, and δt is the time difference between the start of a CAPPI scan and the time when this azimuth is sampled. Because profiles, making up the CAPPI scan, have been computed from a number of profiles in an elevated scan, δt is approximated with the time difference from the start of the volume scan to the start of a Range-Height Indicator (RHI) scan at this azimuth.

Finally, the data in each CAPPI scan were transformed from a cylindrical coordinate system to an image on a cartesian x,y -grid, in which the x axis was taken along the middle azimuth direction of a CAPPI scan. The origin of the x,y -grid coincides with the VIL position. The data values on the cartesian grid points were found through weighted linear interpolation between the grid points in the cylindrical coordinate system. The resolution of the cartesian grid was chosen to appropriately match the spatially averaged resolution of the cylindrical coordinate system.

b. Temporal high pass median filtering

The lidar images may contain structures that do not move with the wind. Such structures typically represent residual effects of attenuation, small nonlinearities in the lidar system response, or atmospheric features, which are anchored to the underlying terrain. In order to remove these features a temporal median image, $f^m(x, t_j)$, is constructed at each level, over a time interval centered about each image

$$f^m(x, t_j) = \text{Median} \{ f(x, t_j) \} ; i-l \leq j \leq i+l , \quad (6)$$

where $f(x, t_j)$ is the instantaneous aerosol backscattering distribution in an image at time t_j and at grid location $x = (x, y)$, and l is the width of the temporal median. The median image is thereafter subtracted from each image to obtain the temporal high pass median filtered image, $f^f(x, t_j)$

$$f^f(x, t_j) = f(x, t_j) - f^m(x, t_j) , \quad (7)$$

The median image is computed over a time period which is short compared to the rate at which the stationary background image changes, yet long enough such that many wind driven aerosol structures pass over each image point. This process removes the stationary features without affecting the motion of the inhomogeneities.

c. Histogram equalization

The instantaneous aerosol backscattering distribution, $f^f(\mathbf{x}, t)$, in an image can be represented as a distribution of pixel brightness values on a screen. \mathbf{x} is the pixel position in x, y coordinates. Anomalous bright targets may dominate, and thus bias the measured average velocity to the velocity of the brightest targets. To reduce this effect the pixel brightness distribution is made uniform by changing each pixel brightness value according to the transformation

$$f_U(\mathbf{x}, t) = P[f^f(\mathbf{x}, t)] \quad , \quad (8)$$

Here, $f_U(\mathbf{x}, t)$ corresponds to the new pixel brightness distribution. P stands for the cumulative probability distribution of the initial pixel brightness distribution. This transformation is illustrated in Fig. 3. Pixel brightness values that lie in the tails of the distribution are compressed, while the pixel brightness values in the central region are expanded. This operation is referred to as histogram equalization.

d. Spatial cross correlation function

To find an objective estimate of the aerosol motion averaged over the area of an image, the location of the maximum value of the two-dimensional spatial cross correlation function (CCF) is used. The CCF between the patterns $f_U(\mathbf{x}, t_1)$ and $f_U(\mathbf{x}, t_2)$, observed at the respective times t_1 and t_2 , is defined as

$$C(\delta\mathbf{x}, t_1, t_2 - t_1) = \int_S f_U(\mathbf{x}, t_1) \cdot f_U(\mathbf{x} + \delta\mathbf{x}, t_2) \cdot dS \quad , \quad (9)$$

where $\delta\mathbf{x} = (\delta x, \delta y)$ is a lag vector, and the integral is taken over an area S .

The CCF is computed between successive images, using the computationally efficient Fast Fourier Transform (FFT) technique (Otnes and Enochson 1972). Before the FFT technique is applied, each image is linearly detrended to take the spectral power out at zero wavenumber and to minimize leakage from low wavenumbers into the higher wavenumbers. The discrete FFT of an image on a regular x, y -grid with dimensions L_x and L_y is written as

$$F_U(k, t) = \sum_{m=1}^M \sum_{n=1}^N f_U(x, t) \cdot e^{-j \cdot 2 \pi k \cdot x} \quad , \quad (10)$$

where

k	= wave vector
	= (k_x, k_y)
k_x	= wave number in x direction
	= $(i_x \cdot M_x) / (M \cdot L_x)$
i_x	= lag index in x -direction $(-M/2 \leq i_x \leq M/2)$
M_x	= number of data points in x direction
M	= number of data points in x direction
	extended with zeroes to obtain a power of 2
k_y	= wave number in y direction
	= $(i_y \cdot N_y) / (N \cdot L_y)$
i_y	= lag index in y direction $(-N/2 \leq i_y \leq N/2)$
N_y	= number of data points in y direction
N	= number of data points in y direction
	extended with zeroes to obtain a power of 2
j	= imaginary unit, i.e. the square root of -1

- x = coordinate of data point on x,y -grid
 = (x,y)
 = $(m.L_x/M_x, n.L_y/N_y)$
 L_x/M_x = grid resolution in x direction
 L_y/N_y = grid resolution in y direction

The basic method uses the FFT's of two successive images to compute the cross spectrum, $G(k, t_1, t_2-t_1)$, where

$$G(k, t_1, t_2-t_1) = 4 \frac{L_x}{M_x^2} \frac{L_y}{N_y^2} F_u^*(k, t_1) \cdot F_u(k, t_2) \quad , \quad (11)$$

and an asterisk denotes a complex conjugate. The cross spectrum is then high pass filtered in wavenumber space to eliminate large spatial scale coherence which may be due to residuals introduced by the temporal high pass median filtering process. Care must be taken here that the spatial high pass filtering process does not remove the large scale coherent aerosol structure between successive images. For a typical ABL, where convective structures scale on the boundary layer depth, ≈ 1 km, a filter that removes scales larger than 2 km by 2 km is a good choice. The inverse FFT of the cross spectrum results in the cross covariance function

$$Cov(\delta x, t_1, t_2-t_1) = \frac{1}{4} \frac{M_x}{M} \frac{N_y}{N} \sum_{i=1}^M \sum_{j=1}^N G(k, t_1, t_2-t_1) e^{j.2\pi.k.\delta x} \quad , \quad (12)$$

The covariance function is the numerator for the definition of the CCF

$$C(\delta x, t_1, t_2-t_1) = \frac{Cov(\delta x, t_1, t_2-t_1)}{\sqrt{\sigma_1 \cdot \sigma_2}} \quad , \quad (13)$$

where σ_1 and σ_2 are the standard deviations of the successive

images. The square of the standard deviation of an image is defined as

$$\sigma^2 = \frac{1}{(M_x \cdot N_y - 1)} \sum_{m=1}^{M_x} \sum_{n=1}^{N_y} [f_u(x, t) - f_{u,ave}(x, t)]^2, \quad (14)$$

where

$$f_{u,ave}(x, t) = \frac{1}{M_x N_y} \sum_{m=1}^{M_x} \sum_{n=1}^{N_y} f_u(x, t), \quad (15)$$

To reduce statistical error, an average correlation function, $C_{ave}(\delta x, t_j, t_j - t_i)$, is then computed over successive images

$$C_{ave}(\delta x, t_j, t_j - t_i) = \frac{1}{j-i} \sum_{l=i}^{j-1} C(\delta x, t_l, t_{l+1} - t_l) \quad (16)$$

where the indices i and j refer to the times between which the averaging is carried out.

e. Location of the correlation maximum

In order to estimate the wind speed it is necessary to locate the maximum of the average correlation function, $C_{ave}(\delta x, t_j, t_j - t_i)$. Interpolation is required because this function is only available at discrete points, $\delta x = (m.L_x/M_x, n.L_y/N_y)$. In addition, the correlation function is also often quite flat near its peak, such that small noise fluctuations can move the apparent peak to one of several points adjacent to the maximum. An approximate location for the maximum, δx_{max} , is first obtained by searching for the peak in the two-dimensional array $C_{ave}(\delta x, t_j, t_j - t_i)$, which is smoothed by using a moving area average over 3 by 3 points. A bicubic natural non-

smoothing spline interpolation is applied to the unsmoothed average correlation function, around the array location δx_{max} . The position of the maximum of the spline function determines the horizontal displacement of the aerosol inhomogeneities. Dividing this displacement by the time separation between two successive images gives the wind velocity. A bicubic natural non-smoothing spline function is used for the interpolation around δx_{max} , since that function is smooth and preserves the shape of $C_{ave}(\delta x, t_j, t_j - t_i)$. Use of the bicubic natural non-smoothing spline interpolation improves the accuracy of the determination of the position of the maximum of the average correlation function to within a fraction of the grid resolution.

A first estimate of the horizontal wind velocity is obtained using the above described algorithm without the correction step for wind distortion. The first estimate of the wind velocity is then used to repeat the algorithm in its full extent to get a better value of the wind velocity. The algorithm converges rapidly requiring only one or two iterations.

3. Results

a. Site and instrumentation

Measurements were obtained between 25 June and 15 July 1987 on the Konza Prairie Long Term Ecological Research (LTER) site near Manhattan, Kansas, as part of FIFE (First ISLSCP* Field Experiment).

*International Satellite Land Surface Climatology Project

Sellers et al. (1988) give a brief description of the experiment. The primary 15 km by 15 km field site is a mostly treeless rolling prairie with altitude variations of roughly 50 m. The UW VIL system was located at a position next to the center of the site ($96^{\circ}32'19''\text{W}$ $39^{\circ}03'52''\text{N}$) at 448 m above sea level (MSL). The average elevation of the FIFE site is approximately 408 MSL. A summary of the UW three-dimensional VIL system parameters is presented in Table 1. A Doppler lidar system, operated by NOAA, was located next to the UW VIL. 16 Portable Automated Mesonet II (PAM II) stations operated by NCAR were located within 10 km of the UW VIL. A radiosonde receiver was also operated by members of Cornell University. The balloon launch location was at $96^{\circ}34'07''\text{W}$ $39^{\circ}06'59''\text{N}$, at 340 MSL, approximately 7 km north of the lidars.

b. Description of the data acquisition

The VIL provided a time sequence of three-dimensional maps of aerosol backscattering. Typical lidar volume scans consisted of 60 Range-Height Indicator (RHI) scans between the horizon and 10 degrees of elevation, with \approx 60 lidar profiles in each RHI. Individual RHI scans were spaced 0.5 degree apart in azimuth to cover a 30 degrees azimuthal sector. This resulted in a time separation between two successive images of 165 s, which was short compared to the lifetime of the coherent aerosol structures. A compromise had to be made between the angular width of the volume scans and the frequency of observation of the scans, as constrained by the laser repetition rate.

The angular size and timing of the images limits the maximum wind speed which can be measured. If the scan time is too long, or the angular sector is too small, the aerosol structure observed on one scan may have advected out of the scan area by the start of the next scan.

Two data sets, acquired under very different conditions, were chosen to test the wind measuring algorithm. The first was collected between 1321 and 1424 CDT on 1 July (CDT = GMT - 5 h) in a convectively driven boundary layer. The second data set was acquired between 0627 and 0657 CDT on 7 July in a largely shear driven boundary layer. Representative volume and CAPPI scans are shown in Figs. 4 and 5. Both data sets show bands of organized aerosol structures. On 1 July, these bands were mainly aligned with the wind. The weather was clear with scattered convective clouds. Surface winds measured by PAM stations were less than 2 m/s. The depth of the ABL changed from approximately 1100 m above the lidar site, at the start of the data set, to around 1300 m, at the end. Scattered convective clouds appeared on top of the convective plumes. On 7 July the aerosol bands were orientation basically perpendicular to the wind direction. The sky above the site was clear, and the surface sensible heat flux was small. A thunderstorm was approaching, and the winds were moderate to strong (3 to 10 m/s). This data set provided an example of shear driven turbulence, in contrast to the convective conditions of 1 July. Boundary layer depth grew from 300 m, at the beginning of the period to 500 m, at the end. The contrast between the aerosol structures and their background, i.e. the image contrast, decreased significantly during this period.

c. Computational results and accuracy

Figs. 6a-d illustrate the effect of various processing steps applied to the CAPPI scans obtained on 1 July. The convective, low wind speed conditions provided a particularly good test case for the performance of the temporal high pass median filtering step. The median image shows a clear picture of the background in which the aerosol structures are embedded. The histogram equalization step, which was applied to make the brightness distribution in the image uniform, enhances the visual contrast in the gray regions.

Fig. 7 displays a comparison of VIL determined winds with conventional measurements. On 7 July all profiles (upper part of the figure) show similar vertical shear. The UW VIL profile, at 062718 CDT, and the Doppler lidar profile, at 0611 CDT, agree very well, except below 300 m height. The UW VIL profile, at 065444 CDT, and the vertically averaged radiosonde profile, at 0704 CDT, match closely. The UW VIL profile looks smoother, as a result of the averaging over a 32 square km horizontal area. In the early afternoon of 1 July (lower part of the figure) the conditions were convective with almost no average wind. These conditions, together with the organized roll convection (see Fig. 4), caused large updrafts and downdrafts in the ABL. As a result bright and dark bands appeared in the images. In order to obtain a stable estimate of the horizontal wind velocity, it is therefore necessary averaging over an area of 12 km by 6 km. This allowed averaging over many convective cells, to obtain a consistent estimate of the mean wind velocity. The fluctuations in a UW lidar profile

between adjacent points are on the order of 0.1 m/s in speed and 10 degrees in direction. As expected, under almost windless conditions, with strong clear air convection, little vertical shear is evident. The Doppler lidar showed a wind speed profile which decreases with altitude. The difference between the UW VIL derived winds and the Doppler lidar determined winds are most likely due to sampling effects, caused by the much smaller averaging volume, represented by the Doppler VAD (= Velocity Azimuth Display) scan. The Doppler VAD wind measurement technique provided wind measurements, during a 2-minute sweep, for a volume consisting of a vertically oriented cone. The VIL was located at the vertex of the cone. Wind measurements at each altitude sample a ring around the lidar with a diameter which increases with altitude. The wind profile measured by the radiosonde balloon represents a point measurement of the wind velocity at each level. The wind profile, measured by the radiosonde drift, shows large variations that are caused by the turbulent motions on the balloon path. In this convective light wind case, the turbulent velocities scale with the convective scaling velocity w_* , which was approximately 1.5 m/s. The 30 minute average 10 m winds measured by PAM stations are also shown. Two successive averages are shown for each PAM station. Large differences exist between stations and between successive measurements. The scatter in the points on each profile, the differences between the profiles, and the variations in the PAM measurements are equal to or less than w_* .

Each of the individual steps of the wind measurement algorithm was found necessary in order to obtain smooth and accurate profiles. Fig. 8

shows 165 s average wind profiles, averaged over an 8 km by 4 km area. They were acquired in the morning of 7 July, between 062718 and 063003 CDT, when the image contrast was the highest (upper part of the figure), and at the end of this data set, between 065444 and 065729 CDT, when the image contrast was the lowest (lower part of the figure). The calculations were done, using all steps and deleting one step each of the algorithm. The data set contained 12 images, and the time separation between two successive images was 165 s. The correction for wind distortion has a larger effect in the upper part of the boundary layer, where the wind speed is higher. Wind direction is almost uniform throughout the boundary layer depth. Deleting this step at 062718 CDT leads to an overestimate of the horizontal wind speed throughout the boundary layer, because the direction of the wind component transverse to the scanning radius coincides with the clockwise scanning direction. At 065444 CDT, when there is little contrast between the aerosol structures and their background, omission of the correction for wind distortion does not always lead to an overestimate of the horizontal wind speed. In spite of the histogram equalization step, a few local bright spots in a low contrast image may still dominate the CCF computations. The area averaged wind velocity is then biased toward the apparent motion of these individual spots. Because of the median background in which the aerosol structures were embedded was changing rapidly the length of the temporal high pass median filter was selected to be 330 s, i.e. twice the time separation between two successive images. The temporal high pass median filter most strongly affects the regions near the surface and at the top of the

boundary layer. This is because topographic features are most prominent near the surface, while nonlinearities in the lidar system response or residual effects of attenuation are more likely near the top. When this step is not used the wind speeds are biased to low values by stationary features.

The computations showed little sensitivity to the length of the temporal high pass median filter. Fig. 9 shows the results, for the early 7 July data, after the image contrast had decreased substantially, at the end of this data set. Different choices of the length of the temporal high pass median filter, viz. 2 and 6 times the time separation between two successive images, resulted in differences smaller than 0.3 m/s in wind speed and 10 degrees in wind direction, for a 165 s average profile (upper part of the figure). These differences were reduced when more CCF's were averaged together. For a 330 s average the differences between the profiles calculated for different temporal median lengths become smaller than 0.1 m/s in speed and less than 10 degrees in direction. However, when the spatial high pass filtering of the cross spectrum (see Section 2.d), that eliminates scales larger than 2.5 km, is omitted, the profile for a median length of 6 time separations exhibits large errors (lower part of the figure). The high pass spatial filter apparently reduces sensitivity to the length of the temporal median. Fig. 10 shows the results of a calculation for different lengths of the temporal median, viz. 2640 and 3795 s, on 1 July. For 660 s averages the differences between the profiles is smaller than 0.1 m/s in speed and 10 degrees in direction. In addition, the profiles for the longer 24 image median look smoother, which indicates that this is a better choice for the median length for this convective, low wind speed

case.

In Fig. 11 CCF's are presented for both 1 July and 7 July data sets. The CCF's are shown as three-dimensional surfaces to enhance their visualization. The height of the peak with respect to the background is clearly depicted.

4. Discussion and conclusions

Horizontal wind speeds and directions within the atmospheric boundary layer were estimated by measuring the drift of aerosol backscattering patterns inside successive lidar images, using a two-dimensional spatial cross correlation technique.

The wind measurement algorithm, described in Section 2, has been validated by tests on ABL's, during FIFE, under two very different conditions, viz. a convective light wind case and a shear driven case with moderate to high wind speeds. The derived wind profiles were shown to be nearly insensitive to the choice of the length of the temporal high pass median filter, provided an additional spatial high pass filtering is used. The area averaging allowed accurate mean horizontal wind measurements, in the presence of turbulence, which degrades conventional observations.

A comparison of the lidar wind measurements with Doppler lidar and balloon borne radiosonde winds, displayed differences on the order of what is expected from the variations produced by different spatial and temporal averaging inherent in each technique. For example on 1 July internal consistency between winds independently calculated for

adjacent altitudes or times suggest that spatial averaging has reduced sampling errors well below the level of turbulent fluctuations. The variation between adjacent levels, of 5 to 10 minute average, lidar wind measurements, is smaller than 0.1 m/s in speed and 10 degrees in direction.

Acknowledgments. The authors thank Dan Forrest for designing an important part of the software for the data-acquisition system and subsequent processing of the data, and developing the programs for displaying the pictures. We also appreciate the helpful discussions, concerning the data analysis, with our colleagues. The data on balloon soundings of the ABL were collected and analyzed by W. Brutsaert and his colleagues of Cornell University. The Doppler lidar observations were acquired by W. Eberhard and colleagues of NOAA/ERL WPL. Their cooperation is greatly acknowledged. This work was supported by grants from ARO Grant DAA-G29-80-K-0079, NASA GRANT NAG 5-902 and DAAL03-86-K-0024.

REFERENCES

- Collis, R. T. H. and P. B. Russell, 1976 : Lidar measurement of particles and gases by elastic backscattering and differential absorption. *Topics in Appl. Phys.: Laser Monitoring of the Atmosphere*, E. D. Hinkley, Ed. ,14, 71-151.
- Eloranta, E. W., J. King and J. M. Weinman, 1975 : The determination of wind speeds in the boundary layer by monostatic lidar. *J. Appl.*

- Meteor.*, 14, 1485-1489.
- Eloranta, E. W., 1987 : Lidar observations of the atmospheric boundary layer. *Proc. Sixth Symp. Met. Obs. Ins., Amer. Meteor. Soc., Boston, Mass.*
- Eloranta, E. W., 1988 : A lidar system designed for three-dimensional time resolved mapping of atmospheric structure. *Proc. 14th Intern. Laser Radar Conf., ICLAS/IUGG.*
- Ferrare, R. A., 1984 : *Lidar observation of organized convection within the atmospheric mixed layer*. M. Sc. thesis, Department of Meteorology, University of Wisconsin Madison, 204 pp..
- Hooper, W. P. and E. W. Eloranta, 1986 : Lidar measurements of wind in the planetary boundary layer: The method, accuracy and results from joint measurements with radiosonde and kite. *J. Appl. Meteor.*, 25, 990-1001.
- Kaimal, J. C., J. C. Wyngaard, D. A. Haugen, O. R. Cote, Y. Izumi, S. J. Caughey and C. J. Readings, 1976 : Turbulence structure in the convective boundary layer. *J. Atmos. Sci.*, 33, 2152-2169.
- Kolev, I., O. Parvanov and B. Kaprielov, 1988 : Lidar determination of winds by aerosol inhomogeneities : Motion velocity in the planetary boundary layer. *Appl. Opt.*, 27, 2524-2531.
- Kunkel, K. E., E. W. Eloranta and J. M. Weinman, 1980 : Remote determination of winds, turbulence spectra, and energy dissipation rates in the boundary layer from lidar measurements. *J. Atmos. Sci.*, 37, 978-985.
- Leese, J. A. and E. S. Epstein, 1963 : Application of two-dimensional spectral analysis to the quantification of satellite cloud photographs. *J. Appl. Meteor.*, 2, 629-644.

- Otnes, R. K. and L. Enochson, 1972 : *Digital time series analysis*. John Wiley & Sons, Inc., N.Y., 467 pp.
- Sasano, Y., H. Hirohara, T. Yamasaki, H. Shimizu, N. Takeuchi and T. Kawamura, 1982 : Horizontal wind vector determination from the displacement of aerosol distribution patterns observed by a scanning lidar. *J. Appl. Meteor.*, **21**, 1516-1523.
- Sellers, P. J., F. G. Hall, G. Asrar, D. E. Strebel and R. E. Murphy, 1988 : The First ISLSCP Field Experiment (FIFE). *Bull. Amer. Met. Soc.*, **69**, 22-27.
- Sroga, J. T., E. W. Eloranta and T. Barber, 1980 : Lidar measurement of wind velocity profiles in the boundary layer. *J. Appl. Meteor.*, **19**, 598-605.

TABLE CAPTION

Table 1. University of Wisconsin lidar system parameters (1987).

Laser transmitter	
wavelength	1064 nm
beam pointing resolution	0.2 mrad
average output energy per shot	0.6 J
pulse repetition rate	30 Hz
pulse duration	≈ 7 ns
Receiver telescope	
optical area	0.5 m
field of view	adjustable (1.5 - 7 mrad)
detector	Silicon Avalanche Photodiode (RCA 30955E)
quantum efficiency	40 % at 1064 nm
spectral bandpass	1.0 nm (interference filter)
Data logging	
logarithmic amplifier	100μV to 6 V input range (=90dB)
A/D resolution	10 bit resolution
sampling rate	20 MHz max (10 MHz this study)
range resolution	7.5 m (15 m this study)
maximum range	15 km (this study)
preprocessing	VAX 11/750, LSI 11/73 and CSPI Array Processor
output	2.6 GByte write once optical disk, real-time display

FIGURE CAPTIONS

Fig. 1. Three of the 60 Range-Height Indicator (RHI) scans, forming a complete volume scan, are shown. The scanning pattern follows the lines a-b-c-d-e. Successive RHI scans are separated by $\delta\phi$ in azimuth. Synthetic constant altitude lidar profiles are then formed at selected altitudes, for example, along the dashed line h. Aerosol backscatter values in a range interval, between 1 and 2, at a constant altitude line, are found through weighted linear interpolation between data points at the intersections (1 and 2) of that line and the lidar profiles (p and q) in a RHI scan. Using all RHI scans, the data in a volume scan can be rearranged on vertically stacked Constant Altitude Plan Position Indicator (CAPPI) scans.

Fig. 2. A CAPPI scan is corrected for wind distortion by displacing each of its radial aerosol backscatter profiles over a distance $-V.\delta t$, where δt is the time elapsed since the start of a CAPPI scan.

Fig. 3a. The plot shows the probability density distribution (PDF :) and the cumulative probability distribution (CPD : _____) of pixel brightness values for an image on 1 July 1987 at 135649 CDT, at 400 m height above the lidar site.

Fig. 3b. The plot shows the same functions as in Fig. 3a, after the histogram equalization, using 256 levels of pixel brightness. The transformation for two pixel brightness values is illustrated in Fig. 3a with the dashed lines a and b. The region between these lines is expanded through the transformation, while the regions outside the lines are compressed. This results in an overall enhancement of the

contrast in the image.

Fig. 4a. Perspective three-dimensional view of convective cells in the ABL displayed over a high resolution SPOT picture (copyright CNES) of surface topography on 1 July 1987 at 1121 CDT under almost windless convective conditions. This type of display is prepared by selecting a contour layer to construct a solid surface through the volume of normalized aerosol backscatter data. A viewing position, the position of the display screen and the position of a light source is then selected. The lidar is located at the origin of the coordinate system provided in the picture. All dimensions are given in km. A fork shaped creek bed area is clearly visible on the surface, with one leg at 8 km and the other one between 5 and 8 km. The center azimuth angle of a volume scan was 235 degrees. Note the linear organization in the convective cells which are roughly aligned along a heading 190 degrees magnetic.

Fig. 4b. CAPPI scan constructed at 500 m above the lidar site using the data on 1 July. The bright areas correspond to aerosol laden structures that originate from the surface, while the dark regions indicate clear air between these structures. The distance between two adjacent tickmarks is 2 km on the horizontal axis and 1 km on the vertical axis. The lidar is situated 3 km to the right of the pictured scan area.

Fig. 5. Same as Fig. 4, but now for a shear driven ABL with low surface heat flux on 7 July 1987 at 0636 CDT. Linearly organized aerosol structures are lined up in a direction around 100 degrees. The CAPPI scan is made at 150 m above the lidar site. The distance between two adjacent tickmarks on the axes is 1 km. The lidar is located 2 km to the right of the shown scan area.

Fig. 6. The temporal high pass median filtering step, and the histogram equalization step are shown in pictorial form for the 1 July data set at 132109 CDT at 100 m height above the lidar site. The distance between two adjacent tickmarks is 2 km on the horizontal axis and 1 km on the vertical axis.

- a. CAPPI scan constructed from a volume scan. The correction for wind distortion is small because of the low wind speed, viz. smaller than 0.5 m/s.
- b. The temporal median, taken over 24 images, i.e. more than 1 hour time period, basically displays the motionless background. The fork shaped dark area around 8 km reflects the region of the creek beds on the surface.
- c. The temporal high pass median filtering removes the motionless background, which results in a little less contrast in the image.
- d. The histogram equalization clearly enhances the overall contrast in the image.

Fig. 7. A comparison of wind profiles measured by the UW VIL, the NOAA Doppler lidar and the radiosonde. Heights are measured relative to the lidar site. The NOAA lidar was located next to the UW VIL. The radiosonde was launched approximately 7 km from the VIL.

Upper : 7 July 1987

- _____ : 165 s average UW VIL wind profile at 0627 CDT,
- : Doppler lidar wind profile at 0611 CDT,
- : 165 s average UW VIL wind profile at 0654 CDT,
- .-.-.-.- : radiosonde wind profile at 0704 CDT.

The UW VIL wind profile is calculated at altitudes of 15, 30, 60, 100 m

and then at 50 m intervals above 100 m. The length of the temporal high pass median filter was 330 s. The lidar profile from 065444 to 065729 CDT was measured under conditions when the aerosol structures exhibited little contrast from their background. The radiosonde profile is vertically averaged over layers of 100 m thickness.

Lower : 1 July 1987.

_____ : 660 s average UW VIL wind profile at 1326 CDT,

----- : Doppler lidar wind profile at 1327 CDT,

_____ : 660 s average UW VIL wind profile at 1337 CDT,

..... : radiosonde wind profile at 1339 CDT.

The UW VIL wind measurements were calculated at 100 m vertical intervals. The length of the temporal high pass median filter was 3795 s. Thirty minute averaged 10 m altitude winds measured by PAM stations are also shown. The PAM stations were arrayed in a 15 km by 15 km area around the lidars. Two separate 30 minute averages are shown for each PAM station; the first average begins at 1300 and ends at 1330 CDT and measurements are marked by (o) in the figure. The second average period begins at 1330 and ends at 1400 CDT and measurements are denoted by (x).

Fig. 8. 165 s average wind profiles at 062718 CDT (upper) and 065444 CDT (lower) on 7 July 1987, measured using all the steps in the algorithm and deleting one of each steps. The length of the temporal high pass median filter was 330 s, i.e twice the time separation between two successive images.

_____ : including all steps in the wind measurement algorithm,

----- : no correction for wind distortion,

----- : no temporal high pass median filtering,
 .-.-.-. : no histogram equalization.

Fig. 9. UW VIL wind profiles obtained on 7 July at 065444 CDT using two different lengths of the temporal high pass median filter, viz. 330 and 990 s. Heights are relative to the lidar site.

Upper : Temporal averaging over 165 and 330 s.

_____ : median length of 330 s and temporal average of 165 s,
 ----- : median length of 990 s and temporal average of 165 s,
 ----- : median length of 330 s and temporal average of 330 s,
 .-.-.-. : median length of 990 s and temporal average of 330 s.

Lower : 165 s averages calculated with and without spatial high pass filtering (see Section 2.d) that eliminates scales larger than 2.5 km in both horizontal dimensions.

_____ : median length of 330 s,
 ----- : median length of 330 s and no spatial high pass filtering,
 ----- : median length of 990 s,
 .-.-.-. : median length of 990 s and no spatial high pass filtering.

Fig. 10. Profiles measured in the afternoon of 1 July 1987 at 1326 CDT using two different lengths, viz. 2640 and 3795 s, of the temporal high pass median filter and temporal averaging over 165 and 660 s. Heights are relative to the lidar site.

_____ : median length of 2640 s and temporal average of 165 s,
 ----- : median length of 3795 s and temporal average of 165 s,
 ----- : median length of 2640 s and temporal average of 660 s,
 .-.-.-. : median length of 3795 s and temporal average of 660 s.

Fig. 11. CCF's displayed as three-dimensional surfaces, for the 1 July and 7 July data sets. The axes are annotated in km. The same display

technique, with the same viewing position, as in Figs. 4 and 5 is used.

Upper : 1 July, 132109 to 132354 CDT, at 100 m height above the lidar site.

Lower : 7 July, 062718 to 063003 CDT, at 30 m height above the lidar site.

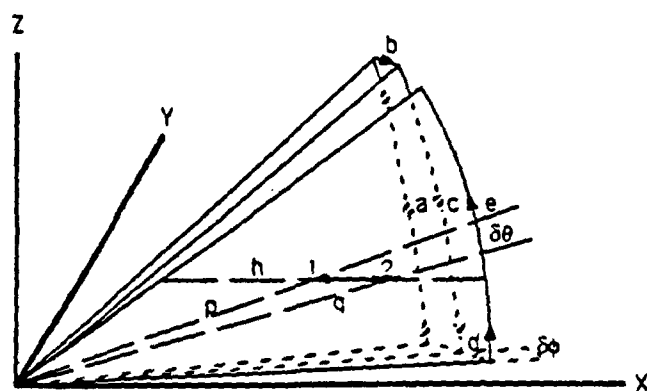


Fig. 1

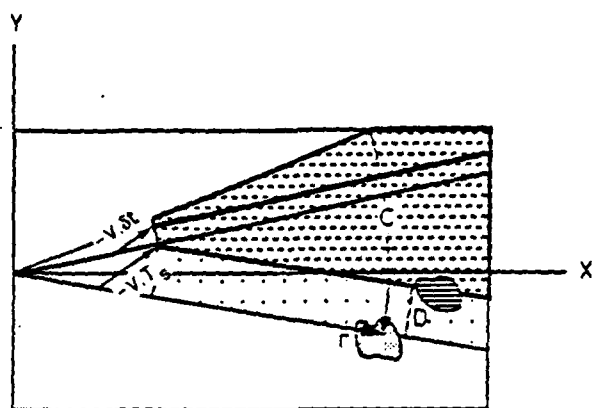
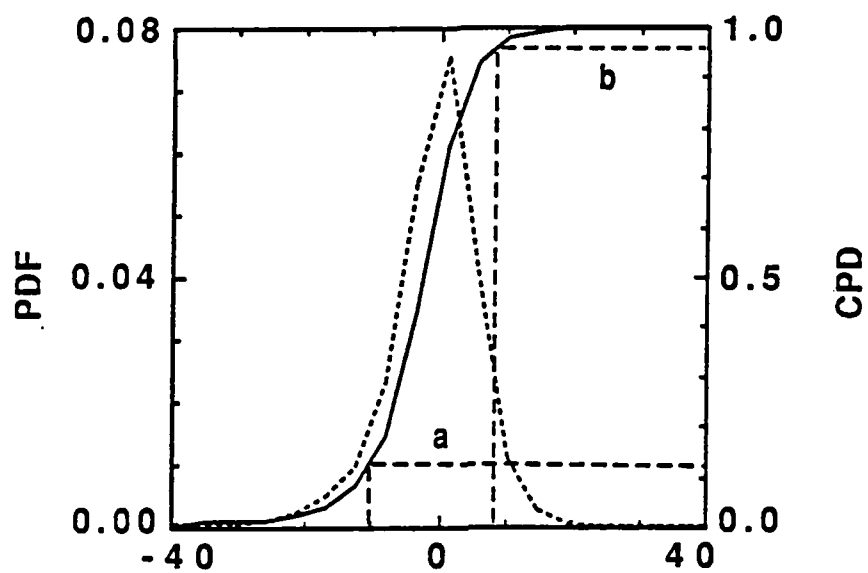
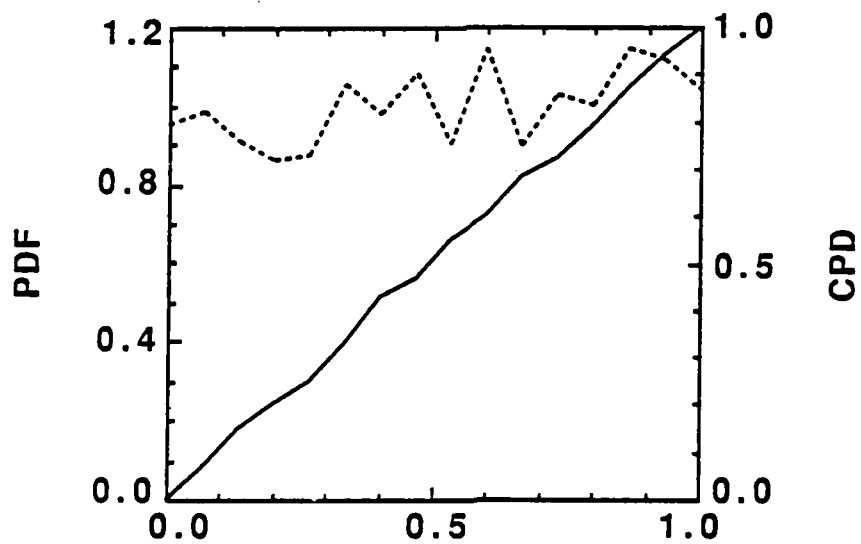


Fig. 2

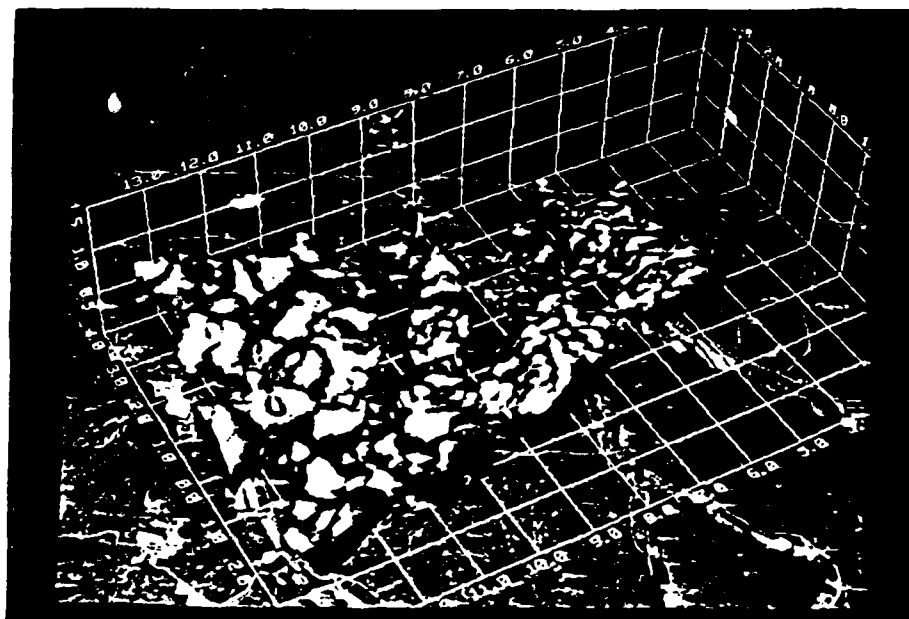


a

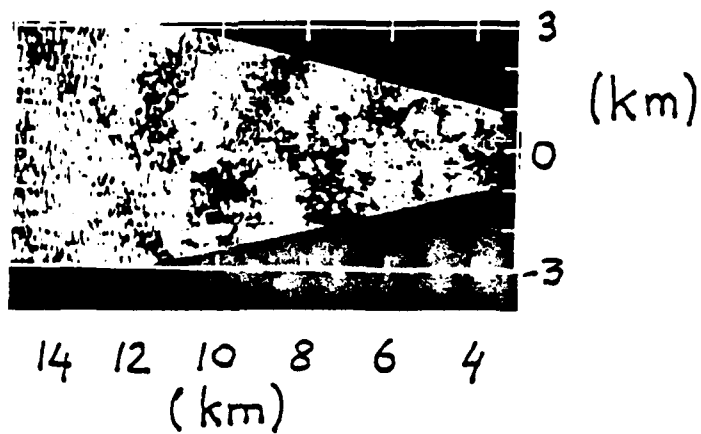


b

Fig. 3

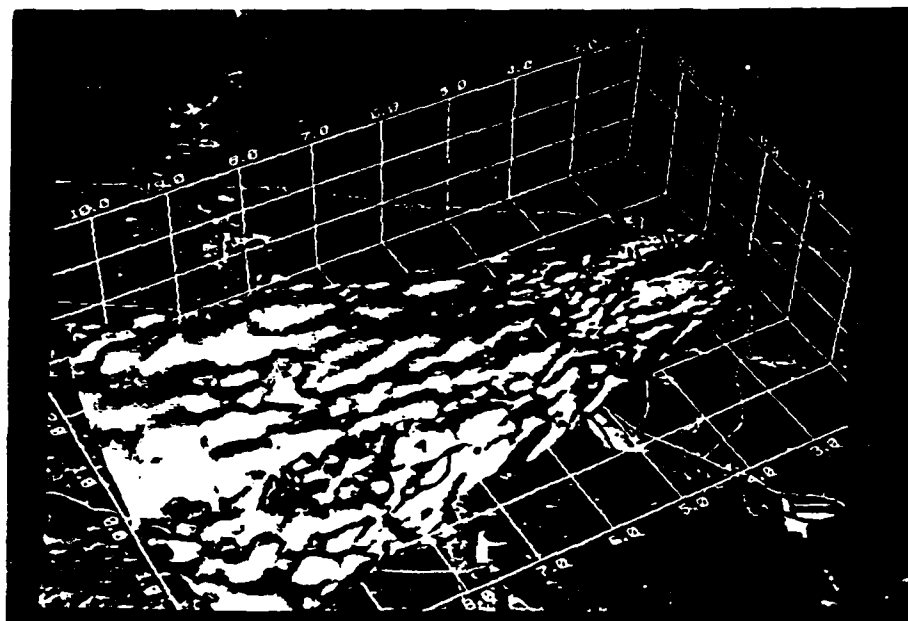


a

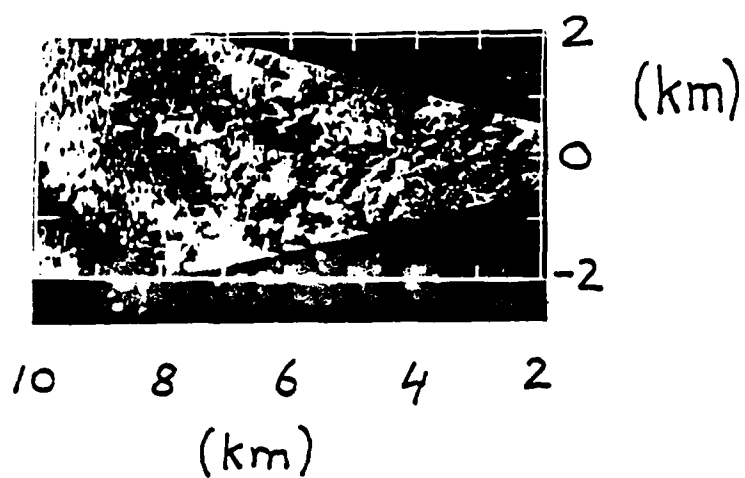


b

Fig. 4



a

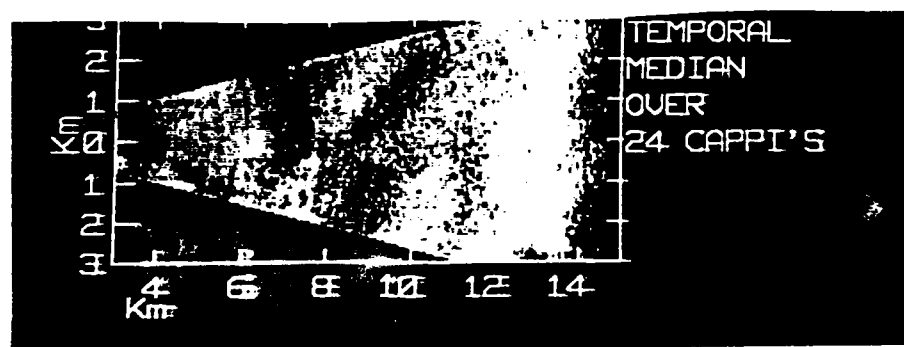


b

Fig. 5



a



b



c



d

Fig. 6

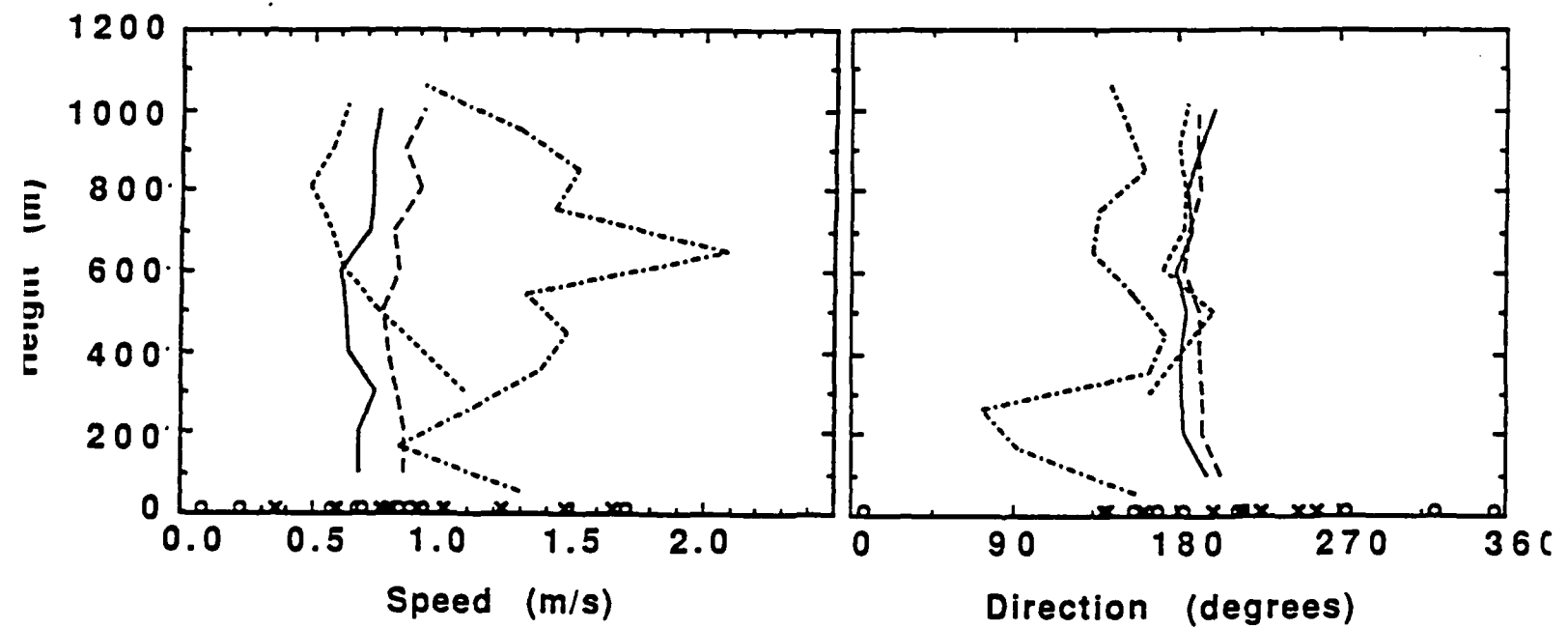
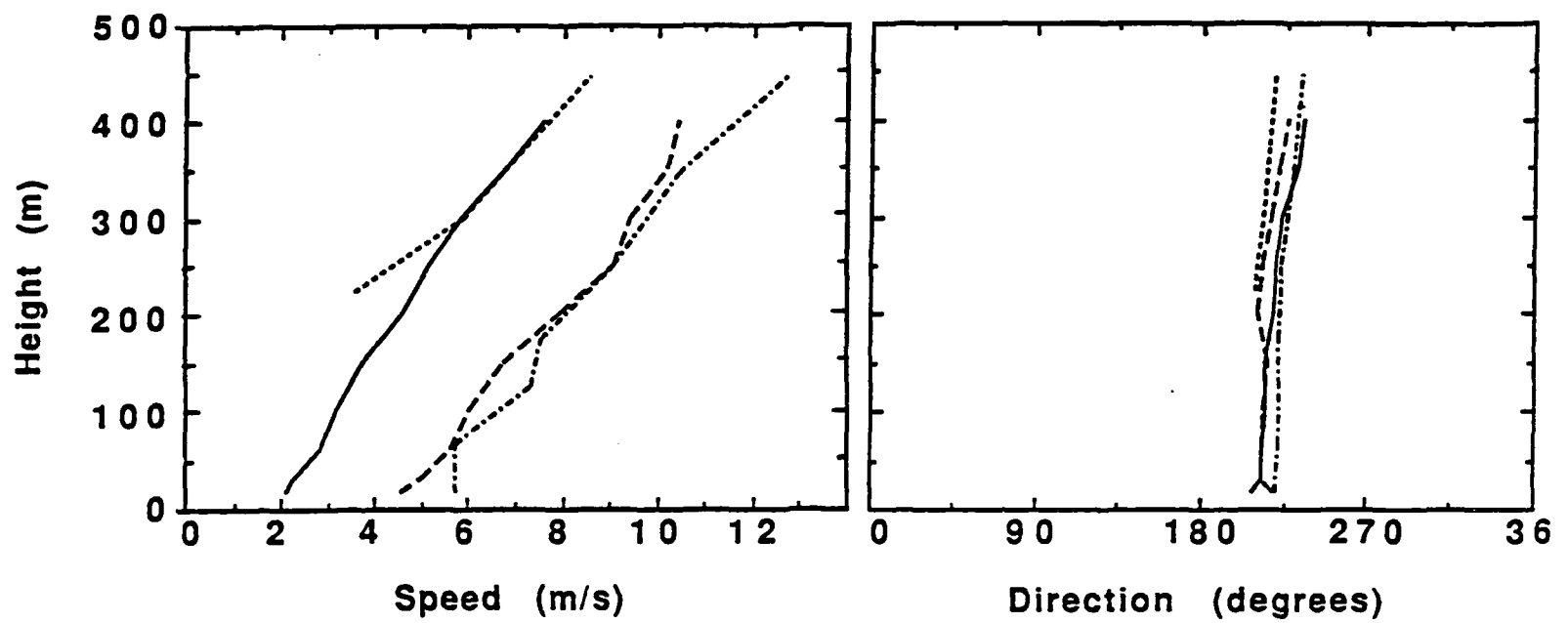


Fig. 7

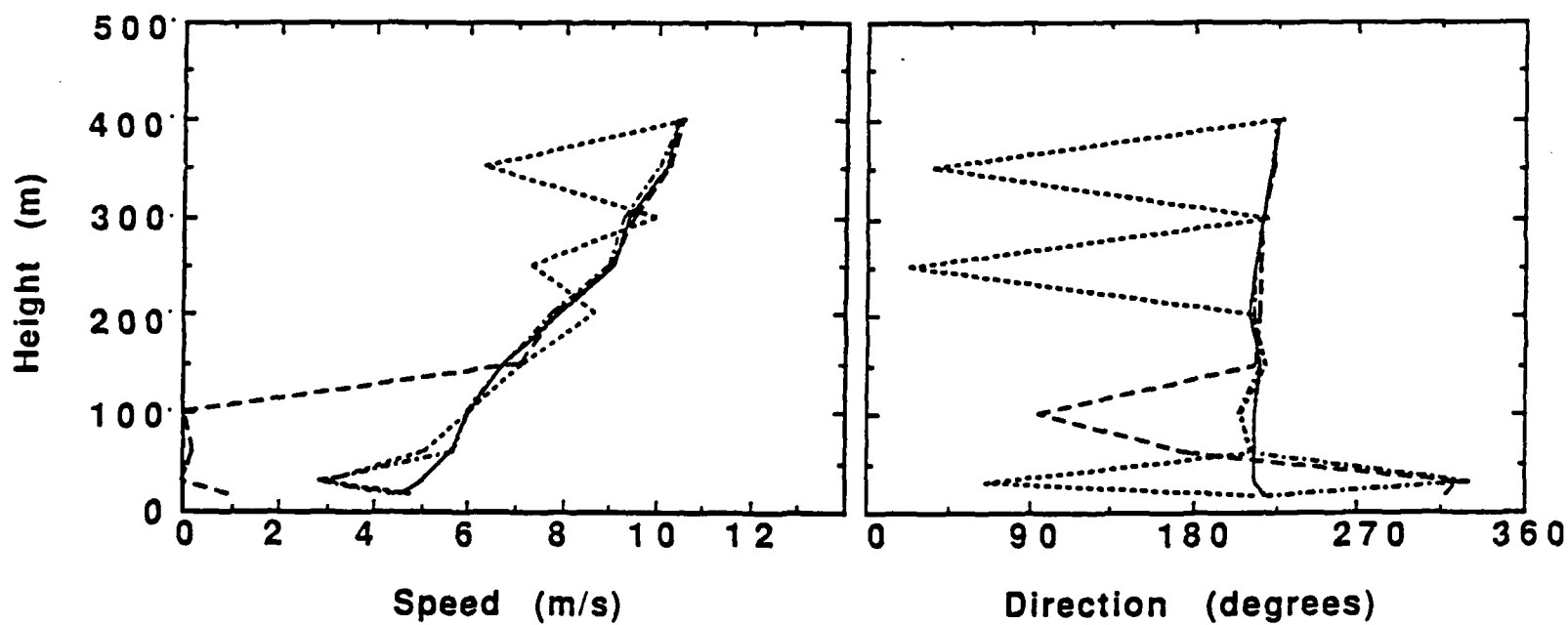
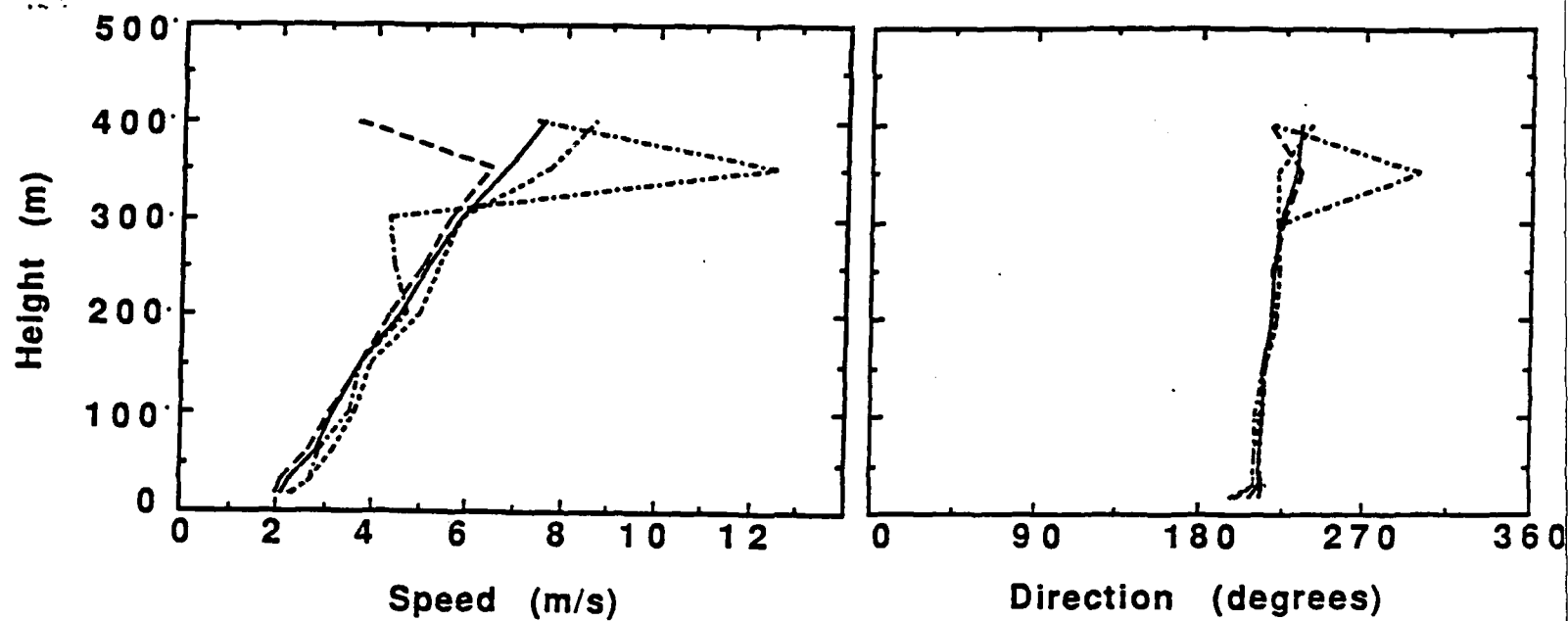


Fig. 8

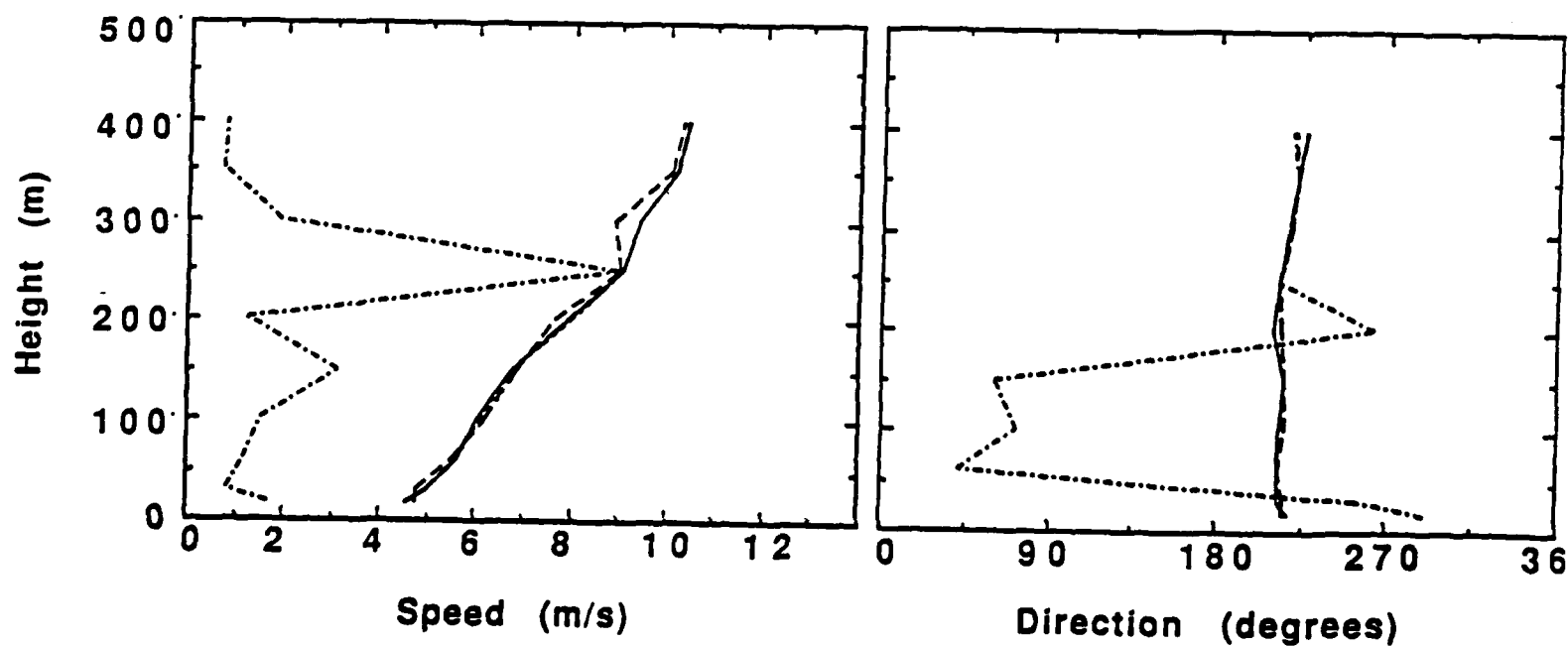
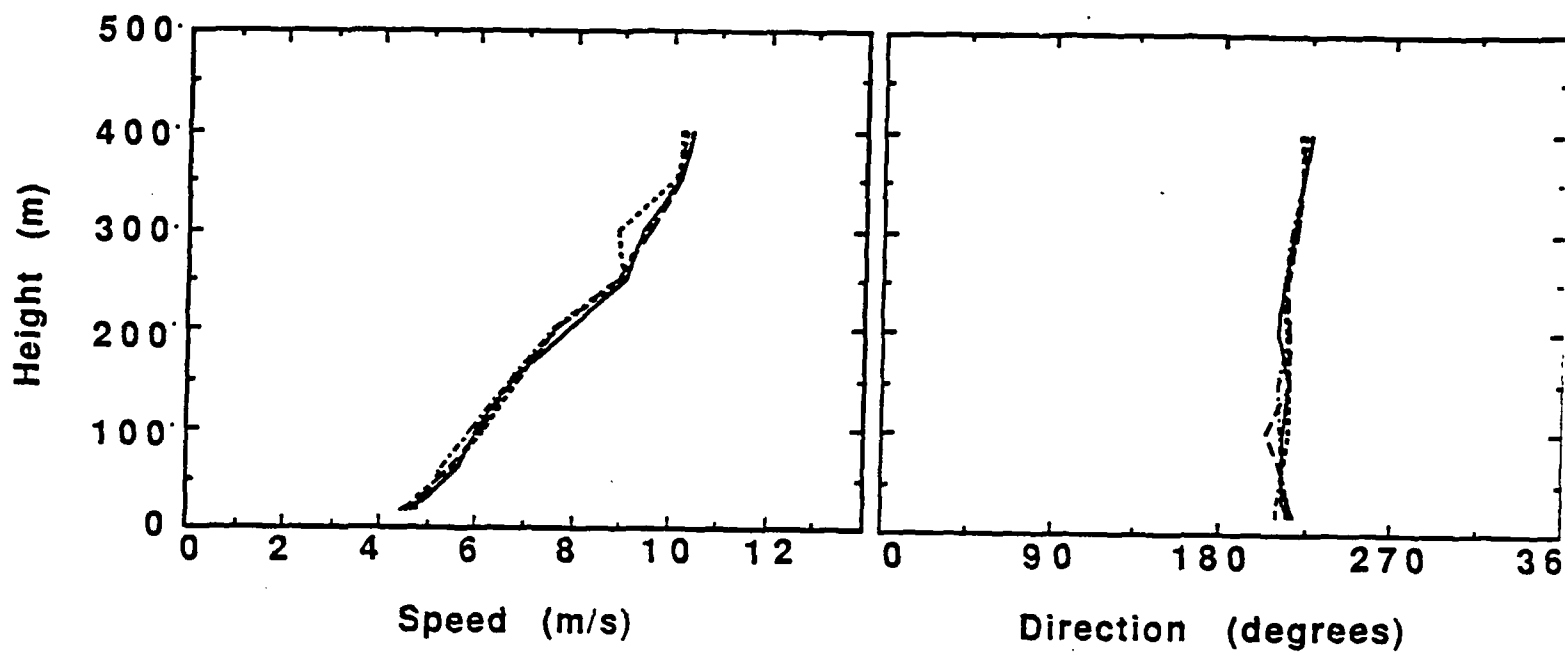


Fig. 0

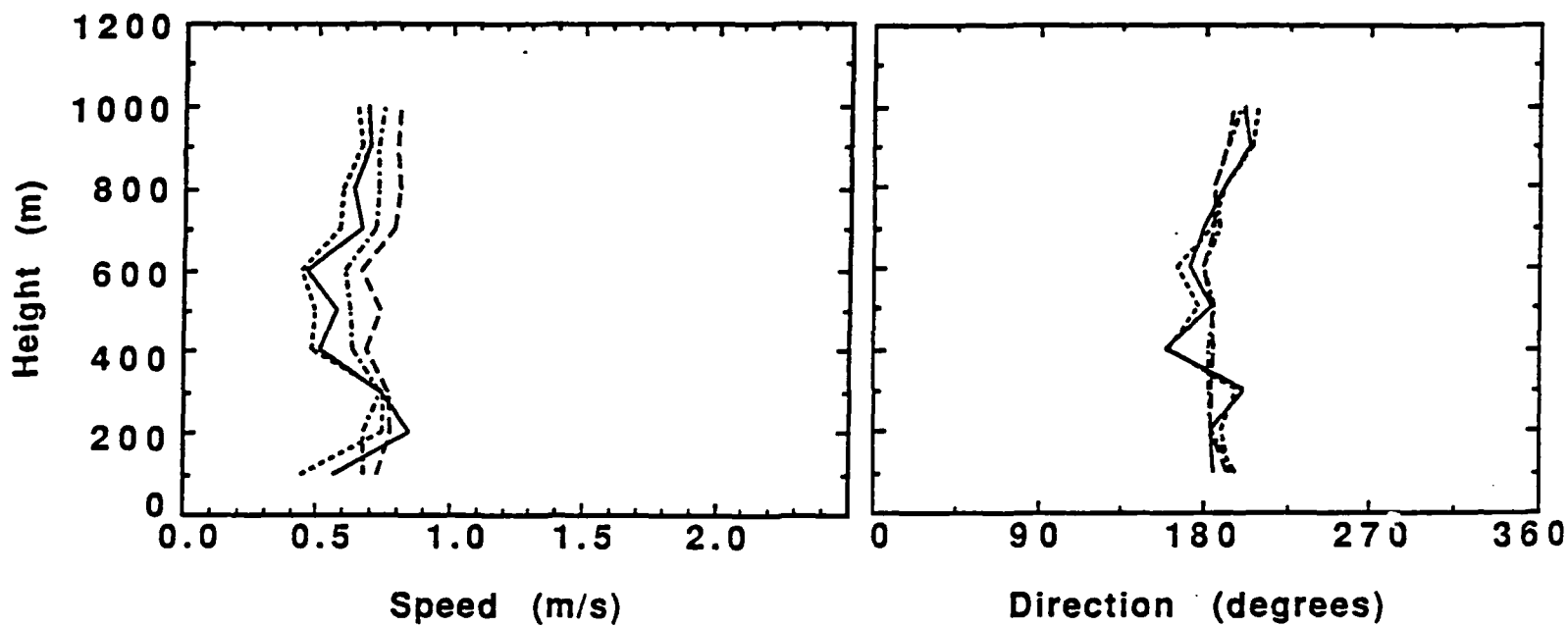


Fig.10

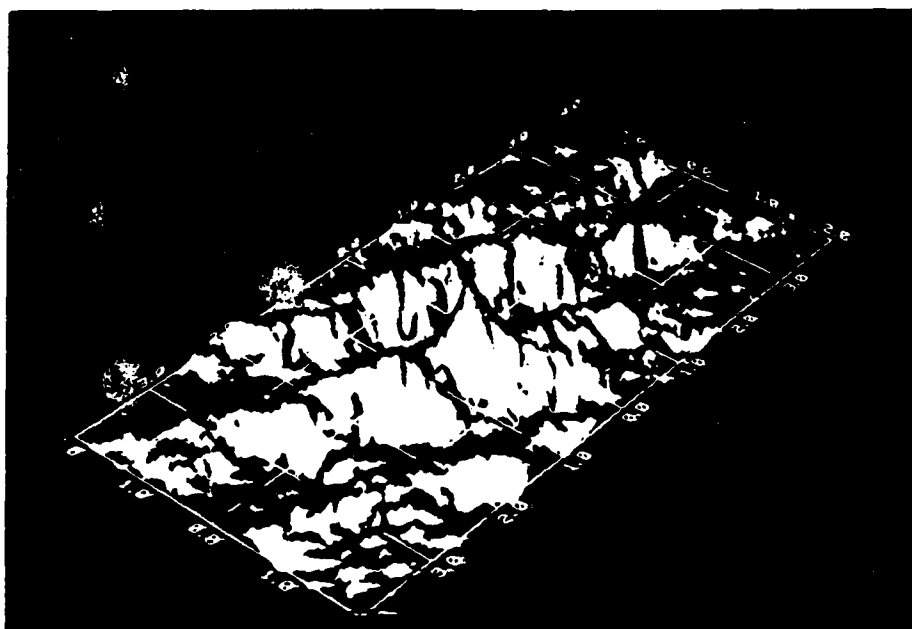
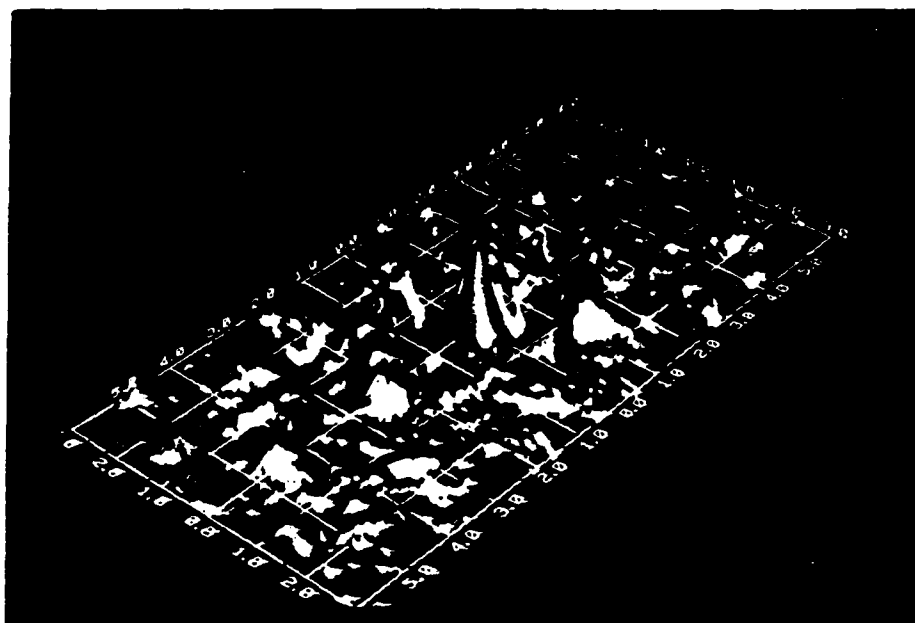


Fig. 11